Drying-Induced Structure Formation in Polymer Films

Doctoral Thesis

(Dissertation)

To be awarded the degree Doctor rerum naturalium

(Dr. rer. nat.)

Submitted by

Chakkresit Chindawong

(From Si Sa Ket, Thailand)

Approved by the Faculty of Natural and Materials Science

Clausthal University of Technology

Date of oral examination

12.03.2015

Chairperson of the Board of Examiners:

Prof. Dr. Sabine Beuermann

Chief Reviewer:

Prof. Dr. Diethelm Johannsmann

Reviewer:

Priv.-Doz. Dr. Jörg Adams

Acknowledgements

I wish to express my sincere gratitude and respect to *Prof Dr. Diethelm Johannsmann*, for his constant support, allowing and helping me to think and work independently, seed innovations to my work and constantly encouraging during the course of my work. I am will be remaining ever grateful to him for his teaching, guidance, friendship and wonderful personality.

I am particularly thankful to Associated *PD. Dr. Jörg Adams* for reviewing my thesis, numerous interesting helpful discussions, and for the support in all stages.

I am also very thankful to all people who contributed to this work (in no particular order).

Dr. Arne Langoff helped me in the measurements with confocal microscope and also helpful discussion.

Michael Tölle was never hesitating to support me when practical help, materials, or reactants were needed.

Special thanks go to Ms. Goertz and Ms. Kornhardt.

I am very much thankful to Sylvia Hanke and her husband for pick up me from Hannover air port.

Katja always supported me with her effort and companion in the different meeting and conferences in Berlin and Freiburg.

Andreas Böttcher for cutting polycarbonate sheets and many helpful technical components.

I must very thank to Rebekka, Robert, Stefanie for impressive moment.

Of course I am also deeply grateful to all other people in our institute for numerous discussions, for practical help whenever it was needed and for the perfect working atmosphere.

I take this opportunity to express my sincere gratitude to my sisters, my brothers

The financial support to this work was provided by Thai Ministry of Science and Technology which is gratefully acknowledgment.

Table of contents

Chapter 1

Literature Review

1.1 Film Formation of Polymer Latex

1.1.1 Definition of polymer latex

A latex is defined as a stable colloidal dispersion of a polymeric particles (usually spherical) in an aqueous medium.[1] The range of polymer particle diameters is approximately a few hundred nanometers and the polymer volume fraction ranges from 0.4 to 0.7.[2] An alternative definition, from the International Union of Pure and Applied Chemistry (IUPAC), is that colloidal particles have at least one dimension between 1 nm and 1 μm (IUPAC2009).[3, 4] The dispersed particles are larger than atomic dimensions but small enough to exhibit *Brownian* motion, which prevents appreciable sedimentation in normal gravity.[5] Brownian motion is the result of an imbalance of force between the colloidal particles and the surrounding molecules of the solvent. It provides evidence for the existence of molecules.

Polymer latexes are classified according to their producing method as natural (produced by metabolic process occurring in the cells of certain plant species), artificial (produced by dispersing a polymer in a dispersion medium) and synthetic (produced by the emulsion polymerization). To produce a synthetic latex, aqueous emulsion polymerization is carried out by gently agitating water, monomer, water soluble initiator and surfactant.[6] The initiator decomposes to give a steady flux of free radicals, which initiate the polymerization. A surfactant is used to provide a stable emulsion system, influencing the polymer particle size and particle size distribution polymer.

1.1.2 Main steps of latex film formation

When latex is cast on a substrate and evaporation is allowed, a continuous, homogeneous film is formed under appropriate conditions. This process is called film formation.[7-10]

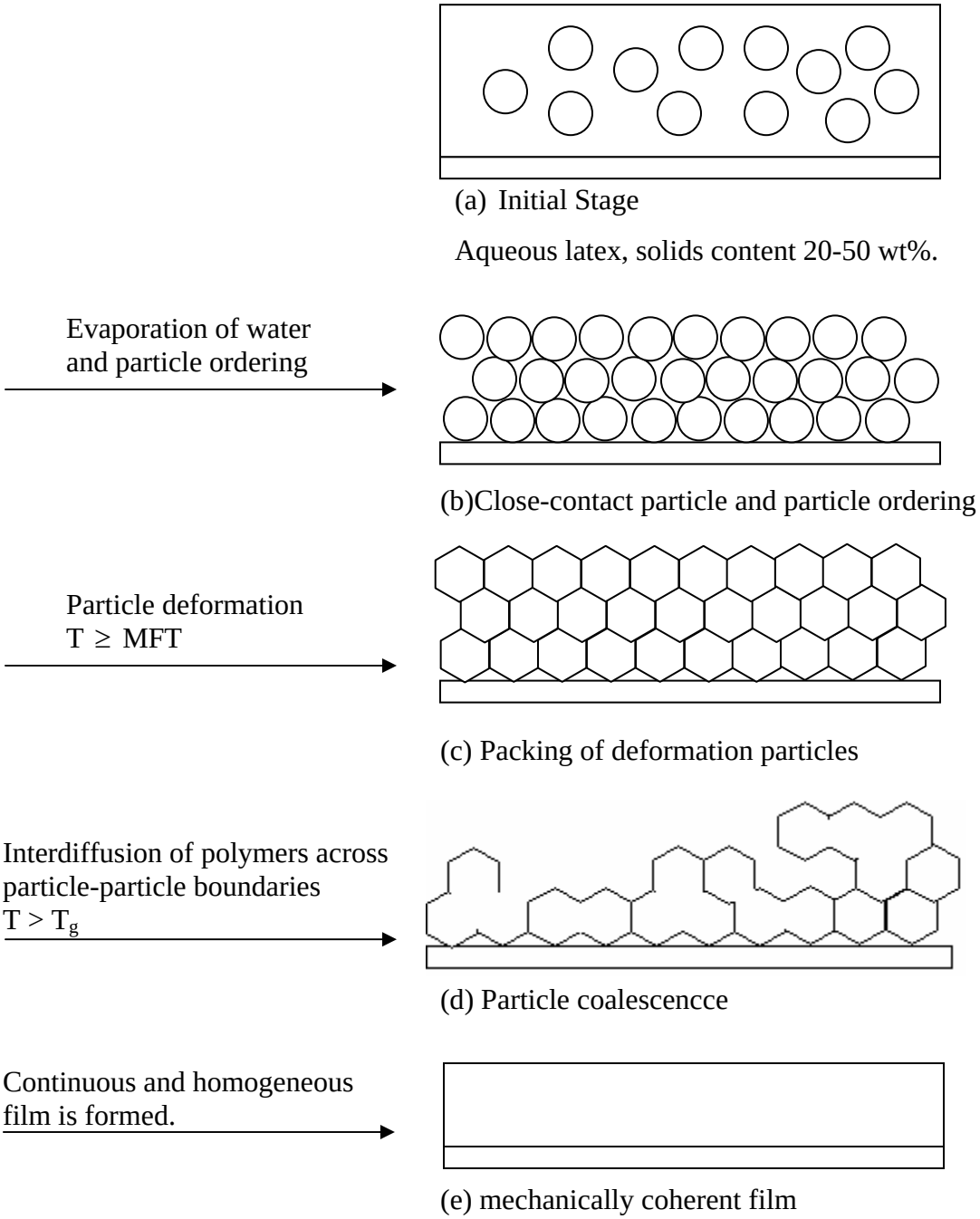

Figure 1: Steps of latex film formation

The main steps of film formation are (Fig. 1):

a) Initial stage: The latex is cast on the substrate. The dispersion has around 10 - 50 wt% solids content. There is no particle ordering. The latex polymer core is hydrophobic and it is therefore surrounded by a hydrophilic surfactant shell making it soluble in water.
b) Evaporation of water results in a more concentrated dispersion and particle ordering.
c) Particle deformation occurs in order to fill all voids left by the removal of the water.
d) Particle coalescence and interdiffusion of polymer across particle-particle boundaries take place. Coalescence is the union of particles to reduce their total surface area.
e) Finally, a clear, continuous and homogeneous film is formed.

It is important also to mention, that for successful film formation, the film must be formed at or above the minimum film-formation temperature (MFT). The MFT is the minimum temperature at which the dry film is transparent and crack-free. If the temperature is above the polymer's glass transition temperature, T_g, aging or further coalescence of the film can result.

1.1.3 Particle distribution during solvent evaporation from thick films

In a fluid which contains particle in a solvent (e.g. latex), as the solvent evaporates, the particle concentration increases. It is often observed for thick films that the particle distribution during drying is not uniform, but a layer of consolidated particles lies on top of a still fluid dispersion below. Routh and Russel[11, 12] proposed the use of a Peclet number, P_e, which controls the vertical distribution of particles. P_e is the ratio of the time for diffusion, t_{diff}, over the drying time, t_{dry}, and given by:

$$P_e = \frac{t_{diff}}{t_{dry}} = \frac{h^2 / D_0}{h / \dot{E}} = \frac{6\pi\eta R h \dot{E}}{kT} \qquad (1.1)$$

η is the solvent viscosity, *R* is the particle radius, *h* is the initial film thickness, $\dot{E}$ is the evaporation rate, *kT* is the thermal energy. For colloidal particles the Stokes-Einstein diffusion coefficient is given by

$$D_0 = \frac{kT}{6\pi\eta R} \qquad (1.2)$$

When $P_e << 1$, diffusion is strong relative to evaporation and uniform particle profiles are expected. For $P_e >> 1$, particles are predicted to be accumulated at the film surface (Fig. 2)

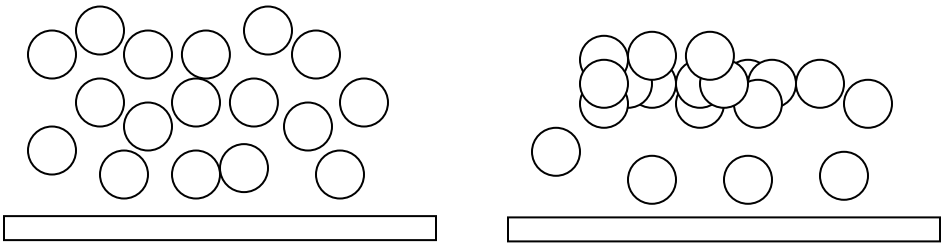

(a) $P_e << 1$, uniform drying (b) $P_e >> 1$, non-uniform drying

Figure 2: Uniform and not uniform drying of a latex films of thickness *h* depending on the Peclet number.[13]

1.1.4 Forces operative during film formation

Initially we can divide the forces on colloidal particles[14] into two types:

a) Those from the surrounding liquid: if the colloidal particle is completely surrounded by liquid, an isotropic hydrostatic pressure is applied to it, which is equal to the liquid pressure.

b) Those from the presence of other colloidal particles. Suppose we have two particles touching each other at one point, and also suppose that the net force is such that the particles are just not repelled by each other but also do not deform each other. At that point the stress condition is isotropic with a value

equal to that of the liquid pressure. So, the net force between two contacting colloidal particles is equal to the total force minus the force of the isotropic stress in the particles due to the liquid pressure. Consequently, only external forces can deviate from the isotropic atress condition within the particles and result in particle deformation.

These external forces can be:

a) Gravitational force
b) The van der Waal force
c) The repulsive force caused by the onerlap of the electric double layers
d) The capillary pressure caused by the receding of the bulk/water air interface
e) The capillary pressure caused by liquid bridges between particles

The gravitational force leads to setting in a dispersion but in our case is very small and can be neglected.

The van der Waals force is the attractive force particles experience when brought within a very small distance from each other, within a few nanometers. The origin of this force lies in fluctuation in the charge distribution of the atoms. The van der Waal force F_{attr} for two identical sphere is given by:

$$F_{attr} = -\frac{A}{6R}\left[\frac{-4s}{\left(s^2-4\right)^2} - \frac{4}{s^3} + \frac{8}{s\left(s^2-4\right)}\right] \qquad (1.3)$$

where A is the Hamaker constant, and s is the dimensionless distance defined as the ratio of the distance between the particle centres and the particle radius.

The repulsive force caused by the overlap of the electric double layers

Colloidal particles in latex coating can be stabilized by either electrostatic forces, due to the presence of charged groups at the particle surface, or by steric means i.e. by repulsion between low molecular weight polymers adsorbed at the interface. Also these two mechanisms can be combined. These repulsive forces have to be overcome in latex film formation so that the latex particles can approach each other close enough to deform.

How strong these forces are is determined by the surface charge density and the subsequent distribution of the electrolyte near the interface.

The capillary pressure caused by a receding bulk/water air interface.

Before the stage when the deformation of the particle starts, we have a dense random packing of the colloidal particles with some water still between the particles. The air water in interface forms a meniscus. In this case a pressure difference exists over the curved surface with the higher pressure on the inner side of the curvature (Fig. 3).

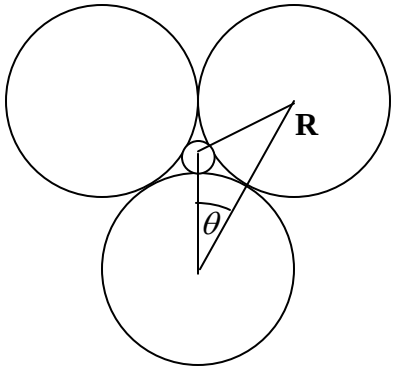

Figure 3: Water/air interface into the packing of the particles, where θ is the contact angle of the water air interface and the particles and R is the particle radius.

This pressure is called capillary pressure and for a meniscus in the neck regions between three particles is given by:

$$\Delta P_C \approx 12.9 \frac{\gamma_{w/a} \cos\theta}{R} \qquad (1.4)$$

where θ is the contact angle of the water/air interface and the particles and $\gamma_{w/a}$ is the water/air surface tension.

The capillary pressure caused by liquid bridges between particles

When the water/air interface reaches the substrate surface, some water can remain between particles in contact forming liquid bridges. (Fig. 4). Again there is a pressure difference between the inside and the outside of the bridge, and depending on the curvature of the liquid bridge the pressure will tend to press the particle together or push them apart.

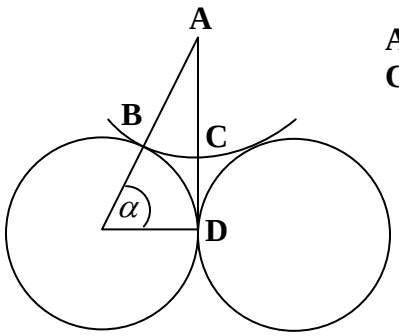

Figure 4: Water/air interface at the contacts between particles. Where, r_1 and r_2 are the radii of the liquid bridge and α is the filling angle.

This pressure difference is given by:

$$\Delta P_C = \gamma_{w/a}(r_1^{-1} + r_2^{-1}) \qquad (1.5)$$

where r_1 and r_2 are the radii of the liquid bridge (negative radii of curvature corresponds to concave surfaces, while positive radii corresponds to convex surface), as defined in Fig. 4 and from geometric considerations we have:

$$\begin{aligned} r_1 &= -R\frac{1-\cos\alpha}{\cos(\alpha+\theta)} \\ r_2 &= R\left[\sin\alpha + \frac{1-\cos\alpha}{\cos(\alpha+\theta)}(\sin(\alpha+\theta)-1\right] \end{aligned} \qquad (1.6)$$

where α is the filling angle.

In this case it is more revealing to consider the force, F_c as the contact force pushing the particles apart, instead of the pressure resulting from these bridges. This force is provided by the pressure inside the liquid bridge pulling or pushing the spheres apart and by the water/air surface tension $\gamma_{w/a}$ pulling the spheres together. This is given by:

$$F_C = \Delta P_C \pi r_2^2 - 2\pi r_2 \gamma_{w/a} \qquad (1.7)$$

A negative F_c corresponds to the case where the two spheres are pulled together.

1.1.5 Driving force for the particle deformation

There was a disagreement between Dillon et al and Brown about which is the driving force for the particle coalescence.[3, 15] On the one hand, Dillo et al. [16] proposed that the driving force for the particle coalescence is the surface tension of the polymer/air interface, $\gamma_{p/a}$. They assumed particle deformation occurs after water has left the film and treated the latex particles as viscous apheres. In this case the excess pressure due to the surface tension inside a spherical surface of radius *R* over the outside surface is given by:

$$P = \frac{2\gamma_{p/a}}{R} \qquad (1.8)$$

They used the Frenkel equation[17]

$$\theta^2 = \frac{3\gamma t}{2\pi R \eta} \qquad (1.9)$$

where θ is the half angle of coalescence defined in Fig. 5 and η is the viscosity of the polymer.

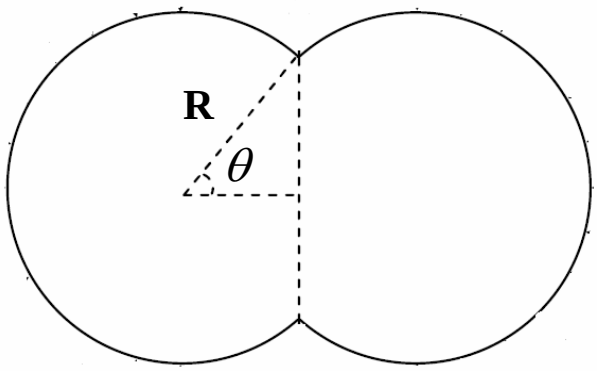

Figure 5: Model of two coalescing spheres as proposed by Frenkel (1945).[8] The half angle of coalescence θ and the radius R of the particles.

We can note several points from the above. First of all, the angle θ is a valuable measure of the action of the latex and relates to the physical properties of the film.
The higher the θ, the voids in the film become smaller, which results in increased tensile strength, when diffusion across particle boundaries take place. From above we can also see that θ is proportional to the surface tension and inversely proportional to the viscosity and the particle radius. That means for a given latex we can change the viscosity, and this will affect the θ and consequently the particle coalescence. The viscosity can be changed either by heating the film or by the addition of plasticizers that lower the glass transition temperature, relative to the ambient temperature.
In the case of heating, we have the Vogel-Fulcher equation to describe the temperature dependence of viscosity η:

$$\eta = \eta_0 \exp\left(\frac{B}{T - T_0}\right) \qquad (1.10)$$

where η_0, B and T_0 constants.

Form this we can see that a temperature increase of the polymer results in a lower viscosity. From the Frenkel equation, lower η means a higher θ and so a better particle coalescencec.

On the other hand, Brown argued that the capillary forces are the primary driving forces for the particle deformation and treated the particles as elastic spheres. According to Brown the condition for film formation, the capillary force F_C is higher than the resistance of the spheres to deformation F_G. So:

$$F_C > F_G$$

Brown showed that this condition implies

$$G_t < 35\gamma_{w/a} / R \qquad (1.11)$$

Here, G_t is the shear modulus of the film measured by observing the strain resulting from the application of stress for duration of time t.

Initially there was a belief that one of the two models is correct and the other not. Actually, as shown in more recent works, the driving force for the particle deformation depends on the condition of drying and the characteristics of the polymer particles and film.

As shown in the work from Routh and Russel[18], there are the following cases:

Wet Sintering: The driving force is polymer-water surface tension. It occurs when the evaporation time is higher than the time for viscous collapse. This relates to the model of Dillon.

Dry sintering: The driving force is the polymer-air surface tension. It occurs when the evaporation time is much less than the time needed for viscous collapse.

Capillary deformation: The driving force is the water/air surface tension as proposed by Brown.

Receding water front: Initially deformation occurs by capillary mechanisms, but the deformation is not complet by the time the capillary pressure reaches the maximum value. After this step, as the water evaporates and leaves dry particles behind, the deformation mechanism, switches to a dry or moist sintering.

Sheetz deformation: In some case there is a possibility of skin formation in a drying film. The skin is a coalescenced polymer layer above a wet layer. Sheetz argued

that diffusion of water through the skin creates a large osmotic pressure in the fluid below, causing deformation. Another possible explanation, as the skin slows evaporation, other mechanism like wet sintering can cause compaction.

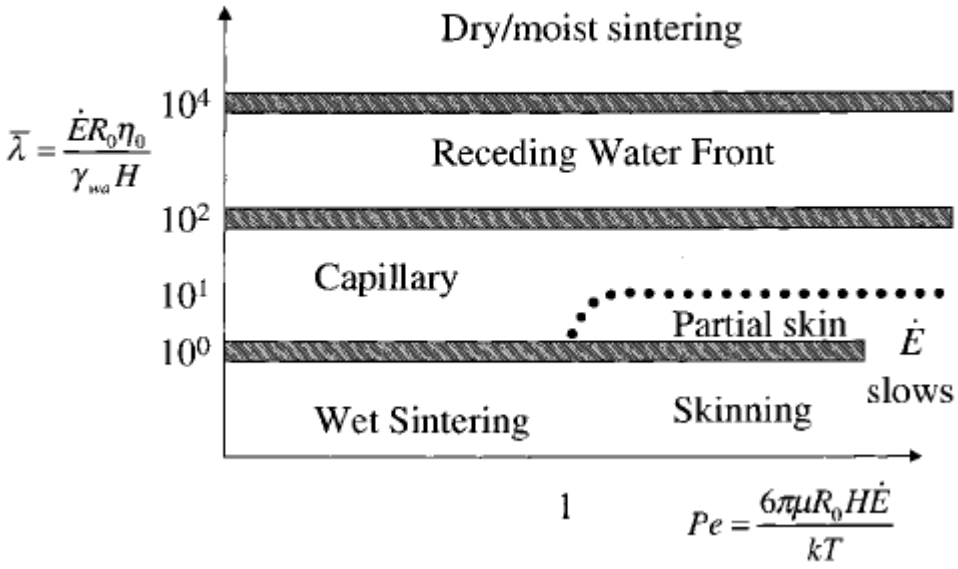

Figure 6: Driving forces for deformation of latex particles depending on the drying conditions. [13, 18]

In the Fig. 6 we can see which of the above mechanisms occurs depending on several factors. $\bar{\lambda} = \frac{JR\eta}{\gamma_{w/a}h}$ is the ratio of the time for viscous collapse over the evaporation time (all these parameters have been defined above), and P_e is the Peclect number as described in section 1.1.3. Skin formation will only occur when drying is non-uniform ($P_e >> 1$) and the film is subject to wet sintering. Furthermore, it was shown that the addition of salts can increase the tendency for skin formation.[13] This happens as the addition of salts can decrease the electrostatic repulsion of latex particles and hence encourage coalescence of the particles. Furthermore, induced flocculation can promote heterogeneous drying and hence increase the likelihood for skin formation. It was also

found the the drying is not only affected by the concentration of the salt and the valency of its ions, but also affected by the type of ions.

References

1. Zohrehvand, S. Film Formation from Water-Borne Latex Dispersions. Doctoral Thesis, Delft, 2001.

2. Mark, H. F.; Bikales, N. M.; Overberger, C. G.; Menges, G., *Encyclopedia of polymer science and engineering*. John Wiley & Sons Ltd: New York, 1989; Vol. 8.

3. J. L. Keddie; Routh, A. F., *Fundamentals of Latex Film Formation: Processes and Properties*. Springer: Dordecht, 2010; Vol. Chapter 1.

4. Keddie, J. L.; Routh, A. F., Fundamentals of Latex Film Formation: Processes and Properties. *Springer* **2010**.

5. Sood, A. K., Structural Ordering in Colloidal Suspensions *Solid State Physics* **1991,** 45, 1-73.

6. Mark, H. F.; Bikales, N. M.; C.G., O.; Menges, G., *Encyclopedia of Polymer Science and Technology*. 2nd Ed. ed.; John Wiley & Sons Ltd: New York, 1974; Vol. 6

7. Keddie, J. L., Film formation of latex. *Materials Science and Engineering* **1997,** 21, (3), 101-170.

8. Nilsson, K. Film formation of latex in dry coating films. Master Thesis, Karlstads universitet, Karlstad, 2007.

9. Routh, A. F.; Russel, W. B., Horizontal drying fronts during solvent evaporation from latex films. *AIChE Journal* **1998,** 44, (9), 2088-2098.

10. Y. Chevalier; C. Pichot; C. Graillat; M. Joanicot; K. Wong; J. Maquet; P. Lindner; Cabane, B., Film formation with latex particles. *Colloid and Polymer Science* **1992,** 270, (8), 806-821.

11. Routh, A. F.; Russel, W. B., A Process Model for Latex Film Formation: Limiting Regimes for Individual Driving Forces. *Langmuir* **1999,** 15, (22), 7762-7773.

12. Routh, A. F.; Zimmerman, W. B., Distribution of particles during solvent evaporation from films. *Chemical Engineering Science* **2004,** 59, (14), 2961-2968.

13. König, A. M.; Weerakkody, T. G.; Keddie, J. L.; Johannsmann, D., Heterogeneous Drying of Colloidal Polymer Films: Dependence on Added Salt. *Langmuir* **2008,** 24, (14), 7580-7589.

14. Visschers, M.; Laven, J.; van der Linde, R., Forces operative during film formation from latex dispersions. *Progress in Organic Coatings* **1997,** 31, (4), 311-323.

15. Jensen, D. P.; Morgan, L. W., Particle size as it relates to the minimum film formation temperature of latices. *Journal of Applied Polymer Science* **1991,** 42, (10), 2845-2849.

16. Dillon, R. E.; Matheson, L. A.; Bradford, E. B., Sintering of synthetic latex particles. *Journal of Colloid Science* **1951,** 6, (2), 108-117.

17. M.M.Ristic; S.Dj.Milosevic, Frenkel's Theory of Sintering. *Science of Sintering* **2006,** 38, 7-11.

18. Routh, A. F.; Russel, W. B., Deformation Mechanisms during Latex Film Formation: Experimental Evidence. *Industrial & Engineering Chemistry Research* **2001,** 40, (20), 4302-4308.

1.2 Evaporative Lithography

1.2.1 Introduction

In the evaporative lithography a mask with regulary ordered holes is placed above a drying suspension or dispersion. After the evaporation of the solvent, a patterned film with raised features results. The evaporative lithography method was initially proposed by Routh and Russel.[1] More recently Harris et al.[2] studied the evaporative lithographic patterning of colloidal films.

1.2.2 Preliminary studies

Evaporative lithography was studied initially by Routh and Russel.[1] They developed a model to predict the horizontal drying fronts during solvent evaporation from a latex film. This model can also be applied for nonuniform drying of the film. In this case it is assumed that a cover is placed over an initially uniform dispersion. The cover hinders the evaporation in the area below it. According to the model, for the area with the evaporation, the height *h* follows Eq. 1. over time *t* and for the area without a cover, it follows Eq. 2. For both case the volume fraction, ϕ, follows Eq. 3.

$$1+\frac{\partial \bar{h}}{\partial \bar{t}}+\frac{\partial}{\partial \bar{x}}\left(\bar{h}^{3}\frac{\partial^{3}\bar{h}}{\partial \bar{x}^{3}}\right)=0 \qquad (1)$$

$$\frac{\partial \bar{h}}{\partial \bar{t}}+\frac{\partial}{\partial \bar{x}}\left(\bar{h}^{3}\frac{\partial^{3}\bar{h}}{\partial \bar{x}^{3}}\right)=0 \qquad (2)$$

$$\frac{\partial \bar{h}\phi}{\partial \bar{t}}+\frac{\partial \phi \bar{h}\bar{u}_{x}}{\partial \bar{x}}=0 \qquad (3)$$

where $\bar{u}_x=\bar{h}^{2}\frac{\partial^{3}\bar{h}}{\partial \bar{x}^{3}}$ is the dimensionless vertically averaged horizontal velocity.

Furthermore, it is important to mention that in this model the horizontal distances, x, are expressed in units of L, which is capillary length and is expressed by

$$L=h_i\left(\frac{\gamma}{3\eta_0\dot{E}}\right)^{1/4} \qquad (4)$$

where h_i is the initial wet thickness of the film, $\dot{E}$ is the evaporation rate, η_0 is the viscosity of the dispersion, and γ is the surface tension of the dispersion.

In order to examine the model, a latex film with an initially constant height of 0.15 mm was cast. Above it and at a close distance, in order to hinder evaporation, a cover with regularly spaced holes was placed. The resulting film is shown in Fig. 1(a). It is clear from this figure, that there are raised features in the film in the open areas. A magnified view of this film is shown in Fig. 1(b). The center-to-center spacing was estimated to be around 4L. Under these conditions for thickness and center-to-center distance, the model prediction is shown in Fig. 1(c). As shown in Fig. 1(c) the film height rises from the centres of the evaporating regions on either side up to the transition, and then drops towards the centre of the covered region. Profilometry of a similar region on the film is shown in Fig. 1.4(d). Comparing Fig. 1.4(c) and Fig. 1.4(d), it is clear that the model predicts the observed trend.

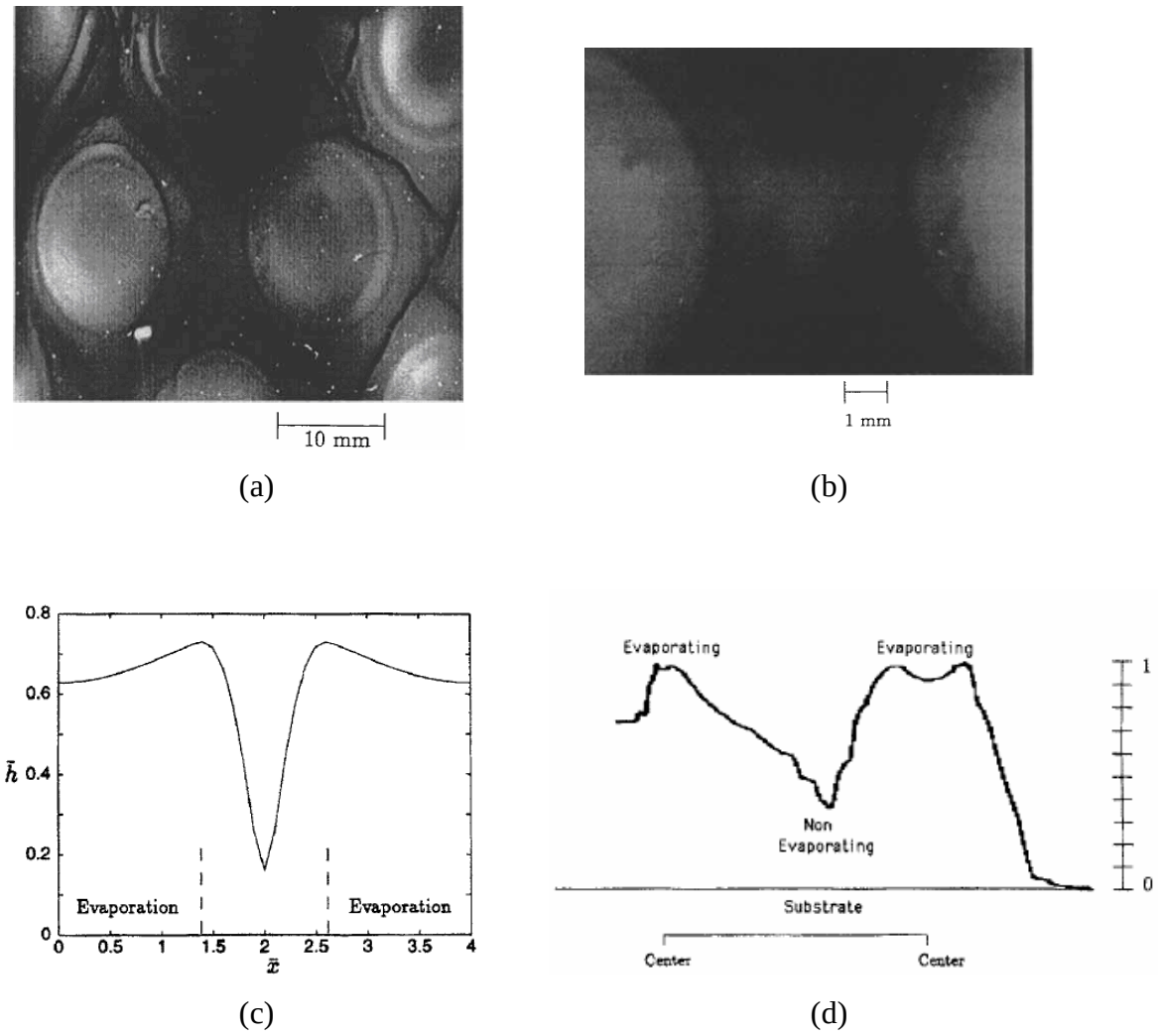

Figure 1 (a) Photo of a film with selective evaporation in circular regions; (b) magnified view of the same film; (c) prediction of the model under the same conditions and (d) results from profilometry experiments. Results taken from Ref. 1.

1.2.3 Principles of technique

In the evaporative lithography technique,[2] a mask with an hexagonal array of holes is placed above a drying colloidal aqueous suspension. A schematic representation of the evaporative lithography process is shown in Fig. 2(a),(b) where, P is the pitch, or centre-to-centre distance of holes, dh is the hole diameter, hg is the initial gap height between the mask and the underlying film, and hi is the initial thickness of the wet film.

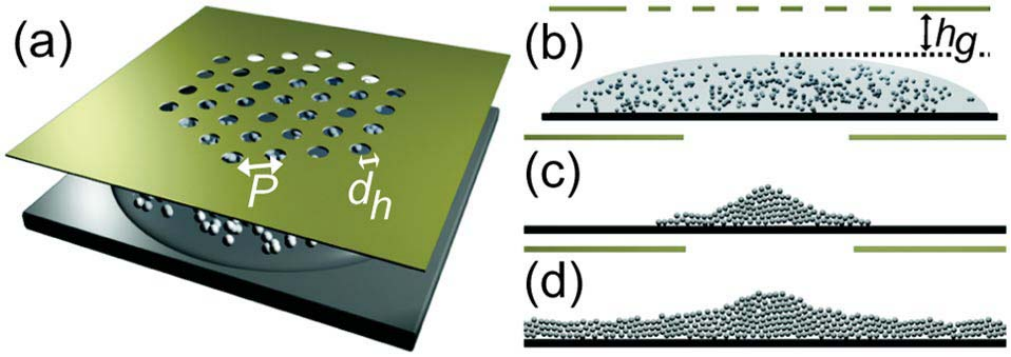

Figure 2 Schematic presentation of (a) the evaporative lithography process (b) side view of the film after casting (c) discrete pattern feature from an initial dilute suspension and (d) a continuous patterned film from a concentrated suspension. Figure taken from Ref. 2.

After casting the film and as the drying proceeds, there is a difference in the evaporation rates between the masked and unmasked regions. The evaporation rate is higher in the unmasked areas, and in the masked areas it approaches zero. The water flows inward to regions of higher evaporation to replace the fluid loss, as the film should be kept flat, due to surface tension. Furthermore, this flow carries also particles and hence this results in accumulation of particles below the open regions. The accumulation of the particles explains the observed patterns. In addition, it is observed that if the initial suspension is dilute, the final film has discrete patterned features (Fig. 2(c)). On the other hand if the initial suspension is concentrated, a continuous patterned film is prepared (Fig. 2(d)).

In order to determine the minimum feature size, the diffusion time is compared to the convection time, through the Peclet number,

$$P_e = \frac{t_{dif}}{t_{con}} = \frac{u_x (P - d_h)}{2D_0} \qquad (5)$$

where u_x is the horizontal particle velocity,

$\frac{u_x (P - d_h)}{2}$ is the distance from the centre of a masked region to a hole edge,

D_0 is the Stokes-Einstein diffusion coefficient.

It is shown that, this can be expressed also as:

$$P_e = \frac{J_{free} d_h (P - d_h)}{4\rho D_0 h_i} \qquad (6)$$

where J_{free} is the evaporative flux of the freely evaporative film

ρ is the fluid density

On the other hand, when $P_e > 1$, convection dominates and there is pattern formation. On the other hand, when $P_e < 1$, diffusion dominates and hence the pattern formation is hindered. Consequently, smaller features can be patterned either by increasing the evaporation flux, which depends on d_h, P, temperature and humidity or by decreasing the D_0.

Moreover, not only single-compound colloidal suspensions have been studied in the evaporative lithography process, but also binary.[3] In this case the colloidal suspension contains a blend of microspheres and naoparticles. In the initial stages of drying, both the microspheres and the nanospheres are transported to unmasked regions, where the evaporation rate is higher. As the drying proceeds, the microspheres start to consolidate in a closed-packed network. This network has small interstitial pores (Fig. 3). The nanoparticles are able to migrate through these, at the initial steps of drying, with the flow of water and later due to capillary tension at the liquid menisci among the particles.

(a) (b)

Figure 3 (a) Interstitial pores formed between closed-packed microspheres and surrounding nanoparticles in binary mixtures of high aspect radio. (b) Schematic illustration of a magnifiled side view of resulting binary film produced from initial suspension that contains high concentration of colloidal microspheres (grey spheres) and a dilute concentration of nanoparticles (green spheres). Figure taken from Ref. 3.

Finally, in addition to aqueous colloidal suspensions, also nongaseous suspensions.[4] have been studied by evaporative lithography. When a mask with holes is placed above that suspension, due to evaporative cooling, the unmasked areas are cooler than the masked. This temperature gradient leads to a surface tension gradient and hence to recirculating flow cells (Fig. 4(a)). The final pattern on the surface depends on the initial volume fraction of the suspension. On the one hand, for volume fraction below 0.22, the particles concentrate below the unmasked regions due to the circulating flow cells. (Fig. 4(b)). Consequently, the final pattern of the surface is the negative of the drying mask. On the other hand, for higher volume fraction, fluid flows from masked to the unmasked regions, particle convection occurs and hence the particles accumulate below the holes. This mechanism is analogous to the one that occurs in the aqueous suspensions.

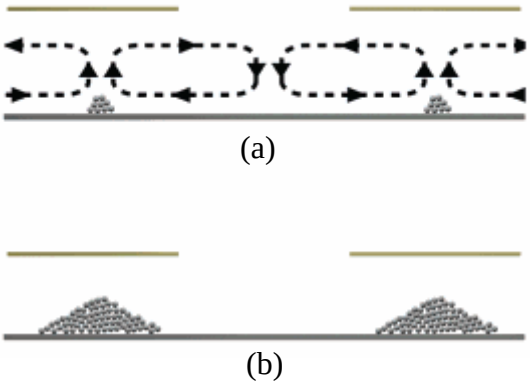

Figure 4 Schematic presentation (a) of the recirculating flow cells formed in drying nonaqueous suspensions below a mask with holes and (b) of the patterns formed for volume fractions up to 0.22. Figure taken from Ref. 3.

1.2.4 Examples

Examples of (i) unary aqeous, (ii) binary aqeous and (iii) unary nonaquoeus films obtained through evaporative lithography are shown in Fig. 5.

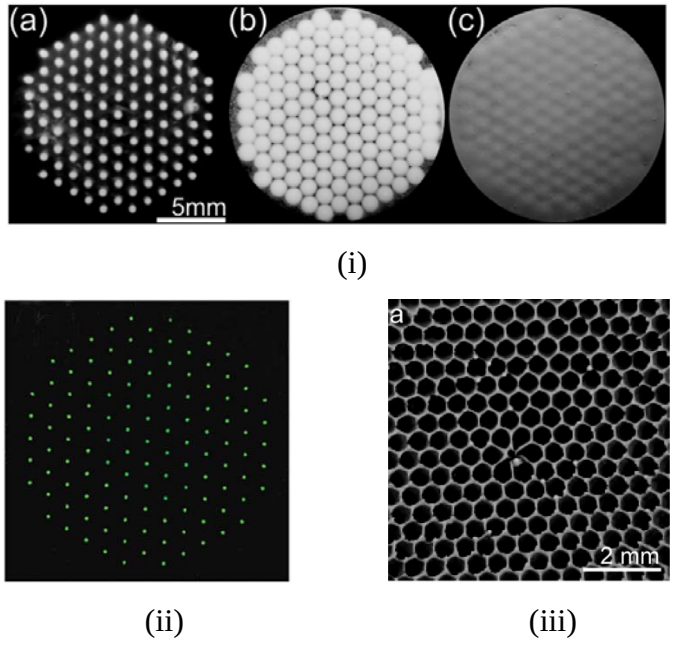

Figure 5 Films obtained by evaporative lithography prepared from: (i) unary aqeous colloidal suspension of silica microspheres with volume fractions (a) 0.05 (b) 0.1 and (c)

0.3 (optical images). Figure taken from Ref. 2. (ii) binary aqueous suspension of silica microspheres and fluorescent sulphonated polystyrene nanoparticles (fluorescence images). Figure taken from Ref. 3. (iii) unary suspension of silica microspheres in ethanol, with 0.001 volume fraction (optical image). Figure taken from Ref. 4.

1.2.5 Limitation of the technique

When evaporative lithography is used with hard latex particles, film formation will not occur. The dried film would be opaque, brittle and full of cracks. Another limitation of this technique is that the patterns are limited in term of design and complexity.

References

1. Routh, A. F.; Russel, W. B., Horizontal drying fronts during solvent evaporation from latex films. *AIChE Journal* **1998,** 44, (9), 2088-2098.

2. Harris, D. J.; Hu, H.; Conrad, J. C.; Lewis, J. A., Patterning Colloidal Films via Evaporative Lithography. *Physical Review Letters* **2007,** 98, (14), 148301.

3. DANIEL J. HARRIS; CONRAD, J. C.; LEWIS, J. A., Evaporative lithographic patterning of binary colloidal films. *Phil. Trans. R. Soc. A* **2009,** 367, 5157–5165.

4. Harris, D. J.; Lewis, J. A., Marangoni Effects on Evaporative Lithographic Patterning of Colloidal Films. *Langmuir* **2008,** 24, (8), 3681-3685.

1.3 Coffee-Stain Effect

Deegan, R. D. et. al.[1] had reported that coffee-stain effect or ring formation in an evaporating sessile drop is a hydrodynamic process in which solids dispersed in the drop are advected to the contact line. After all the liquid evaporates, a ring-shaped deposit is left on the substrate that contains almost all the solute. They show that the drop itself can generate one of the essential conditions for ring formation to occur: contact line pinning. Furthermore, they show that when self-induced pinning is the only source of pinning an array of patterns—that include cellular and lamellar structures, saw tooth patterns, and Sierpinski gaskets—arises from the competition between dewetting and contact line pinning. A a photograph of a dried coffee drop in Figure 1.

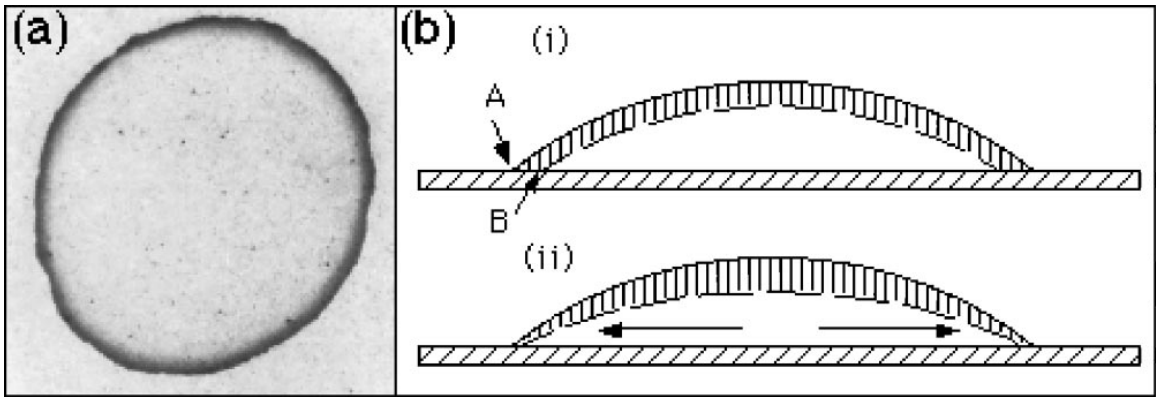

Figure 1 (a) A photograph of a dried coffee drop. The dark perimeter is produced by a dense accumulation of coffee particles. The radius is approximately 5 cm. (b) Schematic illustration of the origin of the advective current. (i) If the contact line were not pinned, uniform evaporation would remove the hashed layer, the interface would move from the solid line to the dashed line, and the contact line would move from *A* to *B*. However, if the contact line is pinned then the retreat from *A* to *B* is not possible, and there must be a flow that replenishes the lost fluid. (ii) Shows the actual motion of the interface and the compensating current.

Eral, H. B. et. al.[2] study the influence of electrowetting on the formation of undesired solute residues, so-called coffee stains, during the evaporation of a drop containing non-volatile solvents. Electrowetting is found to suppress coffee stains of

both colloidal particles of various sizes and DNA solutions at alternating (AC) frequencies ranging from a few Hertz to a few tens of kHz. Figure 2 shows two main effects which have been shown to contribute to the suppression: (i) the time-dependent electrostatic force preventing pinning of the three phase contact line and (ii) internal flow fields generated by AC electrowetting counteract the evaporation driven flux and thereby prevent the accumulation of solutes along the contact line.

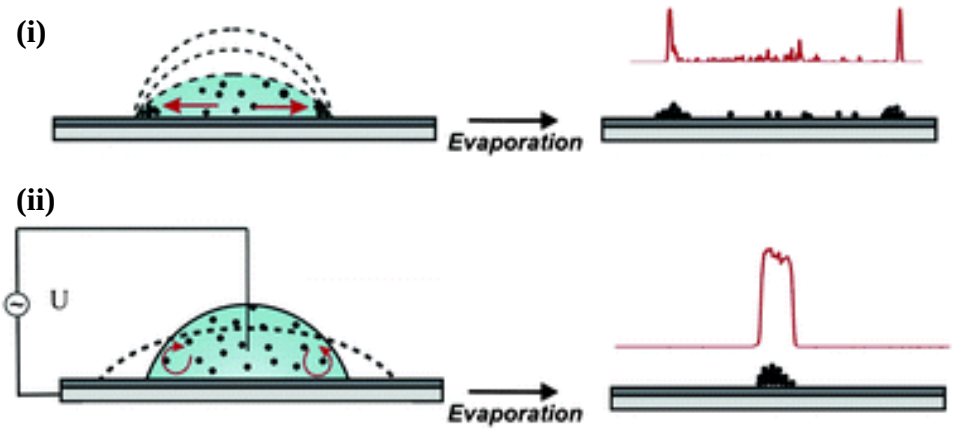

Figure 2 Two main effects are shown to contribute to the suppression: (i) the time-dependent electrostatic force prevents pinning of the three phase contact line and (ii) internal flow fields generated by AC electrowetting counteract the evaporation driven flux and thereby prevent the accumulation of solutes along the contact line.

Kajiya, T. et. al.[3] propose an experimental procedure for visualizing the solute concentration profile by combining the fluorescent microscopy with the lateral profile observation in the drying process of polymer solution droplets. They have conducted a dynamical observation of the transport process of the solute polymer toward the edge that causes the “coffee stain phenomenon”. They have found that the polymer concentration increases sharply near the edge, while it remains almost constant in the central region until the last stage of drying. The method is useful to understand the dynamical process that occurs near the contact line.

Berteloot, G. et. al.[4] propose a simple model of the dynamics of a contact line under evaporation and partial wetting conditions, taking into account the divergent nature of evaporation near the contact line, as evidenced by Deegan et al. (Nature, 389 (1997) 827). They show that evaporation can induce a non-negligible change of the contact angle together with modification of the flow near the contact line. They apply our results to dip-coating of a substrate with non volatile solutes. They show that at small velocities the coating thickness increases and scales like the inverse of the square of the velocity which implies a minimum of the coating thickness at the cross-over with the more familiar Landau-Levich regime.

References

1. Deegan, R. D., Pattern formation in drying drops. *Physical Review E* 2000, 61, (1), 475-485.

2. Eral, H. B.; Augustine, D. M.; Duits, M. H. G.; Mugele, F., Suppressing the coffee stain effect: how to control colloidal self-assembly in evaporating drops using electrowetting. *Soft Matter* 2011, 7, (10), 4954-4958.

3. Kajiya, T.; Kaneko, D.; Doi, M., Dynamical Visualization of "Coffee Stain Phenomenon" in Droplets of Polymer Solution via Fluorescent Microscopy. *Langmuir* 2008, 24, (21), 12369-12374.

4. Berteloot, G.; Pham, C. T.; Daerr, A.; Lequeux, F.; Limat, L., Evaporation-induced flow near a contact line: Consequences on coating and contact angle. *Europhysics Letters* 2008, 83, (1), 14003.

1.4 Cellulose nanocrystals (CNC)

1.4.1 Definition

Cellulose nanocrystals are highly crystalline, rigid, rod-like particles obtained by controlled hydrolysis of cellulose with strong acids. These particles, also known as cellulose whiskers, are very small with lengths between a few hundred nanometers to several micrometers and diameters from <5 to 20 nanometers, depending on the source of cellulose.[1-3]

The first report of cellulose whiskers was made by Ranby and co-workers[4] in the 1951s. Subsequent research by Battista and Smith[5] in 1957 led to the development and commercialization of microcrystalline cellulose (MCC). MCC is obtained by subjecting cellulose to hydrochloric acid and has found widespread use in the food and pharmaceutical industries. In addition, the properties of cellulose nanocrystals (mechanical, optical, and morphological) have inspired several research projects.[3]

1.4.2 Preparation

Cellulose nanocrystals/whiskers are generally obtained by reacting purified cellulose starting materials with mineral acids, such as sulfuric or hydrochloric acid, using moderate conditions. As mentioned earlier, amorphous cellulose regions are more susceptible to degradation by the hydronium ions than the crystalline regions, because these regions have a less ordered structure and are less densely packed. The most important parameters in the acid-catalyzed hydrolysis of cellulose are the type and concentration of the acid, temperature, and reaction time. The reaction is quenched by the addition of water to dilute the acid, which must thereafter be removed to avoid further cellulose degradation. Generally, centrifugation and extensive dialysis are used for this purpose. The result is an aqueous suspension of cellulose nanocrystals.

Araki and co-workers studied the effects of surface charge on the colloidal stability of cellulose nanocrystal suspensions.[6] They used sulfuric and hydrochloric acids to hydrolyze bleached softwood Kraft pulp and found that the higher surface charge density of the sulfuric acid-treated samples (84 mmol of sulfate esters/kg of dry material and 26 mmol of carboxyl groups/kg of dry material) compared to the samples treated with hydrochloric acid (< 18 mmol of weak acid groups/kg of dry material) resulted in higher colloidal stability. In a subsequent study, Araki et al.[7] used a post-sulfation

process with 55 wt % sulfuric acid to generate a negative surface charge on HCl hydrolyzed cellulose whiskers and observed a colloidal stability for the post-sulfated suspensions close to that of suspensions prepared by H_2SO_4-hydrolysis.

Around the same time, Dong et al. studied the effects of hydrolysis conditions on the surface charge of cellulose nanocrystals.[8] They varied the parameters during the H_2SO_4-hydrolysis of cotton fibers and observed a reduction in length and increase in surface charge with increasing reaction time. Several years later, a similar study by Beck-Candanedo et al.[9] investigated the effects of hydrolysis time and acid-to-pulp ratio on the properties of nanocrystals from hardwood and softwood cellulose. In the case of softwood cellulose, a longer hydrolysis time (45 min.) produced shorter whiskers with lower polydispersity. For both cellulose types, a higher acid-to-pulp ratio (17.5 mL/g) generated whiskers with smaller dimensions. In addition, the hardwood and softwood nanocrystals were found to have similar characteristics and the sulfate groups attached to the surface of the nanocrystals were found to be thermally unstable.

More recently, Elazzouzi-Hafraoui et al.[10] analyzed cellulose nanocrystals from cotton cellulose, tunicate cellulose, and MCC (Avicel) by atomic force and transmission electron microscopy (AFM and TEM), as well as small- and wide-angle X-ray scattering (SAXS and WAXS) and found that the particles were flat with a broad length distribution but with uniform thickness. The differences in observed dimensions from those previously reported by Dong et al.[8] and Araki et al.[6] were attributed to the fact that the particles were aggregates of smaller crystallites and that this fact was not taken into consideration in the previous studies.

The use of statistically designed experiments for the optimization of the hydrolysis reaction parameters and isolation of cellulose nanocrystals was reported by Bondeson et al.[11] in 2006. The group employed response surface methodology (MODDE 7, Umetrics) with acid concentration (H_2SO_4), mass of cellulose starting material (MCC), hydrolysis temperature, hydrolysis time, and time of ultrasonic treatment as factors, and yield and median particle size as responses. The reaction conditions that maximized the yield while producing a particle size close to 0.15 μm were an acid concentration of 63.5% sulfuric acid, a hydrolysis temperature of 44 °C, and a hydrolysis time of 130 min. Under these conditions, the mean particle size was 0.2 μm (as measured by laser

granulometry) and the yield was 30 %. However, it was suggested that the optimum values for the reaction parameters would be different for different cellulose sources. Also, the effect of sonication on the two responses was not obvious and considered a potential topic for future research.[2, 10, 11]

1.4.3 Morphology

The morphological aspects of cellulose nanocrystals have inspired numerous studies involving diverse analytical techniques. For example, Heux et al.[12] reported the use of solid state 13C nuclear magnetic resonance (NMR) spectroscopy to investigate the structure of sugar beet pulp microcrystals. NMR spectroscopy was useful to measure cellulose crystallinity under tightly controlled conditions, but it was difficult to extract information about the size of the microcrystals from the NMR results. Terech et al.[13] used SAXS to analyze the shape of cellulose whiskers obtained from tunicate cellulose. They performed measurements at six different concentrations of cellulose nanocrystals and found no particle aggregation within the concentration range used in their study. The cellulose whiskers exhibited rod-like shapes with high aspect ratios and had average dimensions of 5.9 nm (diameter) and 1 μm (length).

De Souza Lima and co-workers reported the use of polarized (DLS) and depolarized dynamic light scattering (DDLS) to analyze the translational and rotational dynamics of cellulose whiskers obtained from cotton and tunicate cellulose.[14] Their results for tunicate whiskers, which were based on the Broersma model,[15-17] were largely in agreement with those of Terech et al., except with respect to whisker diameter, which was more than double that reported by Terech et al. The measured dimensions were 15 and 16 nm in diameter and 255 and 1160 nm in length for cotton and tunicate whiskers, respectively.

AFM is the analytical technique that has probably provided the most detail on the morphology of cellulose nanocrystals. The use of AFM to analyze the structure of cellulose nanocrystals at the sub-nanometer scale was reported by Baker et al.[18, 19] High resolution images of cellulose whiskers obtained from the cellulose of the marine alga Valonia ventricosa revealed that the whiskers were straight, cylinder-like particles with corrugations on their surface, and lengths on the order of thousands of nanometers with 20 nm (a few) to 100 nm (majority) diameters. By using real and simulated AFM

images, the atomic arrangement on the whisker surface was found to be a mixture of triclinic and monoclinic domains. The AFM studies also revealed the presence of intra-chain periodicities of 0.52 nm, corresponding to the glucose units, and 1.04 nm for the cellobiose units.

Kvien and co-workers[20] used AFM, bright-field transmission electron microscopy (TEM), and field-emission scanning electron microscopy (FE-SEM) to analyze the size and shape of cellulose nanoparticles obtained from MCC and found that the particles had a needle-like shape with thinner diameters at the ends. The measured dimensions were a length of 210 ± 75 nm and a diameter of 5 ± 2 nm. Of the three methods, FE-SEM was found to have insufficient resolution and provided little information about the morphology of the cellulose whiskers.

Table 1 Dimensions of cellulose nanocrystals from various cellulose sources.[21] (Adapted from ref 21)

Cellulose source	Length (nm)	Width (nm)	Technique
Bacterial	100-1000	10-50	TEM
Cotton	100-150	5-10	TEM
Cotton	150-210	5-11	AFM
MCC	35-265	3-48	TEM
Ramie	150-250	6-8	TEM
sisal	100-500	3-5	TEM
Soft wood	100-150	4-5	AFM
Hard wood	140-150	4-5	AFM
Tunicate	1000-3000	15-30	TEM

It is now commonly accepted that the morphology of cellulose nanoparticles depends on the source of cellulose used and the reaction conditions of the acid-catalyzed hydrolysis. In a recent review, Gardner et al.[22] published a collection of typical cellulose whisker dimensions for several cellulose sources, obtained from different literature reports (Table 1). As seen in Table 1, the length of cellulose nanocrystals ranges from hundreds of nanometers to several microns and the cross-sectional dimension from a few to several tens of nanometers. Nanoparticles obtained from cellulose produced by bacteria, algae, or tunicates exhibit the largest dimensions.

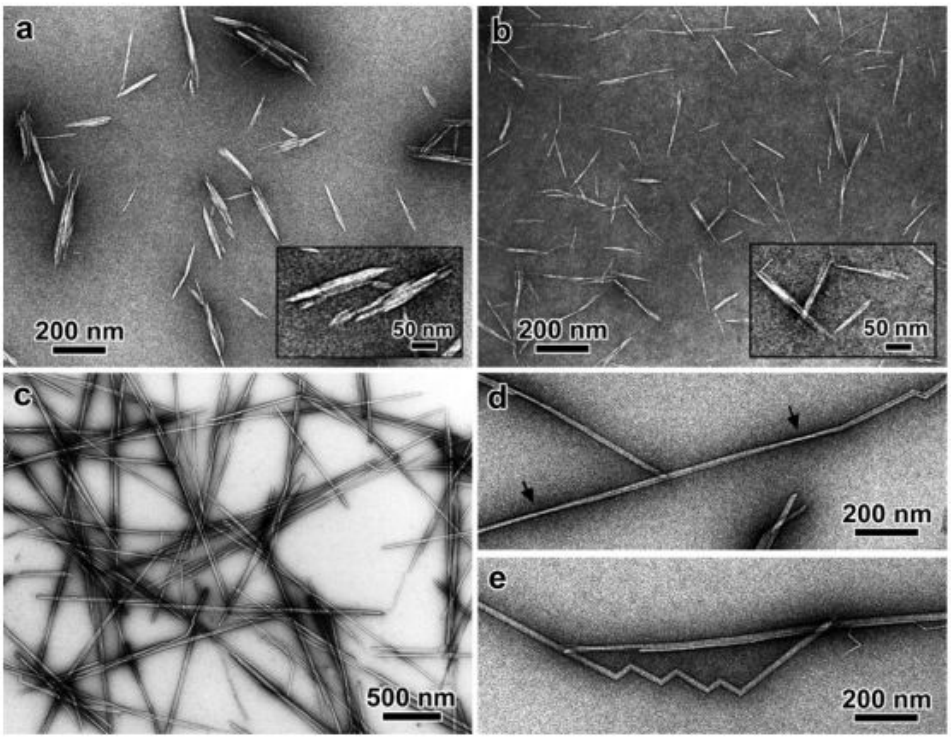

Figure 1 TEM micrographs of negatively stained cellulose whiskers obtained by sulfuric acid hydrolysis of cotton (a), Avicel (b), and tunicate (c-e) cellulose. Insets: enlarged views of some characteristic particles. The arrows in (d) indicate zones where the whiskers are seen edge-on. Picture taken from Ref. 10.[10]

Figure 1 shows TEM images of nanocrystals obtained from various cellulose sources by sulfuric acid-catalyzed hydrolysis. The images clearly illustrate the difference

in dimensions of whiskers from different cellulose sources. It is also evident that the shape of the particles varies from needle-like to cylindrical. However, the surface morphology of the nanocrystals is not apparent in these images.

1.4.4 Properties

1.4.4.1 Chiral nematic behavior

Several studies have reported that suspensions of cellulose whiskers spontaneously form optically active, chiral nematic (also "cholesteric") liquid crystalline phases when the whisker concentration rises above a critical value. Above this concentration, the previously randomly oriented cellulose nanoparticles orient themselves parallel to their neighbors and form a quasi-layered structure in which the direction of orientation rotates slightly from layer to layer in a helical fashion (Figure 2).

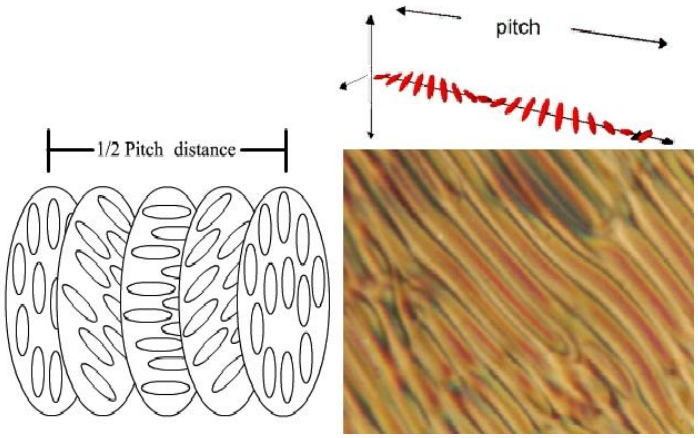

Figure 2 Chiral nematic structure formed by rod-like particles. Picture taken from Ref. 23.[23]

An important property of cholesteric structures is the pitch (*P*), which is defined as the length, perpendicular to the layers, required for the particles to complete a 360° degree rotation. When the value of (*P*) from the cholesteric helix coincides with the wavelength of light passing through the material, the structure exhibits selective reflection properties. The pitch of a cholesteric structure is related to the wavelength of the reflected light by the equation proposed by de Vries[24]:

$$\lambda = nP\sin(\varphi) \qquad (1)$$

where λ is the wavelength of the reflected light, n is the average refractive index, P is the pitch in nanometers, and φ is the angle of incidence. According to equation (1), as the angle of incidence changes, so does the reflected wavelength, i. e., the color for visible light. Thus, chiral nematic structures, such as those observed in concentrated cellulose nanocrystal suspensions, exhibit iridescent interference colors.[1, 25, 26]

Gray[25] observed that for suspensions of cellulose whiskers, obtained from bleached Kraft wood pulp, the critical concentration was 3 wt %, above which the suspensions form two phases: (a) an anisotropic, i. e. chiral nematic, one located at the bottom of the phase-separated suspension, and (b) an isotropic (randomly oriented) phase, located at the top.[25] Gray reported that these optical properties were also observed in some cellulose derivatives, and were sensitive to many factors, such as the nature of the side-groups, degree of substitution, molecular weight of the cellulose derivative, temperature, type of solvent, and the cellulose derivative concentration.

The chiral nematic order of liquid crystalline phases observed in cellulosic derivatives can be trapped in a solvent-swollen gel after partial removal of the solvent by a variety of techniques, including casting films from a mesophase solution and cross-linking the solvent of the cholesteric phase.[25]

1.4.5 Optical Properties of CNC

1.4.5.1 Iridescence

Iridescence is an optical phenomenon where the apparent color of the object depends upon the viewing angle of the observer. It is often seen in the world of biology, such as in the butterfly wings, carapaces of beetles, and in sea shells. The mechanism of iridescence has been extensively studied in the cases of various creatures for over a century. In 1927, using only optical microscopy, Mason[27] studied the structure of the butterfly wing and concluded that multilayer systems were primarily responsible for the iridescence present in the wing. The invention of electron microscopy then allowed for this phenomenon to be studied in greater detail than was possible before. Anderson et al. in 1942[28] observed similar optical results as Mason by using SEM. In general the

iridescence of butterfly wings is caused by the multilayer structure as opposed to pigmentation. Interference from these structures produces the observed colors.

Iridescence studies also have been done on sea shells,[29] as well as on spider and beetle exoskeletons.[30] In a review article, Seago et al.[31] classfied the iridescence observed in beetles into three groups based on its origins: multilayer reflection, three-dimensional photonic crystal, and diffraction grating behaviour.

The iridescent properties of CNC films were first reported by Revol et al.[32] in 1998 when studying the casting process of CNC suspensions under controlled conditions. They found that a solid films produced by these casting showed iridescence. This phenomena was later explained using a theory from de Vries[24] on the basis of a helicoidal arrangement of birefringent layers. De Vries postulated that the reflected wavelength depends upon the helical pitch of the chiral nematic liquid crystal arrangement. When the magnitude of the pitch is on the order of the wavelength of the incident light, satisfying the condition $\lambda = nP$, where n is the average refractive index of the material and P is the helical pitch of the liquid crystal, then only a narrow wavelength band of the light will be reflected. De Vries limited his discussion to the case of normal incident propagation light. Revol et al.[32] subsequently extended de Vries' relationship, and concluded that an approximate relationship of $nP\cos\theta = \lambda$ could be adopted for the oblique angle situation, where, θ being the angle between the viewing angle and the normal vector of the surface. Thus, a sample with a black background that reflects red light when viewed at normal incident to the surface would appear green when viewed at 45 º

It can be seen from the de Vries equation that the reflected iridescence color depends mainly on the pitch of the chiral nematic structure. The pitch itself can be altered by changing many different parameters, the first being ionic strength. Dong et al.[33] studied the effect of adding various electrolytes such as HCl, NaCl and KCl during the phase separation of CNC produced during acid-hydrolysis. They found that by increasing the ionic strength of the positively charged particles, the pitch formed by the anisotropic phase of CNC LC decreases. This induces a blue-shift in the reflected light of an CNC suspension when it is cast into a solid film. The decrease in pitch was explained as a product of the reduction of the double layer thickness caused by the repulsive forces

that exist between chiral nematic CNC particles. CNC crystals synthesized by acid hydrolysis have many sulfate groups on the surface of the cellulose molecules; adding electrolytes is analogous to adding counterions to the suspension. This has the effect of neutralizing the surface charge of the CNC particles in the anisotropic phase and reduces the repulsive forces. It was found that the amount of electrolyte that can be added is limited to a low concentration; high concentrations make the suspension unstable.

Later, Dong et al.[8] extended their study by adding inorganic counterions such as K^+, Na^+, Cs^+, and H^+ as well as organic ones such as ammonium, tetramethylammonium, tetraethylammonium, tetrapropylammonium, tetrabutylammonium, trimethylammonium, and triethylammonium to the CNC suspension. They found that for inorganic counterions the critical concentration for formation of the ordered phase increases in the order of $H^+ < Na^+ < K^+ < Cs^+$. For the organic counterions the critical concentration in general increases with increasing counterion size, suggesting that the equilibrium is governed by a balance between hydrophobic attraction and steric repulsion forces. Adding counterions also decreases the pitch of the CNC chiral nematic phase as determined by a polarized microscopy.

The pitch can be affected by other parameters including CNC concentration, temperature, and applied magnetic field, as studied by Pan et al.[34] They showed that the pitch increased with the CNC concentration. This was explained by the fact that increasing the concentration will increase the anisotropic phase volume and an increased suspension concentration promotes the formation of proportionately more anisotropic phase. As the volume fraction of the anisotropic phase increases, so does the pitch of the chiral nematic phase. By increasing the temperature, they found that pitch was reduced; the increased temperature will enhance the flexibility of the cellulose molecules in CNC, allowing for a greater twist angle. Finally, by drying the CNC under an applied 0.2 Tesla magnetic field an elongated pitch was observed. The increase in chiral nematic pitch may be due to the magnetic alignment of cellulose crystallites, given their anisotropic shapes and nonzero magnetic susceptibilities. This may cause the tilt angle between the directors in adjacent pseudo layers to decrease[35, 36], Similar effects have been observed for other liquid crystals.[37] The pitch data in these studies were obtained by measuring the maximum reflection Circular Dichroism (CD) peak value.

1.4.5.2 Selective circular polarized reflection

Another unique optical property of CNC is that it selectively reflects left circularly polarized light, meaning that the material has a stronger reflection for left-handed polarized light than for right-handed polarized light. This property is referred to as optical activity and applies to all chiral nematic liquid crystal molecules, as it is derived from the interaction of chiral materials with polarized light.

Like other chiral nematic materials CNC has strong optical activity, in the range of 103 to 105 deg/mm. The optical activity is measured as the angle of polarization vector rotation when linear polarized light passes through a medium. As with the iridescence exhibited by CNC films, the selective reflection of circular polarized light has also been explained by de Vries. In his model, de Vries[24] proposed that liquid crystals consist of a large number of thin layers and that light is reflected at the successive boundaries formed by these layers. Reflection at the boundary of two layers can only occur when there is a difference between the refractive indices of these layers, meaning that the medium can be thought of as a stack of double-refractive thin layers. This reflection occurs because the linear components of the light wave passing through one layer will observe a change in the refractive index of the medium when passing into the next layer. The fast component will be reflected with phase reversal, and the other component is reflected without reversal. Constructive interference will occur when the reflected electric field components are in phase with one another. From his model, de Vries concluded that only one handedness of circular polarized light can be selectively reflected by a chiral structure.

1.4.5.3 Circular Dichroism (CD) and Induced Circular Dichroism (ICD)

Circular Dichroism (CD) is a measure of the optical activity of chiral molecules and is quantified by the absorption difference between left circularly polarized light and right circularly polarized light by a chiral medium.

$$CD = AL - AR \qquad (2)$$

where, AL is the absorption of left-handed Circular Polarized Light (CPL) and AR, the absorption of right-handed CPL. As CNC is pure crystalline cellulose it has no chromophore[38]; absorption by the material is negligible at visible wavelength. Instead the selective reflection of CNC has been widely considered as a source of CD. If a chiral nematic sample predominantly reflects left-handed CPL then the total amount of light transmitted through the sample will be reduced by the amount of reflected light, resulting in the apparent selective absorption of left CPL. The magnitude of the CD will therefore be positive which is characteristic of a left-handed helical structure. Given that CD quantities can be directly related to material structure, in particular the chiral nematic pitch, by measuring the CD across a wide spectrum one can gain insights into the molecular structure of CNC.

The shape of a CD band depends on the degree of order and the texture of the mesophase. A uniform planar texture gives a sharp CD band, whereas a structure composed of chiral nematic polydomains yields a broad CD band.[39]

Induced circular dichroism (ICD) refers to circular dichroism that is induced by the interaction of an achiral compound interacting with chiral molecules. This effect is produced by a combination of the intermolecular forces, the properties of the chiral molecule in question, and even on the chromophore itself. The ICD technique has been widely used both as a probe for determining the interaction between chiral and achiral molecules[40] and to measure the chirality of chiral matrices.[41] CNC has been shown to display induced CD for specific dye compounds.[26]

References

1. de Souza Lima, M. M.; Borsali, R., Rodlike Cellulose Microcrystals: Structure, Properties, and Applications. *Macromolecular Rapid Communications* **2004,** 25, (7), 771-787.

2. Azizi Samir, M. A. S.; Alloin, F.; Dufresne, A., Review of Recent Research into Cellulosic Whiskers, Their Properties and Their Application in Nanocomposite Field. *Biomacromolecules* **2005,** 6, (2), 612-626.

3. Fleming, K.; Gray, D. G.; Matthews, S., Cellulose Crystallites. *Chemistry – A European Journal* **2001,** 7, (9), 1831-1836.

4. Ranby, B. G., Fibrous macromolecular systems. Cellulose and muscle. The colloidal properties of cellulose micelles. *Discussions of the Faraday Society* **1951,** 11, 158-164.

5. Orlando A Battista; Smith, P. A. Level-off d.p. cellulose products. US 2978446 A, 1957.

6. Araki, J.; Wada, M.; Kuga, S.; Okano, T., Flow properties of microcrystalline cellulose suspension prepared by acid treatment of native cellulose. *Colloids and Surfaces A: Physicochemical and Engineering Aspects* **1998,** 142, (1), 75-82.

7. Araki, J.; Wada, M.; Kuga, S.; Okano, T., Influence of surface charge on viscosity behavior of cellulose microcrystal suspension. *Journal of Wood Science* **1999,** 45, (3), 258-261.

8. Dong, X. M.; Gray, D. G., Effect of Counterions on Ordered Phase Formation in Suspensions of Charged Rodlike Cellulose Crystallites. *Langmuir* **1997,** 13, (8), 2404-2409.

9. Beck-Candanedo, S.; Roman, M.; Gray, D. G., Effect of Reaction Conditions on the Properties and Behavior of Wood Cellulose Nanocrystal Suspensions. *Biomacromolecules* **2005,** 6, (2), 1048-1054.

10. Elazzouzi-Hafraoui, S.; Nishiyama, Y.; Putaux, J.-L.; Heux, L.; Dubreuil, F. d. r.; Rochas, C., The Shape and Size Distribution of Crystalline Nanoparticles Prepared by Acid Hydrolysis of Native Cellulose. *Biomacromolecules* **2007,** 9, (1), 57-65.

11. Bondeson, D.; Mathew, A.; Oksman, K., Optimization of the isolation of nanocrystals from microcrystalline cellulose by acid hydrolysis. *Cellulose* **2006,** 13, (2), 171-180.

12. Heux, L.; Dinand, E.; Vignon, M. R., Structural aspects in ultrathin cellulose microfibrils followed by 13C CP-MAS NMR. *Carbohydrate Polymers* **1999,** 40, (2), 115-124.

13. Terech, P.; Chazeau, L.; Cavaille, J. Y., A Small-Angle Scattering Study of Cellulose Whiskers in Aqueous Suspensions. *Macromolecules* **1999,** 32, (6), 1872-1875.

14. De Souza Lima, M. M.; Wong, J. T.; Paillet, M.; Borsali, R.; Pecora, R., Translational and Rotational Dynamics of Rodlike Cellulose Whiskers. *Langmuir* **2002,** 19, (1), 24-29.

15. Broersma, S., Viscous force and torque constants for a cylinder. *J. Chem. Phys.* **1981,** 74, (12), 6989-6990.

16. Broersma, S., Rotational Diffusion Constant of a Cylindrical Particle. *J. Chem. Phys.* **1960,** 32, (6), 1626-1631.

17. Broersma, S., Viscous Force Constant for a Closed Cylinder. *J. Chem. Phys.* **1960,** 32, (6), 1632-1635.

18. Baker, A. A.; Helbert, W.; Sugiyama, J.; Miles, M. J., High-Resolution Atomic Force Microscopy of NativeValoniaCellulose I Microcrystals. *Journal of Structural Biology* **1997,** 119, (2), 129-138.

19. Baker, A. A.; Helbert, W.; Sugiyama, J.; Miles, M. J., New Insight into Cellulose Structure by Atomic Force Microscopy Shows the IÎ± Crystal Phase at Near-Atomic Resolution. *Biophysical Journal* **2000,** 79, (2), 1139-1145.

20. Kvien, I.; Tanem, B. r. S.; Oksman, K., Characterization of Cellulose Whiskers and Their Nanocomposites by Atomic Force and Electron Microscopy. *Biomacromolecules* **2005,** 6, (6), 3160-3165.

21. Habibi, Y.; Lucia, L. A.; Rojas, O. J., Cellulose Nanocrystals: Chemistry, Self-Assembly, and Applications. *Chemical Reviews* **2010,** 110, (6), 3479-3500.

22. Gardner, D. J.; Oporto, G. S.; Mills, R.; Samir, M. A. S. A., Adhesion and Surface Issues in Cellulose and Nanocellulose. *Journal of Adhesion Science and Technology* **2008,** 22, (5-6), 545-567.

23. http://www.iq.usp.br/mralcant/AboutLC.html.

24. De Vries, H., Rotatory power and other optical properties of certain liquid crystals. *Acta Crystallographica* **1951,** 4, (3), 219-226.

25. Gray, D. G., Chiral nematic ordering of polysaccharides. *Carbohydrate Polymers* **1994,** 25, (4), 277-284.

26. Edgar, C.; Gray, D., Induced Circular Dichroism of Chiral Nematic Cellulose Films. *Cellulose* **2001,** 8, (1), 5-12.

27. Mason, C. W., Structural Colors in Insects. II. *The Journal of Physical Chemistry* **1926,** 31, (3), 321-354.

28. Anderson, T. F.; Richards, A. G., An Electron Microscope Study of Some Structural Colors of Insects. In 1942; Vol. 13, pp 748-758.

29. Brink, D. J.; van der Berg, N. G.; Botha, A. J., Iridescent Colors on Seashells: an Optical and Structural Investigation of Helcion pruinosus. *Applied Optics* **2002,** 41, (4), 717-722.

30. Russell, S. T.; Ramnarine, I. W.; Mahabir, R.; Magurran, A. E., Genetic detection of sperm from forced copulations between sympatric populations of Poecilia reticulata and Poecilia picta. *Biological Journal of the Linnean Society* **2006,** 88, (3), 397-402.

31. Seago, A. E.; Brady, P.; Vigneron, J.-P.; Schultz, T. D., Gold bugs and beyond: a review of iridescence and structural colour mechanisms in beetles (Coleoptera). *J. R. Soc. Interface* **2009,** 6, (Suppl 2), S165-S184.

32. Revol, J.-F.; Godbout, L.; Gray, D. G., Solid self-assembled films of cellulose with chiral nematic order and optically variable properties. *Journal of Pulp and Paper Science* **1998,** 24, (5), 146-149.

33. Dong, X. M.; Kimura, T.; Revol, J.-F. o.; Gray, D. G., Effects of Ionic Strength on the Isotropic-Chiral Nematic Phase Transition of Suspensions of Cellulose Crystallites. *Langmuir* **1996,** 12, (8), 2076-2082.

34. Pan, J.; Hamad, W.; Straus, S. K., Parameters Affecting the Chiral Nematic Phase of Nanocrystalline Cellulose Films. *Macromolecules* **2010,** 43, (8), 3851-3858.

35. Meyer, R. B., DISTORTION OF A CHOLESTERIC STRUCTURE BY A MAGNETIC FIELD. *Appl. Phys. Lett.* **1969,** 14, (7), 208-209.

36. Hurault, J. P., Static distortions of a cholesteric planar structure induced by magnetic or ac electric fields. *J. Chem. Phys.* **1973,** 59, (4), 2068-2075.

37. Domenici, V.; Veracini, C. A.; Novotná, V.; Dong, R. Y., Twist Grain Boundary Liquid-Crystalline Phases under the Effect of the Magnetic Field: A Complete 2H and 13C NMR Study. *ChemPhysChem* **2008,** 9, (4), 556-566.

38. Dong, X. M.; Gray, D. G., Induced Circular Dichroism of Isotropic and Magnetically-Oriented Chiral Nematic Suspensions of Cellulose Crystallites. *Langmuir* **1997,** 13, (11), 3029-3034.

39. Yue, Z.; Cowie, J. M. G., Preparation and Chiroptical Properties of a Regioselectively Substituted Cellulose Ether with PEO Side Chains. *Macromolecules* **2002,** 35, (17), 6572-6577.

40. Zsila, F.; Bikadi, Z.; Simonyi, M. s., Induced circular dichroism spectra reveal binding of the antiinflammatory curcumin to human Î±1-acid glycoprotein. *Bioorganic & Medicinal Chemistry* **2004,** 12, (12), 3239-3245.

41. Guo, J. X.; Gray, D. G., Induced circular dichroism as a probe of handedness in chiral nematic polymer solutions. *Liquid Crystals* **1995,** 18, (4), 571-580.

1.5 Security Printing

The large increase in counterfeiting in recent years demonstrates the inadequacy of current anti-counterfeiting methods. It is prudent and advisable that more sophisticated security technology should be developed to maintain an edge over counterfeiters. By sophisticated, it is often understood to mean use of multilayered technologies consisting of both overt (readily visible to the naked eye) and covert (hidden and invisible without the use of special equipment and/or chemicals). They are difficult for counterfeiters to reproduce, yet easy for consumers and field investigators to verify information. There are many anti-counterfeiting techniques presently available to both the public at large and commercial interests, ranging from the simple to the sophisticated. Security features based on optical techniques are of particular interest, being difficult to replicate and relatively easy for customers to identify. The most popular optical security technologies are Optical Variable Device (OVD), selective reflection, and security inks.

1.5.1 Optical Variable Device (OVD)

The Optical Variable Device relies on changes in the optical properties of the material to certify the uniqueness of a brand. Color dependence on orientation properties are useful as a medium-level security method, as the image made of this material cannot be copied due to the fact that conventional copiers and scanners can only copy in a fixed direction. The most popular examples of OVDs are holograms, hidden images and iridescent images.

Holograms are one of the most well-known and easily recognizable anti-counterfeiting devices in the market. The first metalllised hologram to appear on an identity document was in 1984 on United Nations' passports: simple authentication devices on the cover.[1] Holograms are produced by recording the interference pattern created by two beams of coherent light, typically laser light. A hologram image is made up of microgrooves, which will diffract light and recreate the recorded image in the projected interference pattern.

Different types of holographic images can be formed depending on the techniques

used, namely 2D and 3D holograms. The former refers to a layering of 2D images to create the holographic object, while the latter refers to a real 3D image created using holograph recording techniques. A 3D hologram has an additional dimension realized by placing objects in the foreground, midground and background; extremely complex and secure designs can be created. A high volume of holograms can be produced by hot stamping, which makes this technique more favourable in terms of cost. Further, holograms produce vibrant, iridescent 3D images that cannot be reproduced by conventional imaging techniques.

Holograms can however be copied using mechanical means such as embossing. A skilled holographer can make copies that are very difficult to distinguish from the originals. For instance, it has been reported that more than half the sales of the drug artesunate in South East Asia are forged despite the use of holographic security.[2] Given time, any anti-counterfeiting technique can be duplicated and so companies should look to the future and work to develop more sophisticated measures. Another technique used for making a more secure OVD is the hidden image created by using computer- generated Fourier signals. Stepien et al.[3] proposed an approach to make such an OVD by including both a rainbow holographic effect and hidden Fourier-plane images. Under typical illumination, the first element shows rainbow holographic and kinematic effects while the second element shows up as a darker image visible at an angular range different than that of the first element, being less visible under usual white light illumination conditions but appearing sharp under laser light.

The advancement of Electron-beam (E-beam) lithographic techniques makes it possible to create high resolution microstructures for use in high security OVD design. R.A. Lee[4] proposed using color-tone lithography to create micro-mirrors having directionally-dependent color reflection. In this example, the micro-mirrors were designed in such a way that the dollar and euro symbol have alternating maximum reflection depending on the viewing angle (see Figure 1).

Figure 1. An artwork sample to be converted into an optically variable microstructure by the color-tone lithography process.[4]

1.5.2 Selective Reflection

Selective reflection as a security feature has been widely studied, although it is more often seen in disclosed patents than in published papers. A few typical examples of the use of selective reflection by chiral liquid crystals for security applications will be discussed. In US patent application No. 20100112314, Jiang et al.[5] disclose a method to make invisible ink using chiral liquid crystals. Security pigment systems are generally a composite of a reflective material, a transparent chiral birefringent material and a transparent carrier medium. The security pattern is invisible when viewed with naked eye but becomes visible as an achromatic bright mark on a dark background when viewed with a circular polarizer. Selective reflection by the chiral nematic pigment is the key to the aforementioned security feature.

Another example is a commercial product, called Helicone® made by SICPA. Helicone is a cholesteric liquid crystal polymer that has an additional secondary security feature that it selective reflects circular polarized light. NCC possesses iridescence; therefore it can be used as an OVD in the same manner as a hologram. Revol et al.[6] first proposed a method to make security paper by adding NCC planchette into the paper. The color variation properties make for a simple authentication method to determine the authenticity of the security paper.

1.5.3 Security Ink

As with selective reflection, security ink is another covert security feature that usually operates in the UV or infrared band. Security ink is used to print security images on various substrates. They cannot be seen under normal lighting conditions; imaging is triggered by light induction, thermal induction, or chemical induction. Security ink features have been widely used in various brands and product anticounterfeiting, including bank notes and consumer product protection. A brief review of these techniques will follow.

1.3.3.1 Light reaction ink

Light reaction ink changes color when exposed to a specific wavelength of light, typically achieved through UV or infrared fluorescence or phosphorescence. These inks can continue to emit for an extended period of time after exposure. A typical example of phosphorescent ink can be seen in glowing at the edge of stamp, as seen in Figure 2.

Figure 2. Green phosphorescent stamp.[7] Ink containing components which emit light after exposure to light of a specific wavelength (normal light or UV light). In phosphorescent materials the emission of light continues after cessation of the stimulated radiation (from 10^{-8} seconds to several seconds or hours) whereas fluorescence is a very short-lived emission which ceases within 10^{-8} seconds (fluorescent ink).

UV security inks are very popular today. Fluorescence from these inks can span from the visible to the infrared. They are widely used in bank notes and other official documents, and have been incorporated into almost all countries' banknote protection systems. Security paper is strictly controlled by the government; the paper being

nonfluorescent as it has no optical brightening Agent (OBA). This UV-insensitive paper is useful for two reasons: one, it provides a good background for fluorescent inks and two, it is easily distinguished from commercial brightened paper.[8]

Security inks can also be sensitive to IR excitation. This feature is of particular interest in that it takes advantage of the anti-Stokes emission where a shorter wavelength emission is generated by a longer wavelength excitation. Security features can be made by printing objects with both IR-active and IR-inactive ink. A typical example of this is barcode printing, where the two types of inks have been used to print the barcode simultaneously but the detectable portion is printed with IR-inactive ink. A counterfeiter who reproduced the whole visible barcode would in fact have made the wrong pattern.

1.3.3.2 Thermal reaction ink

Thermal-reactive inks change color when the temperature of the ink print substrate area is changed. Such inks can often be activated by body temperature or friction, a property that cannot be reproduced by a copier. A typical example of thermochromic ink that changes colour in a reversible way at different temperatures, as seen in Figure 3.

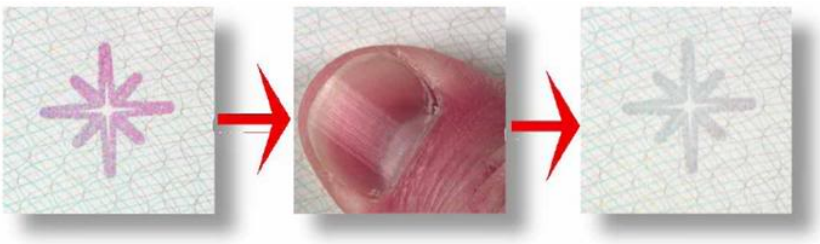

Figure 3 Special ink that changes colour in a reversible way at different temperatures.[7]

1.3.3.3 Chemical reaction security ink

Chemically reactive inks are also important; they are particularly useful for deterring forgers who may try to re-use the security ink by recovering it with solvent. When exposed to solvents such as bleach, alcohol, or acetone these inks will run, change color, or cause a stain to develop. Tampering is easily detected when chemicals or solvents are used on these inks. The definite reaction of the ink to solvent can be used as

a forensic test to determine authenticity, but this is an inherently destructive verification method. Security inks may also degrade naturally over time, depending on the chemical structure.

References

1. Lancaster, I., Innovation drives hologram document protection: New developments prove potent weapon in battle against ID counterfeiting *Keesing Journal of Documents & Identity* **2013**, p. 11-15.

2. Paul N. Newton; Facundo M. Fernandez; Aline Plancon; Dallas C. Mildenhall; Michael D. Green; Li Ziyong; Eva Maria Christophel; Souly Phanouvong; Stephen Howells; Eric McIntosh; Paul Laurin; Nancy Blum; Christina Y. Hampton; Kevin Faure; Leonard Nyadong; C. W. Ray Soong; Budiono Santoso; Wang Zhiguang; John Newton; Palmer, K., A Collaborative Epidemiological Investigation into the Criminal Fake Artesunate Trade in South East Asia. *PLoS Medicine* **2008,** 5, (2), 0209-0219.

3. Pawel J. Stepien; Remigiusz Gajda; Szoplik, T., Computer-generated optically variable devices containing hidden information. *Proc. SPIE 2659, Optical Security and Counterfeit Deterrence Techniques* **1996,** 218, http://dx.doi.org/10.1117/12.235466

4. Lee, R. A., Colourtone lithography. *Microelectronic Engineering* **2002,** 61â€“62, (0), 105-111.

5. Jiang, Y.; Hochbaum, A., Invisible Pigments and Ink. *US 2010/0112314 A1* **2010**.

6. Revol, J.-F.; Godbout, L.; Gray, D. G., Solid self-assembled films of cellulose with chiral nematic order and optically variable properties. *Journal of Pulp and Paper Science* **1998,** 24, (5), 146-149.

7. http://forum-percetakan.blogspot.de/2009_08_01_archive.html.

8. R.D. Warner; Adams, R. M., *Introduction to Security Printing*
PIA/GATF Press: Pennsylvania, 2005.

1.6 Buckling Instability

The buckling instability during drying of sessile drops of polymer solution was reported by L. Pauchard et al.[1] They found that the large shape distortions that occur during the drying of sessile drops of polymer solution are shown to be related to a buckling instability. As solvent evaporates, polymers accumulate near the vapor/drop interface and, depending on the experimental conditions, can form a glassy skin which bends as the volume it encloses decreases. A comparison of the times that characterize drying kinetics and glassy skin formation enables us to predict instability occurrence. Good agreement is found with measurements performed at different polymer concentrations, drop volumes and drying rates. Lateral views showing stable (a) and unstable (b) evolutions of Dextran solution drops deposited on a glass slide are shown in Figure 1.

As polymer solutions dry, high-concentration gradients form near the vapor/solution interface.[2] Depending on the physicochemical properties of the system concerned, the outer layer, with the higher polymer concentration in, can undergo a glass transition. L. Pauchard et al.[1] claims that the formation of this glassy skin is the cause of a buckling instability. In fact if the outer layer becomes glassy, it behaves as an elastic shell which, however, does not impede evaporation. This shell bends as the volume it encloses decreases, while its surface remains constant.

In fact, as for colloids, polymer deposition and adhesion onto the substrate leads to a strong pinning of the three-phase line: the drop evaporates with a constant contact area with the substrate, contrary to a pure solvent drop, which recedes with a constant contact angle. To understand the influence of the polymer concentration, two different drop shape evolutions are observed. At low concentrations (see fig. 1. a-1), the drop progressively flattens with solvent evaporation and the apex height steadily decreases. In the final stage, a flat “pancake” forms, with a depressed central zone for the lowest concentrations. On the contrary, if the concentration is high enough, the drop shape is severely distorted (see fig. 1 b-1). After a steady decrease, the apex height starts to decrease and can reach a value greater than its initial value. In the final stage, the drop shows the shape of a “Mexican hat”.

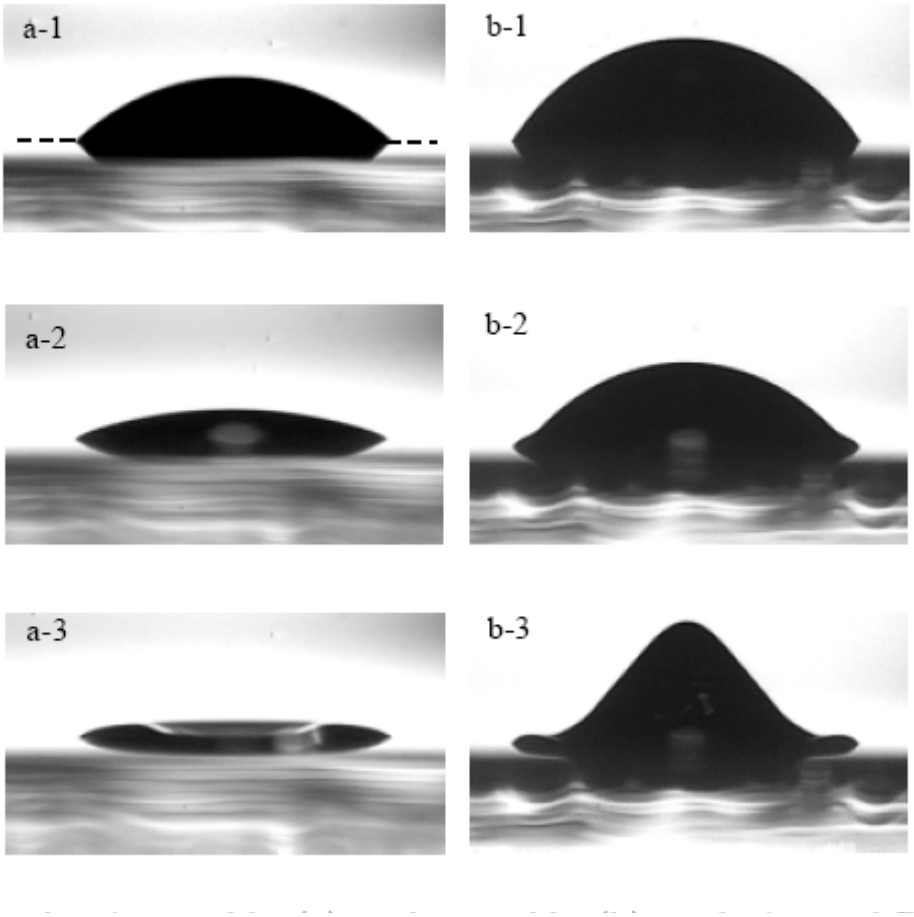

Figure 1 Lateral views showing stable (a) and unstable (b) evolutions of Dextran solution drops deposited on a glass slide. (a) Polymer concentration ω_p = 0.20 g/g: (a-1) just after deposition; the dotted line corresponds to the drop/substrate contact, the drop base diameter is 4mm, it remains constant during drying. (a-2) 6 minutes after deposition: the drop steadily flattens. (a-3) End of drying: the drop forms a flat "pancake". (b) Polymer concentration ω_p = 0.40 g/g: (b-1) just after deposition. (b-2) 6 minutes after deposition: just before instability beginning. (b-3) 7 minutes after deposition: the apex height has increased and reaches a peak leading to the typical "Mexican hat" shape at the end of drying.[1]

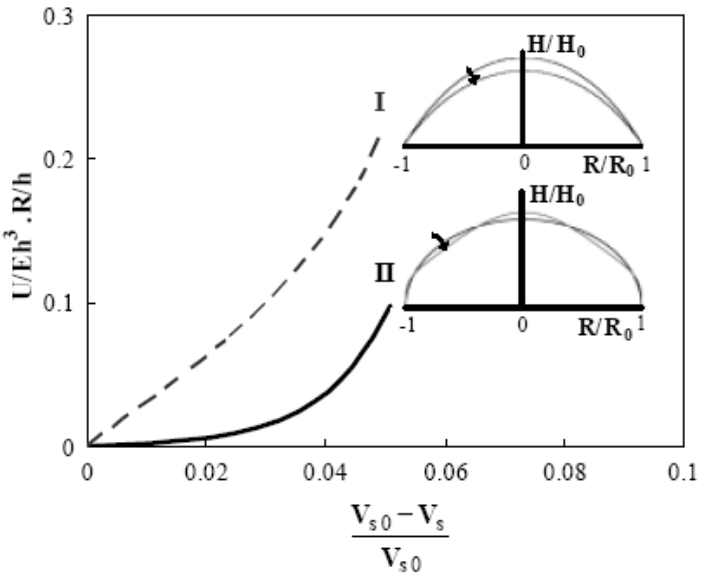

Figure 2 Dimensionless elastic energy ($U/Eh^3.R/h$) *vs.* relative volume (($V_{s0} - V_s$)/V_{s0}) in the case of two configurations: elastic shell flattening (I) and sinusoidal perturbation around a spherical cap shape (II). E is Young's modulus, h the shell thickness (assumed to be uniform and constant over time) and R the radius of curvature characteristic of the initial spherical cap shape. V_{s0} denotes the drop volume when the skin forms at the surface of the drop, V_s denotes the volume variation during buckling of the elastic shell. (The energy reference for a non-deformed shell is assumed to be 0).

To understand the formation of the "Mexican hat" shape, L. Pauchard et. al.[1] estimated the elastic energy for a thin elastic shell under the decrease of its inner volume. The energy of a spherical cap shape with hinge supports at the boundary, continuously flattening under the decrease of its inner volume, is denoted configuration I[3] (see fig. 3). They investigated a sinusoidal perturbation around a spherical cap shape which induces an axisymmetric change of curvature; this is called configuration II (Note that, in these calculations, the shell thickness, h, is supposed to be uniform, time independent and smaller than the other characteristic lengths involved in the problem. Moreover, h is assumed to be small enough to consider that the length change due to the curvature inversion (the external curvature becomes an internal curvature) has a low contribution to the total elastic energy compared to the bending contribution. The energy of

configuration I arises as a balance between two terms: the bending energy (concentrated near the circumferential boundary) and the stretching energy due to the compression of the sphericalcap region, found to be 10% higher than the former. The energy of contribution II is simply due to a bending effect concentrated in the axisymmetric circular fold. Comparison of the energies of both configurations shows configuration II to be energetically favorable (fig. 3). They show that experimental results are also well adjusted by this configuration.

L. Pauchard et. al.[1] also studied the influence of humidity on the buckling instability; indeed varying *RH* changes the drying rate and hence the skin thickness and drying stresses.[4] In his experimental conditions no change was observed in the t_B variations, showing that the instability is governed by glass skin formation.

Gorand, Y. et. al.[5] presented and discussed the very intriguing shapes of drops of a concentrated polymer solution while they dry. As the solvent evaporates, the outer layer of the drop which has a higher polymer concentration displays a glassy transition; an outer "skin" therefore builds up at the surface. This glassy skin behaves like an elastic solid shell which, however, does not block evaporation; this shell bends as the volume it encloses decreases.

To understand the influence of the initial contact angle of the sessile drop, different time variations of the shape are observed[5]:

For low contact angles ($\theta_0 < \theta c \cong 30°$), the drop progressively flattens following solvent evaporation (Figure 3a, $\theta_0 = 25°$). The drop shape is not strongly modified and its apex height decreases regularly, as displayed by the spatiotemporal diagram in Figure 3 ($\theta_0 = 25°$).

For all higher contact angles (Figure 3b and c, $\theta_{0c} < \theta_0$), a surface instability takes place and, following θ_0, this instability results in different drop shapes. Particularly, for intermediate contact angles such as $\theta_{0c} < \theta_0 < \theta_0^* \cong 60°$, the apex height decreases at first and then quickly increases back and reaches a value which may exceed the initial one (Figure 3b, $\theta_0 = 40°$). At the time when the apex height variation begins to differ from the regular trend (Figure 4, $\theta_0 = 40°$), the profiles get distorted (see the profile superposition in Figure 3b). Later, the drop surface area remains constant while its volume keeps decreasing but at a slower rate. At the final stage, the drop has the shape of

a “Mexican hat” (see the side view in Figure 3b). For higher contact angles ($\theta_0^* = 60° < \theta_0$), the apex height first decreases following the same trend as in the previous case and then decreases at a faster rate (Figure 4, $\theta_0 = 70°$). In this latter case, the final drop shape (see the side view in Figure 3c, $\theta_0 = 70°$) displays a circular fold, resulting in a dip at the center of the droplet, only observable on profilometry measurements[6] (Figure 5).

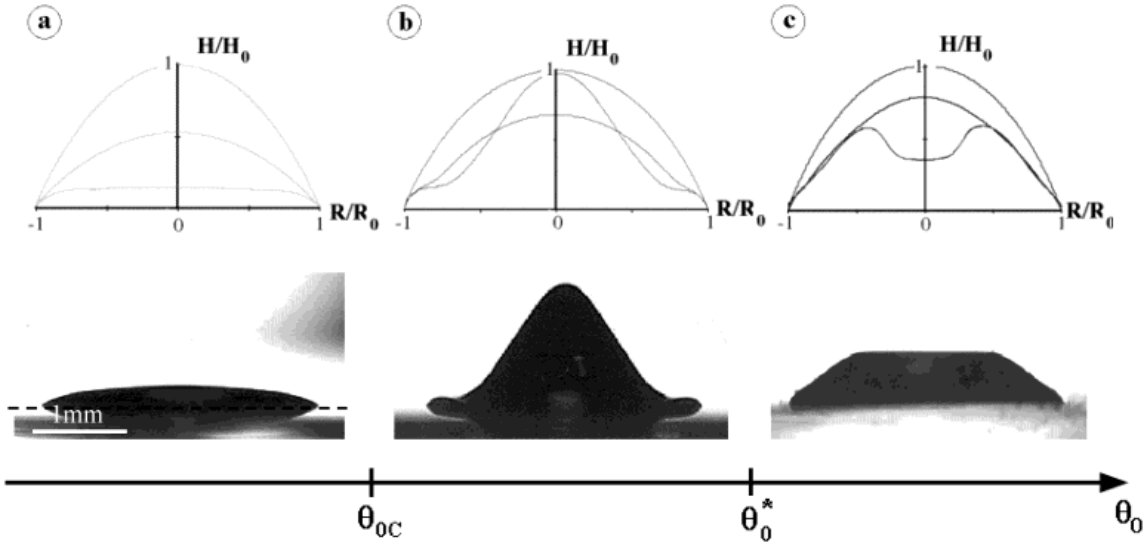

Figure 3 (top) Superposition of dimensionless profiles of sessile drops of dextran solutions recorded at different times during desiccation (RH) 50%). The time elapsed between two consecutive profiles is 300 s. The initial concentration is the same in all cases (ω_{p0}) 0.40 g/g), while the initial contact angle increases from case a to case c ((a): θ_0) 25°, H_0) 0.70 mm, R_0) 3.16 mm (stable case). (b): θ_0) 40°, H_0) 1.28 mm, R_0) 3.52 mm. (c): θ_0) 70°, H_0) 1.85 mm, R_0) 2.64 mm). Each drop remains axisymmetric. (below) Corresponding digitized side views of the sessile drops taken 1 h after the beginning of the experiment.[5]

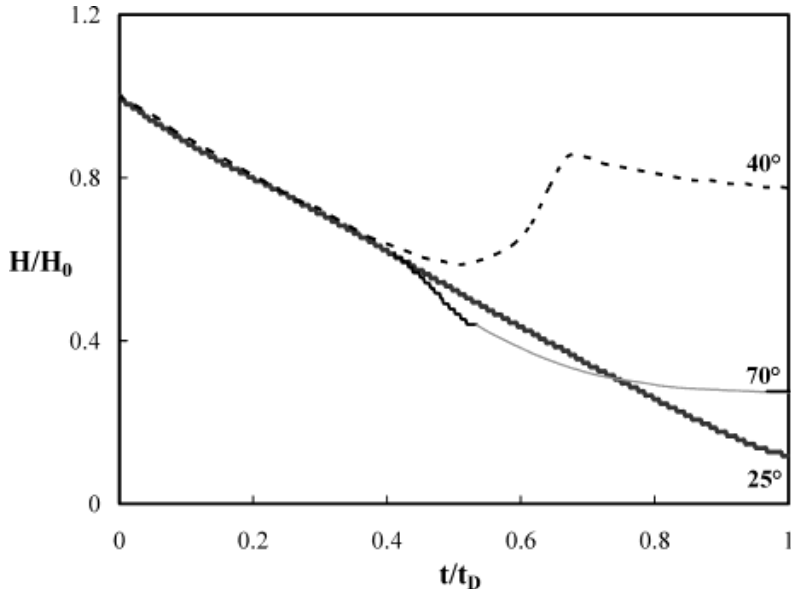

Figure 4 Time variations of the apex height in dimensionless coordinates for the three drop shapes a, b, and c described in Figure 1.8.3. H_0 is the drop apex height at $t = 0$, and t_D is the characteristic time of the desiccation process (time needed for the complete desiccation of pure water drops in the same conditions). The values of t_D are 1860, 2400, and 5500 s for $\theta = 25$, 40, and 70°, respectively. In the case of $\theta_0 = 70°$, the dark line corresponds to the experimental measurements, the gray one, to a guide for the eyes, and the horizontal bar at $t/t_D = 1$, to the value H/H_0 that has been measured by mechanical profilometry at $t/t_D >> 1$.[5]

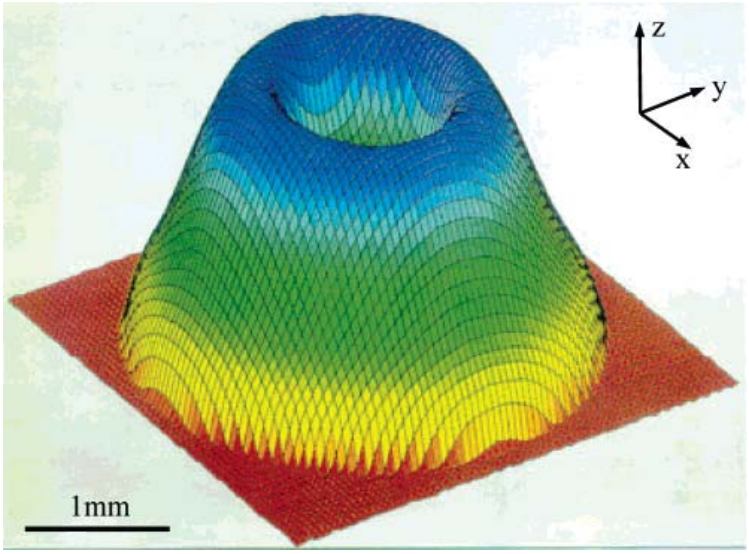

Figure 5 3D map of the drop corresponding to $\theta_0 = 70°$ (image c of Figure 3). This profile was measured using a mechanical profilometer (length scales are amplified in the *z* direction to improve legibility).[5]

References

1. L. Pauchard; Allain, C., Buckling instability induced by polymer solution drying. *Europhys. Lett.* 2003, 62, (6), 897-903.

2. Crank J. and Park G. S., *in Diffusion in Polymers*. Academic Press: 1968.

3. Landau L. D. and Lifshitz E. M., *in Theory of Elasticity*. Pergamon Press, New York: 1959.

4. de Gennes P. G., *Eur. Phys. J. E,* 2002, 7, 31.

5. Gorand, Y.; Pauchard, L.; Calligari, G.; Hulin, J. P.; Allain, C., Mechanical Instability Induced by the Desiccation of Sessile Drops. *Langmuir* 2004, 20, (12), 5138-5140.

6. Boffa, J. M. A., C.; Hulin, , *J. P. Eur. Phys. J.* 1998, AP2, 281.

1.7 The sol-gel process

The first review about the sol-gel process was reported by Hench.[1] *Sols* are dispersions of colloidal particles in a liquid. *Colloids* are solid particles with diameters of 1 - 100 nm. A *gel* is a interconnected, rigid network with pores of submicrometer dimensions and polymeric chains whose average length is greater than a micrometer. The term "gel" embraces a diversity of combinations of substances that can be classified in four categories as discussed by Flory[1]:

(1) well-ordered lamellar structures;

(2) covalent polymeric networks, completely disordered;

(3) polymer networks formed through physical aggregation, predominantly disordered;

(4) particular disordered structures.

Sumio had reported about preparation and properties of sol-gel coating films.[2] In the most sol-gel process, he start from a solution containing source compounds for the target materials as shown in Figure 1. The solution becomes a *sol* as a result of formation of fine colloidal particles or polymers and further reactions lead to gelation, that is, wet gel formation. In the course of sol-to-gel conversion, which takes place at low temperatures, coating, fiber drawing and molding into bulky shapes can be made. In many cases, a target material is obtained by heating a shaped gel at higher temperatures.

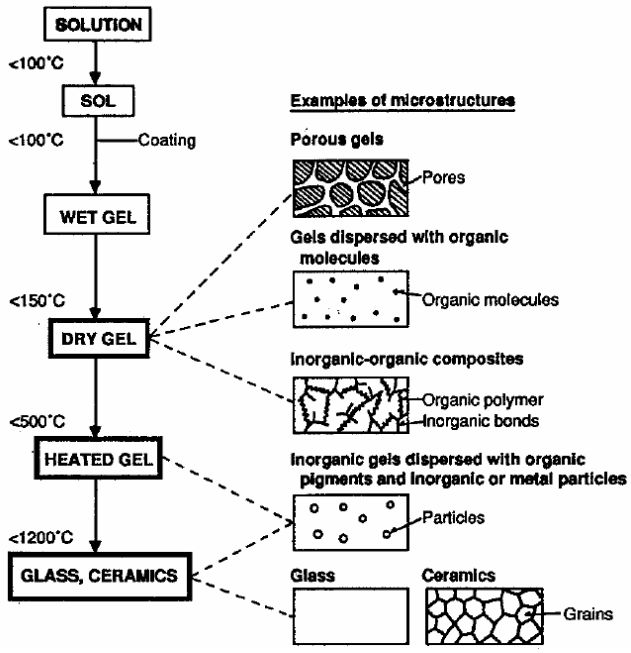

Figure 1 Block diagrams showing the sol-gel processes, processing temperatures and rnicrostructure of products.[2]

1.7.1 Sol–gel reactions[3]

The reaction is generally divided into two steps: hydrolysis of metal alkoxides to produce hydroxyl groups in the presence of stoichiometric water (usually in the presence of acid or base catalyst), followed by polycondensation of the resulting hydroxyl groups and residual alkoxyl groups to form a three-dimensional network as shown in Figure 2. Different metal alkoxides based on silicon, aluminum, transition metal alkoxides such as titanium and zirconium also have been used as sol–gel precursors in combination with a variety of organic components. For non-silicate metal alkoxides, no catalyst is needed for hydrolysis and condensation because these are very reactive themselves. The sequence of reactivity is expressed as follows:

$$\mathbf{Zr(OR)_4,\ Al(OR)_3 > Ti(OR)_4 > Sn(OR)_4 > Si(OR)_4}$$

However, owing to the loss of volatile by-products formed in the hydrolysis–condensation reactions, it is difficult to control sample shrinkage during three dimensional network formation.[4] Factors such as the nature of the alkyl group, solvent,

temperature, water to alkoxide molar ratio, presence of acid or base catalysts, etc., are known to effect the hydrolysis reaction.[5] For example, in the presence of base catalyst, the rate of condensation is fast compared to hydrolysis and results in the formation of dense, colloidal particles. On the other hand, the rate of condensation is slow relative to the rate of hydrolysis under acid catalysis and the resultant silica has a highly ramified, low fractal dimensional structure with many silanol groups on the silica surface.[6]

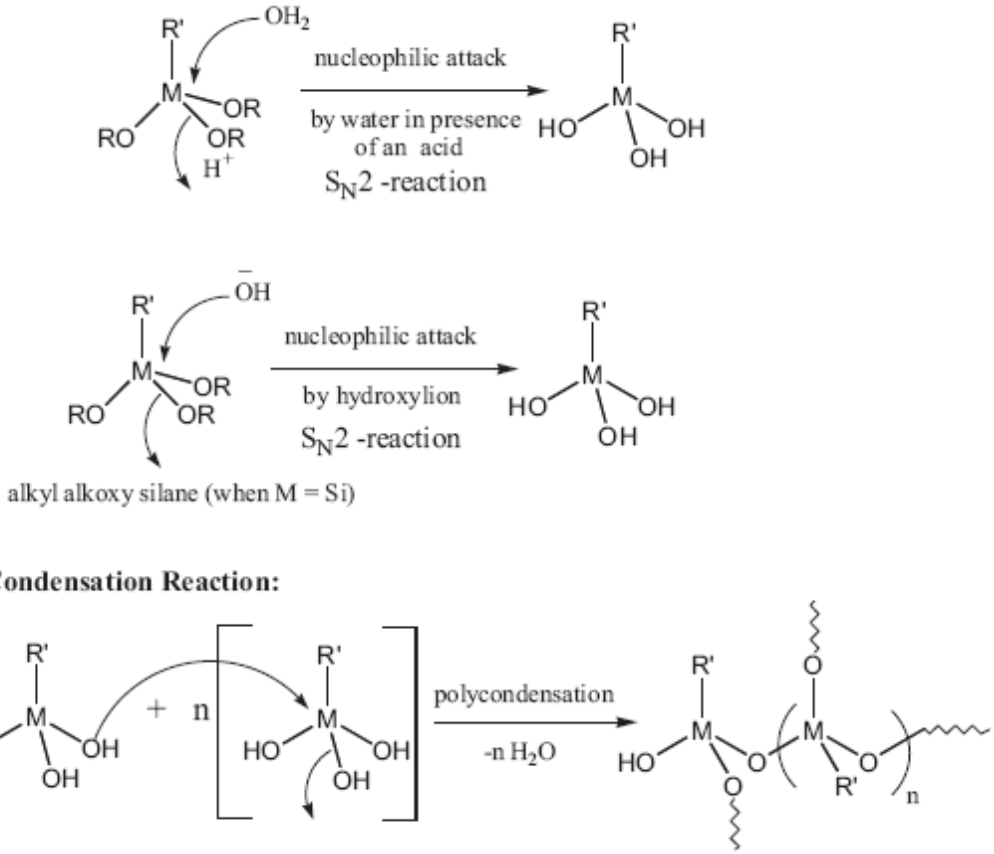

Figure 2 Sol-gel hydrolysis and condensation polymerization reaction[4]

The precursors of which compounds are organo-substituted silicic acid esters of general formula $R'_nSi(OR)_{4-n}$ and bridged precursors of silsesquioxanes $X_3Si–R`–SiX_3$ (X = Cl, Br, OR); where R` can be any organo functional group and is usually 1 or 2. If R` bears any reactive group that can, for example, polymerize or copolymerize (e.g.,

methacryloyl, epoxy, amino, isocyanate, vinyl or styryl groups) or undergo hydrolysiscondensation (trialkoxysilyl groups), it will act as a network former. Therefore, siloxane hybrids can be easily synthesized as the Si_2Csp^3 bonds are covalent and stable towards nucleophilic attack by water, alcohols, hydroxylated ligands, etc. They can be used, for example, as building blocks for the formation of highly ordered polyhedral oligomeric silsesquioxane (POSS) clusters[7, 8] and as organosilane coupling agents for ceramic particle coatings[9, 10] Some sol-gel precursors is shown in Figure 3.[11]

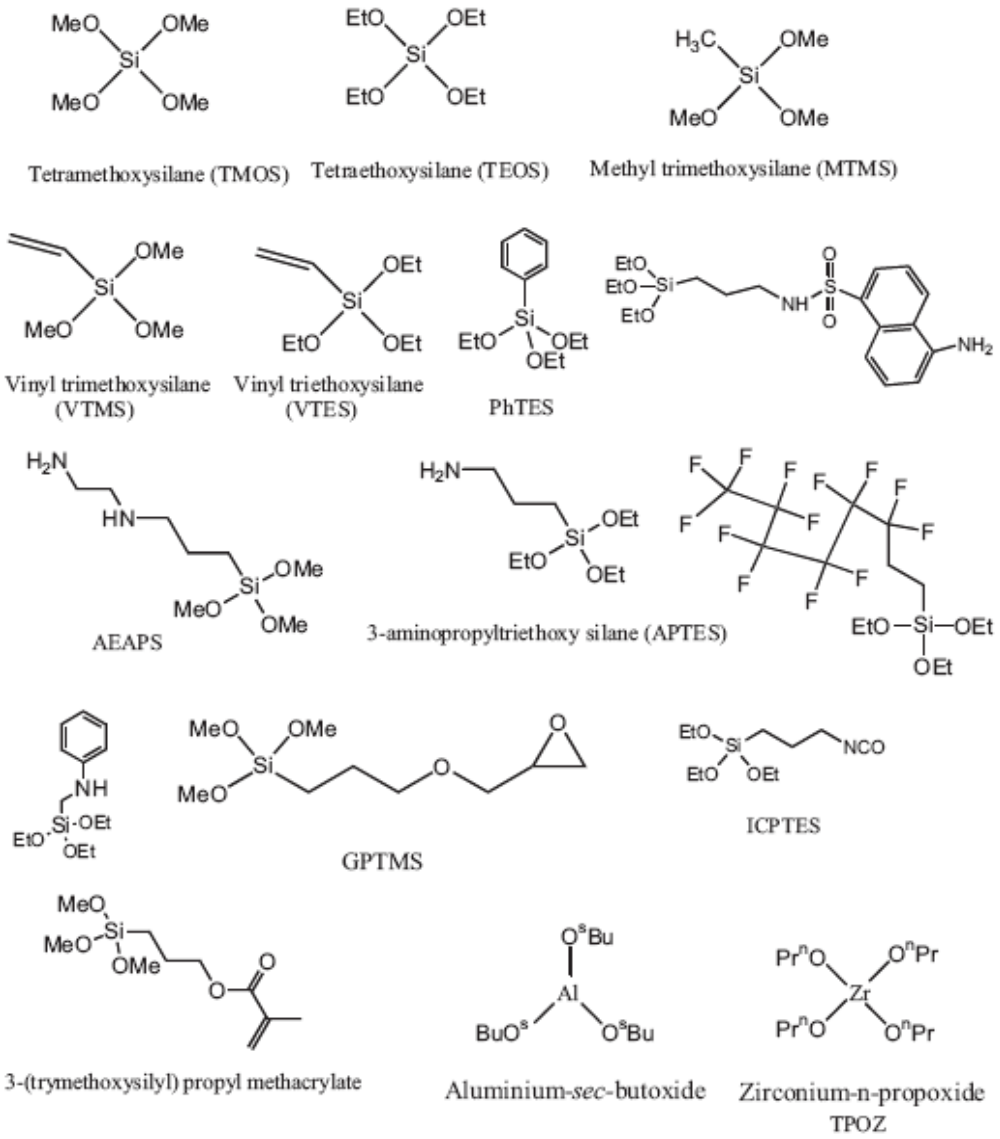

Figure 3 Different sol-gel precursors which used in coating applications.[12]

References

1. Hench, L. L.; West, J. K., The sol-gel process. *Chemical Reviews* **1990,** 90, (1), 33-72.

2. Sakka, S., Preparation and properties of sol-gel coating films. *Journal of Sol-Gel Science and Technology* **1994,** 2, (1-3), 451-455.

3. Zoromba, M. S. T. Preparation and Characterization of New Nanostructured Organic/Inorganic Composite Coatings for Anti-Fog Applications. Clausthal University of Technology, 2009.

4. Wen, J.; Wilkes, G. L., Organic/Inorganic Hybrid Network Materials by the Sol-Gel Approach. *Chemistry of Materials* **1996,** 8, (8), 1667-1681.

5. Tjong, S. C.; Chen, H., Nanocrystalline materials and coatings. *Materials Science and Engineering: R: Reports* **2004,** 45, (1-2), 1-88.

6. Goda, H.; Frank, C. W., Fluorescence Studies of the Hybrid Composite of Segmented-Polyurethane and Silica. *Chemistry of Materials* **2001,** 13, (9), 2783-2787.

7. Lichtenhan, J. D.; Vu, N. Q.; Carter, J. A.; Gilman, J. W.; Feher, F. J., Silsesquioxane-siloxane copolymers from polyhedral silsesquioxanes. *Macromolecules* **1993,** 26, (8), 2141-2142.

8. Matajka, L.; Dukh, O.; Brus, J. A. I.; Simonsick Jr, W. J.; Meissner, B., Cage-like structure formation during sol-gel polymerization of glycidyloxypropyltrimethoxysilane. *Journal of Non-Crystalline Solids* **2000,** 270, (1-3), 34-47.

9. Daniels, M. W.; Francis, L. F., Silane Adsorption Behavior, Microstructure, and Properties of Glycidoxypropyltrimethoxysilane-Modified Colloidal Silica Coatings. *Journal of Colloid and Interface Science* **1998,** 205, (1), 191-200.

10. Daniels, M. W.; Francis, L. F. In *Effect of curing strategies on porosity in silane-modified silica colloidal coatings*, Materials Research Society Symposium - Proceedings, 1999; 1999; pp 313-317.

11. Atanacio, A. J.; Latella, B. A.; Barbac, C. J.; Swain, M. V., Mechanical properties and adhesion characteristics of hybrid sol-gel thin films. *Surface and Coatings Technology* **2005,** 192, (2-3), 354-364.

12. Schottner, G., Hybrid Sol-Gel-Derived Polymers: An Applications of Multifunctional Materials. *Chemistry of Materials* **2001,** 13, (10), 3422-3435.

Chapter 2

Objectives and Structure of the Thesis

2.1 Thesis objectives

This thesis makes use of three major materials. One is dextran, a water-soluble polysaccharide polymer. The second one is polystyrene. And the last one is cellulose nanocrystals (CNCs), a material derived from wood pulp, as the basis of a more secure and less expensive anti-counterfeiting device.

The objectives of this thesis are:

- To guide the structure formation during drying of polymer films by heating with a laser.

- To introduce a new method to create the patterned polymeric surfaces with the concept of infrared assisted evaporative lithography.

- To evaluate the film properties of spin-coated CNC films impregnated with sol-gel solution by dip-coating method and spin-coating method.

- To explore the potential application for making a security printing by using cellulose nanocrystals blended with latex dispersion.

2.2 Thesis structure

This thesis is divided into seven chapters. A review of the relevant literature and thesis objective are given in Chapter 1 and 2, respectively. Chapters 3 through 6 reported in manuscript format. Chapter 7 presents an overall conclusion.

In chapter 3, we presented a simple method to induce elevations by locally heating a film with a laser. Most of the time, we added a dye to the material. The dye's absorption amounts to a localized heat source. Since the rate of evaporation is high at the irradiated spot, there is a flow of liquid towards the area of irradiated spot. In consequence, a "Mexican hat" develops. The phenomenon is related to what is called "evaporation lithography" in the literature. Novel about our work is the combined action of solvent flow and buckling. Buckling leads to a characteristic pattern, which is a rather small peak on top of a wider pedestal. Importantly, the buckling-induced features are narrower than the features induced by flow. We only found buckling when employing dextran and did not found in polystyrene. Presumably, buckling is the consequence of an elastic skin and hydrogen bonding. Apparently, such a skin resisting contraction is only formed by certain materials. For reasons which are not understood to date, the minimum

feature size is about 300 μm. The size of the laser spot only is a few tens of microns. Parameters affecting the profile structure such as diameter of laser spot, polymer concentration, molecular weight, dye content were investigated.

In chapter 4, we introduced a new method to create a patterned polymer surface base on the principle of infrared assisted evaporative lithography. In this experiment, we dried films on a 3M CG3700 polyester sheet (thickness 0.127 mm), which carried the black lines particled onto the back side. When drying a polystyrene film deposited onto the back side of this kind of substrate under an IR-lamp, the black lines absorbed heat. The films after drying showed elevations at the positions of the black lines. We characterized the profile structure by using profilometer and imageJ program. We also calculated the amplitude of surface profile by using FFT method. The parameters which effect on the raised feature such as the wet film thickness, the molecular weight of polymers and the dye content were investigated.

In chapter 5, we studied the films properties of CNC films coated with sol-gel solution films and CNC/latex blend films prepared by spin-coating on glass substrate. We found that both CNC films coated with sol-gel solution films and CNC/latex blend films are not re-dispersed in water, while pure CNC films are re-dispersed in water. When samples were immersed in water, the CNC films coated with sol-gel solution are not delaminated from glass substrate while CNC/latex blends films are delaminated. The hardness of the films was tested by pencil hardness tester. The refractive index of samples was measured by Abbe refractometer.

In chapter 6, we propose the use of a CNC latex blend as an ink for security printing. When printed onto dark paper, the letters are darker than the background if viewed without polarizers, while they are brighter than the background if viewed with crossed polarizers. We quantified the polarization effect in diffusion reflection and in-plane orientation. We found that the substrate effects on the sample orientation. If a rough substrate (such as paper) is the substrate, it will always be difficult to maintain a well-defined orientation after drying. The microscopic texture of samples was also investigated by polarized-light optical microscope and laser scanning confocal microscope.

In chapter 7, we presented the overall conclusions.

Chapter 3

Guided Structure Formation on Drying Polymer Films Building on the Combined Action of Evaporative Lithography and a Buckling Instability

Guided Structure Formation on Drying Polymer Films Building on the Combined Action of Evaporative Lithography and a Buckling Instability

*Chakkresit Chindawong and Diethelm Johannsmann**

Institute of Physical Chemistry, Clausthal University of Technology
39678 Clausthal-Zellerfeld, Germany

3.1 Abstract

Polymer films with small elevations were formed by locally heating the film during drying with a focused laser beam. The maximum achievable height was about 2-5 times of the film thickness. Characteristic differences were found between polystyrene films drying from toluene solution and dextran films from aqueous solution. The height profile of polystyrene is well described by a Gaussian. The minimum achievable full width at half height was about 200 μm which is about 5 times of the diameter of laser spot. Dextran films dried under similar condition develop a small cusp in the center. The cusp is about 100 μm wide. The cusp develops because of bucking. The technique therefore combines evaporative lithography with other previously reported techniques of the generation or topographical structures building on elastic instability. Contrasting to the previously demonstrated techniques, the location of cusp is precisely controlled by the preceding flow of the materials towards the center of the irradiated spot.

Keywords: *dextran, polystyrene, buckling instability, evaporative lithography*

3.2 Introduction

The formation of topographical structures at the surfaces of polymer coatings has a long history as well as many practical applications. Structures are often produced by printing or embossing. The structures also form spontaneously, which is of practical interest if the process is sufficiently controlled. An example of a commercially successful material undergoing such spontaneous processes is “cracquelure”. If properly formulate paints develop fine patterns of cracks within hours after application, thereby mimicking the appearance of paintings by old masters. A counter example is the orange skin. Surfactant (present in most water borne paints) has a tendency to give rise to Marangoni convection. If this happens the surface of film looks like an orange skin – as the name says – which is usually avoided.

A further large class of surface structures goes back to a rate of evaporation being different at different locations of the coating. The “coffee-stain effect” is widely known. The coffee-stain effect denotes an accumulation of material at the edge of a drying film on droplet. To be precise, there are two distinct reasons why material can driven towards the edge. The first one is an increased evaporation rate at the edge and a second one is a primed contact line which produces a flow towards the rim even if the evaporation rate is the same everywhere.[1]

Lateral flows driven by evaporation are also employed intentionally for the sake of structure formation. This technique as acquired the name “evaporative lithography”.[2, 3] Evaporative lithography (more generally, structure formation driven by evaporation) is often portrayed as characteristic feature of multiphase flows. The transport is driven a liquid with high vapour pressure. A second, on volatile phase is dragged along. Diffusion is too slow to re-establish a concentration equilibrium. Eventually, drying arrests the process, freezing in a non-equilibrium situation.

Allain[4] had reported about a buckling instability of dextran solution that related to the large shape distributions occurring drying the drying of sessile drops of polymer solution. As solvent evaporates, polymer accumulate near the vapour/drop interface and, depending on the experimental conditions, can form a glassy skin which bends as the

volume it encloses decreases. The instability occurrence was predicted by comparing the times that characterize drying kinetics and glassy skin formation.

Georgiadis[5] announced a techniques, which they named IR radiation-assisted evaporative lithography (IREAL), which uses the lateral flows in an aqueous dispersion of colloidal particles, driven by differences in evaporation rate created by IR radiative heating through a shadow mask to create polymer coatings with a periodic topographic pattern, repeating over millimetre length scales. They showed that the height of the surface features increases with an increase in several key parameters such as the initial thickness of the film, the volume fraction of particles, and the pitch of the pattern.

Chou and co-workers[6-8] discovered an intriguing pattern transfer technique named lithographically induced self-assembly (LISA). Their experiment showed that when a mask with protruded patterns was placed a certain distance above a flat polymer melt (polymethylmethacrylate (PMMA)), the polymer would be attracted to the below of mask protrusions. Thus the patterns had a lateral dimension identical to that of the mask protrusions. Similar observations on polystyrene were made by Schäffer et al.[9], however, under the condition that external electric field was applied between the mask and the polymer melt. Their fascinating results showed that using a mask to induce and pattern polymer films is a straightforward, feasible technique to fabricate submicrometer and possibly nanometer structures. J. Peng et al. have carried out a series of experiments under different conditions to optimize the process of LISA. Both polymethylmethacrylate (PMMA) and polystyrene (PS) films are perfectly patterned by LISA with the lateral length scales down to 500 nm. The mechanism of pattern transfer has been discussed in detail.[10, 11]

Keddie[12] reviewed the main experimental techniques used to study the film formation process. He presented the fundamental concepts for each of the three main stages of the process: evaporation of water, particle deformation, and polymer diffusion. The latest experimental observations are presented along with theoretical descriptions and models. The effects of surfactant on film properties and describe films made from nanocomposite particles and from blends of latex with nanoparticles, such as clays or carbon nanotubes were considered. The remaining technical challenges and highlighting a few exciting future directions are considered.

This work is mainly concentrated on comparison of the structure formation between a water-soluble polysaccharides, dextran, and polystyrene using light-induced structure formation during drying polymer films.

The use of dextran is proposed as a material which can form hydrogen bonding and has buckling instability induced by polymer solution drying. The use of polystyrene is an opposite material of dextran. The influences of molecular weight, the polymer concentration, the initial thickness of the film and the dye content on the structure formation were determined.

3.3 Materials and Experimental

3.3.1 Materials

There are two types of polymer materials used in this experiment. The first polymer is a water-soluble bacterial polysaccharide, Dextran. Three molecular weights (40,000, 70,000 and 200,000 g/mol) were used. The dextran from *Leuconostoc Spp*. are called Dextran40 (M_w = 40 kg/mol) and Dextran70 (M_w = 70 kg/mol) (were obtained from Sigma-Aldrich, Denmark) and Dextran200 (M_w = 200-300 kg/mol) (was obtained from Polycsience, Inc, Warrington, PA, USA), respectively. The glass transition temperature of dextran is 220 ^{0}C.[4] The second polymer is polystyrene (PS) which has four different molecular weights (59, 167, 228 and 319 kg/mol). The glass transition temperature of polystyrene is about 106 ^{0}C.[13] Toluene (Aldrich) and 1,4-dioxane (Sigma-Aldrich) were used as solvent for polystyrene. Congo red (Riedel-De Haen Ag, Seelze-Hannover, Germany)(λ_{max} = 498 nm, molar extinction coefficient is about 45,000 $(mol/L)^{-1}cm^{-1}$ and melting point is >360 ^{0}C) was used as dye for dextran and oil red EGN (Aldrich, USA) (λ_{max} = 521 nm, molar extinction coefficient is about 26,000 $(mol/L)^{-1}cm^{-1}$ and melting point is 130 ^{0}C) was used as dye for polystyrene. These materials were used as received with out further purification.

3.3.2 Profilometer

The profilometer (TENCOR P-1 long scan profiler) was used to measure the profile structure. The laser power meter (TPM-300CE gentec) was used to measure the diameter of laser spot. The diameter of laser spot exposed on the sample depends on the distance between the lens and sample, d. The polymer film after casting on the glass slide was placed on a stage under the lens. The laser used here is green laser pointer. The laser's wavelength is 532 nm and the peak power is about 5 mW (CLASS IIIa laser product).

3.3.3 Experimental setup

An apparatus was designed to measure the diameter of laser beam. The diameter of laser spot exposed on the sample depends on the distance between the lens and sample, d. The experimental setup for measuring the diameter of laser was shown in Figure 3.1.

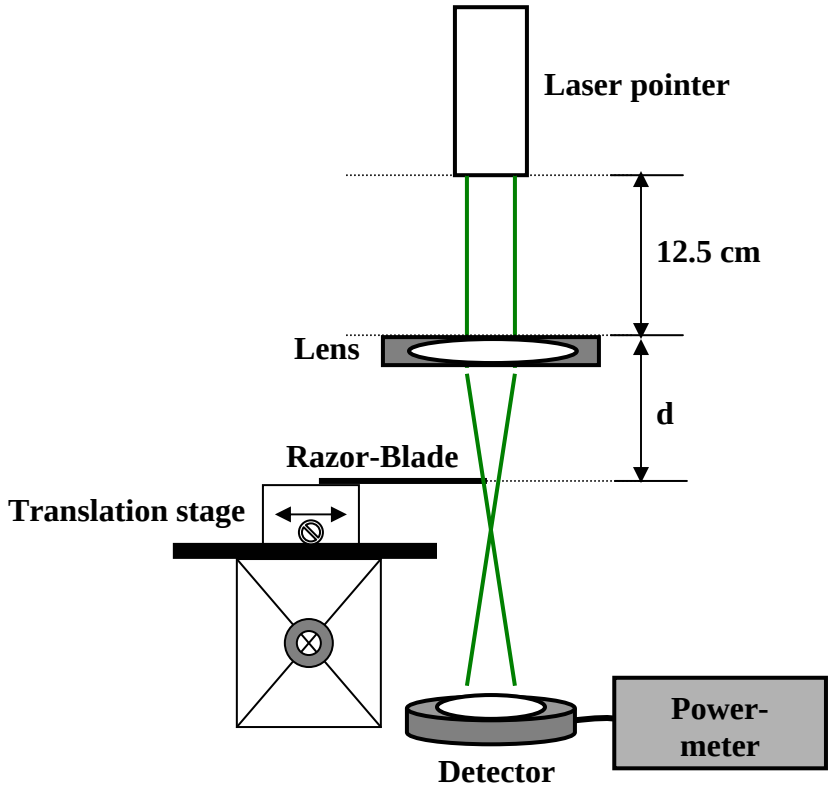

Figure 3.1 The experimental setup for measuring the diameter of laser spot.

Figure 3.2(a) shows schematic view of experimental setup of the laser induced structure formation during drying of polymer film. The key parameters are the initial thickness of the wet film, h_i, and the distance between lens and sample, d. Figure 3.2(b) shows schematic view of a peak structure formation on the polymer film in the exposed area.

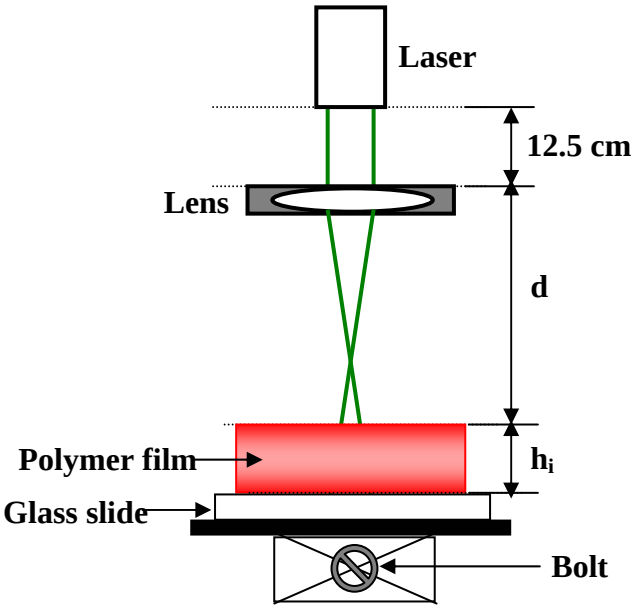

(a)

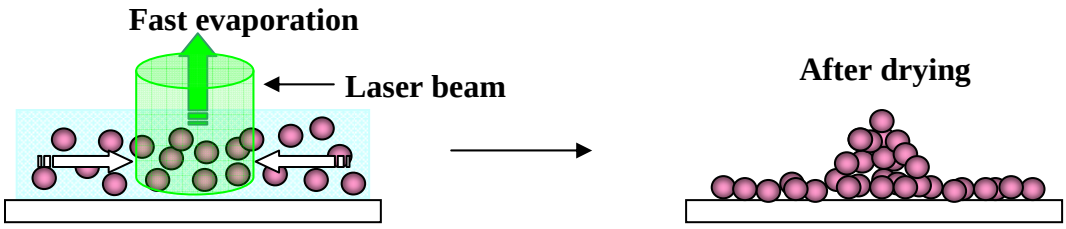

(b)

Figure 3.2 Experimental setup. (a) Schematic view of the laser induced structure formation during drying of polymer film. (b) Schematic view of a peak formation on the polymer film in the exposed area.

3.4 Results and Discussion

3.4.1 Effect of diameter of laser spot

Experiments were conducted in order to evaluate the effect of the diameter of laser spot on the structure formation of the dried polymer film and to determine the target value of the distance between the lense and the sample which would be used later in the other experiments. The dextran (40 and 70 kg/mole) was used in this experiment. The concentration of polymer solution was 0.1 g/g. The concentration of the dye solution was 0.01 g/g. The ratio between polymer solution and dye solution is 9/1 g/g. The wet film thickness was kept constant at h_i = 100 μm. (the thickness was calculated from the applied amount per area). Finally, the distance between lens and sample was varies from 2.5 – 15.0 cm. The laser intensity profiles versus displacement of razor-blade at different distances were plotted in order to calculate the diameter of laser spot, as shown in Fig. 3.3(a). The graph of the diameter of laser spot versus distance between lens and razor-blade was shown in Fig. 3.3(b).

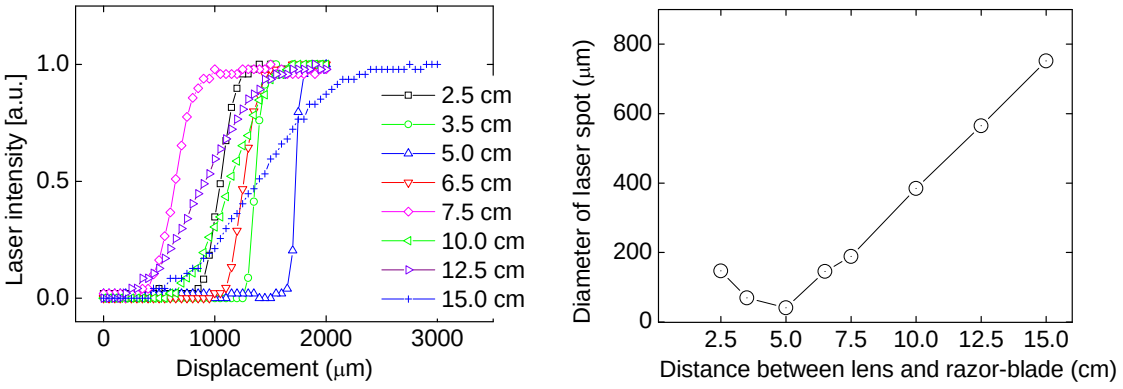

(a) (b)

Figure 3.3 The plot of laser intensity profile versus displacement of razor-blade at different distances (a). The graph of the diameter of laser beam as a function of distance between lens and razor-blade (b).

We found that the focus length of lens is 5.0 cm and the minimum diameter of laser spot is about 40 μm. From the focus length, increasing the distance leads to

increasing the diameter of laser spot and decreasing the distance leads to increasing the diameter of laser spot as well.

All the films were cast on glass substrate (2.0 x 2.0 cm). The profilometry line scan of the peak formation presented the effect of the diameter of laser spot is presented in Figure 3.4(a) and (b). The graph of the peak height as a function of the distance between lens and sample is presented in Figure 3.4(c).

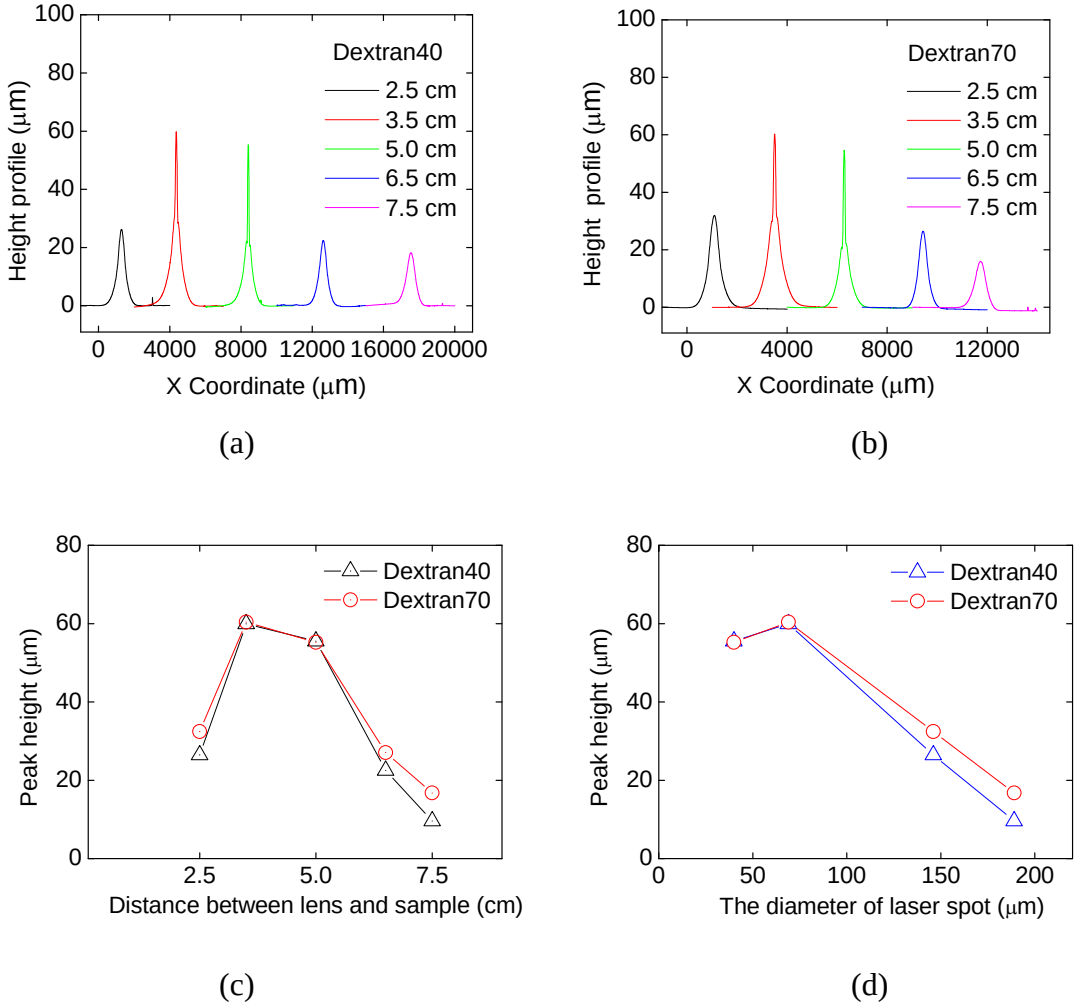

Figure 3.4 A profile of the peak formation of dextran sample (a) dextran40, (b) dextran70, (c) the graph of the peak height of dextran versus the distance between lens and sample and (d) the graph of the peak height of dextran versus the diameter of laser spot.

Figure 3.4(a) and (b) show the peak profile of dextran as a function of the distance between lens and sample. We found that the peak profiles at the distance 3.5 cm and 5.0 cm (focus point) showed the buckling instability at about half of peak height. The base width of all peaks is about 1 mm. When we used the diameter of laser spot more than 200 μm (the distance more than 7.5 cm), peak formation did not occur. This indicated that the base width of peak was not increased by increasing the diameter of laser spot. Figure 3.4(c) shows the graph of the peak height versus the distance between lens and sample. At the focus point (5.0 cm) has higher peak height than other distance except at the distance (3.5 cm). The peak heights at distance 2.5 cm and 6.5 cm are the same because the diameters of laser spot are the same. Comparison between two different molecular weights of dextran, no difference was found between two samples. Figure 3.4(d) showed the graph of the peak height of dextran versus the diameter of laser spot. We found that the peak height showed a decrease with increasing diameter of laser spot.

We want to prove that the evident of buckling instability of dextran might come from hydrogen bonding. To prove these hypotheses, polystyrene was selected for comparison because polystyrene did not form hydrogen bonding. The experiments were conduct in the same condition with dextran and the effect of molecular weight of polystyrene was investigated as well.

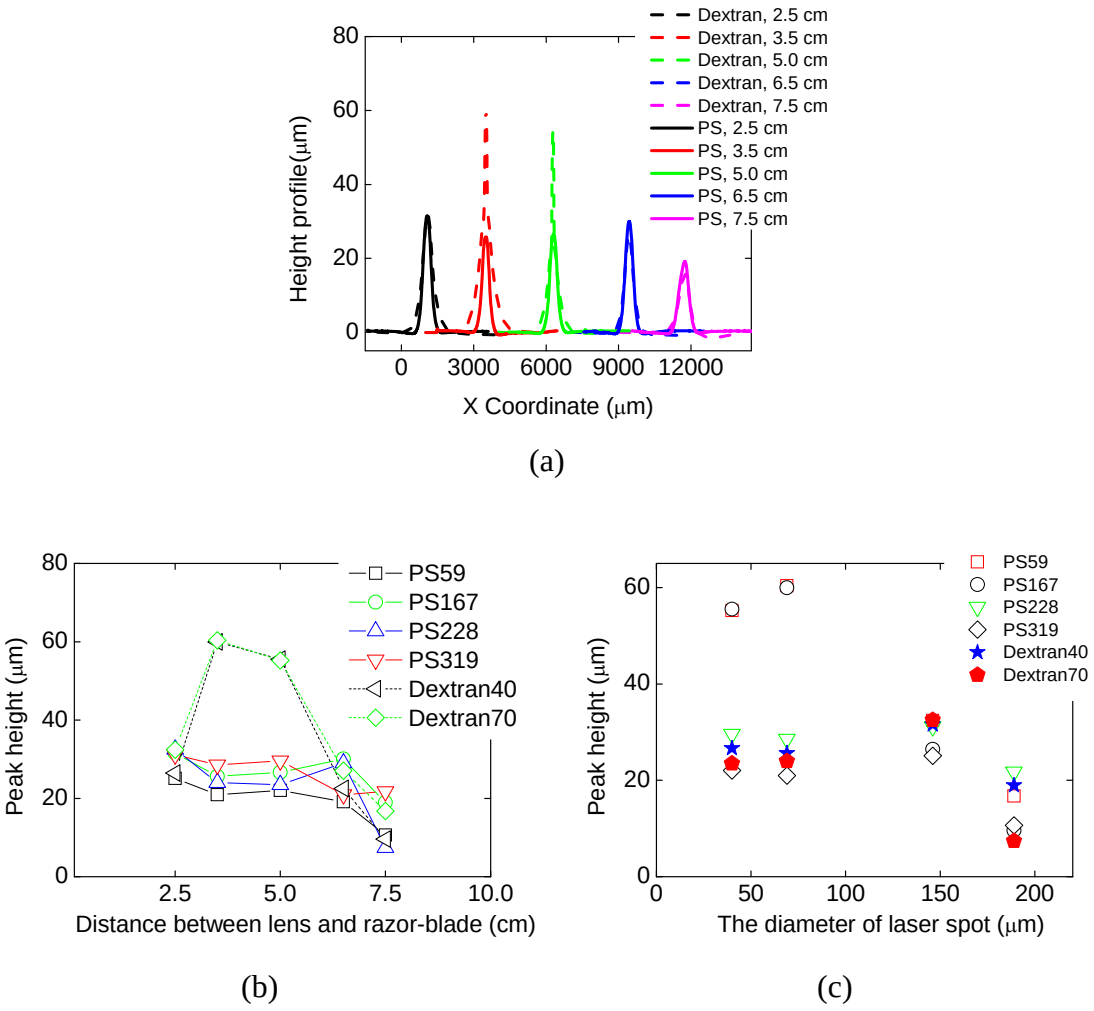

Figure 3.5 The comparision of the peak profile of polystyrene and dextran (a), the plot of peak height of dextran and polystyrene versus distance between lens and razor-blade (b) and the plot of peak height of dextran and polystyrene versus the diameter of laser spot (c).

Figure 3.5(a) shows the peak profile of polystyrene at different distance between lens and sample compared with peak profile of dextran. We did not see evidence of a buckling instability from peak profile of polystyrene. Fig. 3.5(b) showed the plot of peak height of dextran and polystyrene versus distance between lens and razor-blade. We found that maximum peak height of polystyrene occurred at position of buckling instability of dextran. This result indicated that buckling can aid the process of structure formation and hydrogen bonding might involves in this process. We also found that the

peak height of polystyrene slightly decrease when the diameter of laser spot increase, as shown in Fig. 3.5(c).

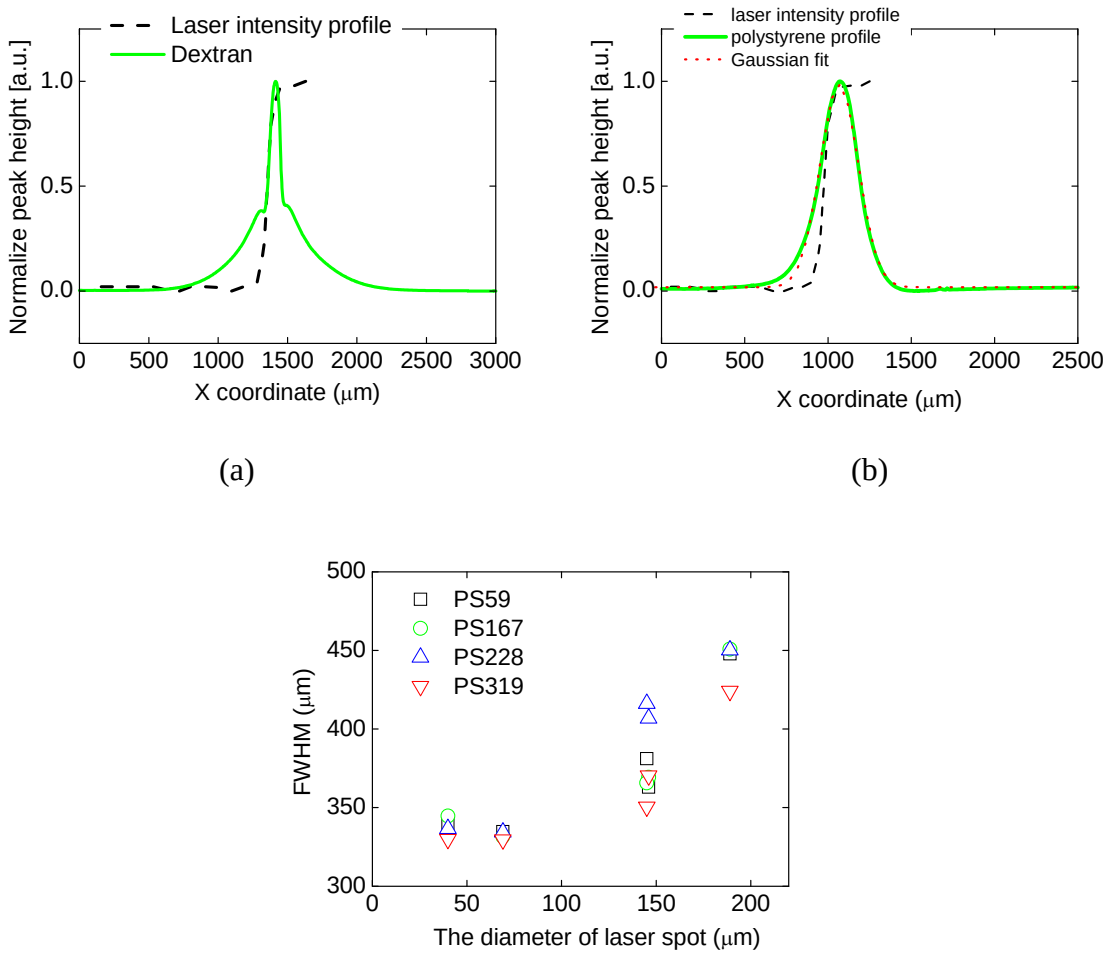

Figure 3.6 The evidentce of buckling instability of dextran, the width of buckling is about diameter of laser spot (a). The peak profile of polystyrene can fit well with Gaussian function (b). The plot of FWHM of polystyrene versus diameter of laser spot.

Figure 3.6(a) showed the evidence of buckling instability of dextran, the width of buckling is about diameter of laser spot. Figure 3.6(b) showed the peak profile of polystyrene which can fit well with Gaussian function, for this reason, we can calculate

the full width of haft maximum (FWHM) of peak as well. Figure 3.6(c) showed the plot of FWHM of polystyrene versus diameter of laser spot. We found that increasing of diameter of laser spot leads to increasing of FWHM. The FWHM is about 2-8 times of diameter of laser spot.

3.4.2. Effect of molecular weight of dextran

Experiments were conducted in order to evaluate the effect of molecular weight of dextran on the structure formation of the dried polymer film. Three molecular weights (40, 70 and 200 kg/mol) were used. The concentration of polymer solution is 0.1 g/g. The concentration of dye solution is 0.01 g/g. The ratio between polymer solution and dye solution is 9/1 g/g. The wet film thickness was varied from 50 to 250 μm. The distance between lens and sample was fixed at 5.0 cm. The irradiation time was about 60 min or until the film dried. The profilometry line scan of the peak formation presented the influence of molecular weight is presented in Fig. 3.7(a)-(c). Graph of the peak height as a function of the wet film thickness is presented in Fig. 3.7(d).

Considering about the peak profile, we found that all dextrans have buckling instability and the point which occurring buckling was about half of peak height as shown in Figure 3.7(a)-(c). Generally speaking, the peak height of all dextrans tends to increase when the wet film thickness increase as seen a good trend on dextran200. No difference was found for three samples.

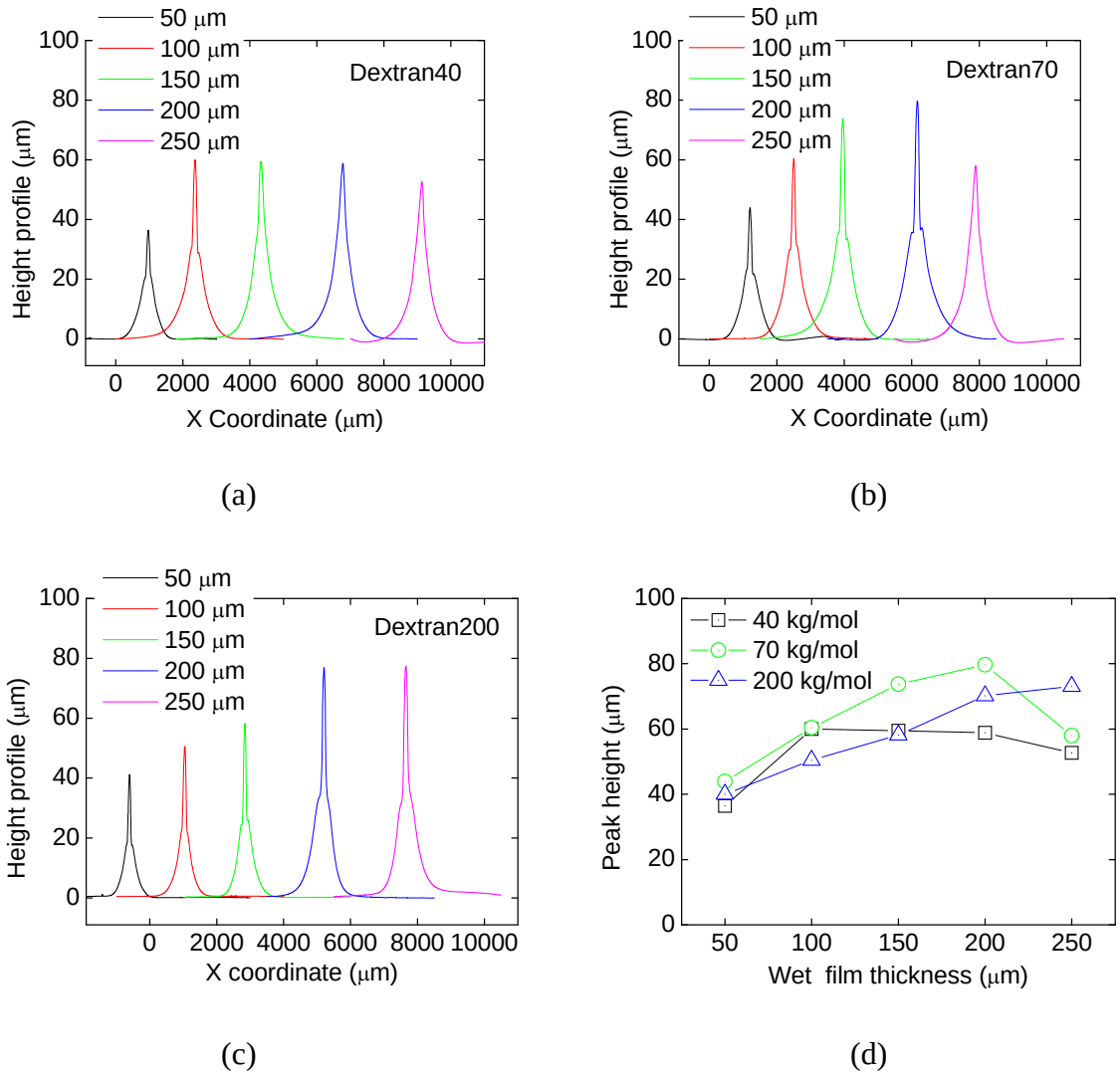

Figure 3.7 A profile of the peak formation of dextran with different wet film thickness (a) Dextran40, (b) Dextran70, (c) Dextran200 and (d) The graph of peak height as a function of the wet film thickness.

3.4.3 Effect of molecular weight of polystyrene

Experiments were conducted in order to evaluate the effect of molecular weight of polystyrene on the peak formation of the dried polymer film and to compare the influence of solvents on peak formation of polystyrene as well. Four molecular weights (59, 167, 228 and 319 kg/mol) were used. 1,4-dioxane was used to compare with toluene. The

concentration of polymer solution is 0.1 g/g. The concentration of dye solution (Oil Red EGN) dissolving in toluene is 0.8 mg/g. The ratio between polymer solution and dye solution is 1/1 g/g. The initial thickness of the film was varied from 100 to 250 μm. The distance between lens and sample was fixed at 5.0 cm. An example of the profilometry line scan of the peak formation presented the influence of molecular weight in toluene is presented in Figure 3.8(a)-(d). The graph of the peak height versus the wet film thickness in toluene and 1,4-dioxane is presented in Figure 3.8(e) and Figure 3.8(f), respectively. The graph of the FWHM versus the wet film thickness in toluene and 1,4-dioxane is presented in Figure 3.8(g) and Figure 3.8(h), respectively.

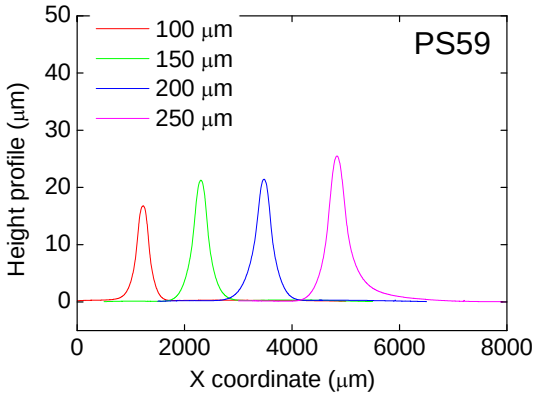

(a)

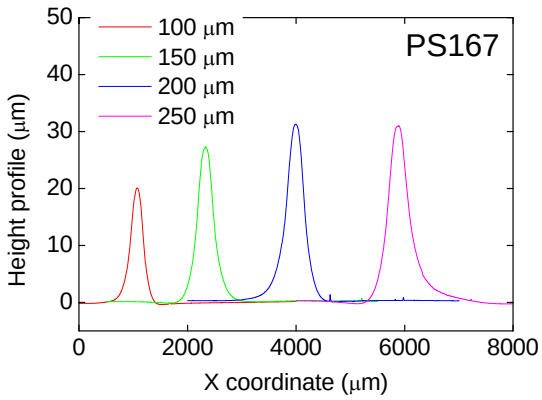

(b)

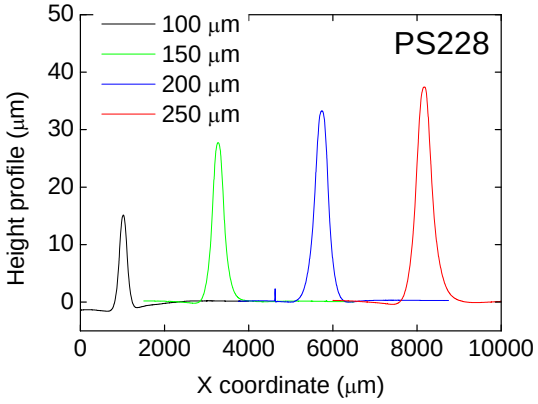

(c)

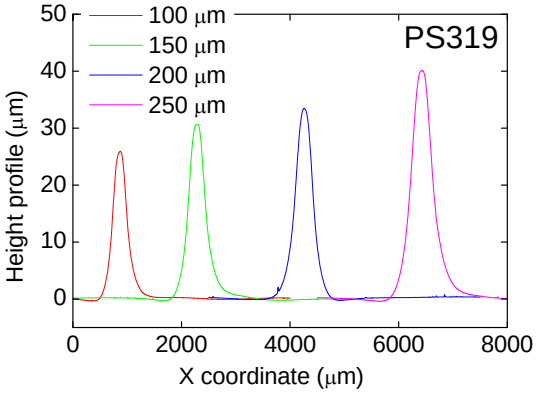

(d)

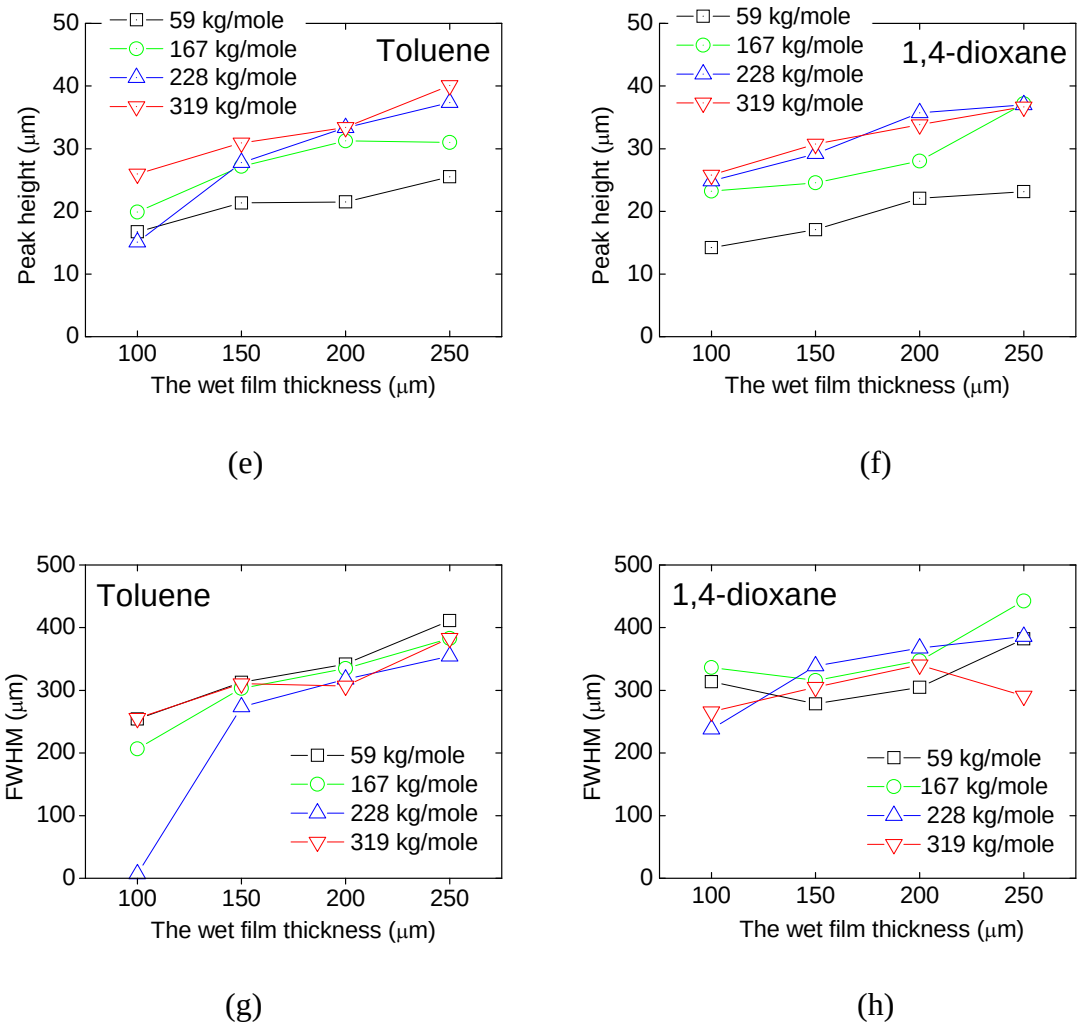

Figure 3.8 A profile of the peak formation of polystyrene with different the wet film thickness (a) 59 kg/mole, (b) 167 kg/mole, (c) 228 kg/mole and (d) 319 kg/mole. The graph of the peak height versus the wet film thickness of polystyrene (e) in toluene and (f) in 1,4-dioxane. The graph of FWHM calculated by fitting Gaussian equation versus the wet film thickness (g) in toluene and (h) in 1,4-dioxane.

Figure 3.8(a)-(d) showed the peak profile of four molecular weights of polystyrene. We found that the peak profiles of polystyrene did not showed the buckling instability and peak profiles were fitted well with Gaussian equation. The reason why the peak profiles of polystyrene did not showed the buckling instability is that polystyrene can not form hydrogen bonding. Figure 5(e) and (f) showed the graph of the peak height versus the wet film thickness of polystyrene in toluene and in 1,4-dioxane, respectively. No difference was found between toluene and in 1,4-dioxane. We found that properties of solvent used such as viscosity, boiling point, density, dipole moment, solubility parameter and surface tension did not effect on the peak formation. The physical properties of the pure solvents are listed in table 1.

Table 1 The physical properties of organic solvents[13]

Property	Toluene	1,4-dioxane
Boiling point (^{0}C)	110.6	88.1
Density (g/cm^3)	0.820	1.023
Dipole moment (Debye)	0.36	-
Solubility parameter (MPa)$^{1/2}$	20.1	18.3
Surface tension (mN/m)	27.4	32.2
Viscosity (cp)	0.52	1.10

In contrast to the study of Jarusuwannapoom, T. et al[13], they found that dipole moment and conductivity of solvent effect on the morphology of product fibbers producing by electro-spinning. The peak height showed an increase with the wet film thickness. Considering about molecular weight, we found that higher molecular weight leads to higher peak height.

Figure 3.8(g)-(h) showed the graph of the full width of half maximum (FWHM) calculated by fitting Gaussian equation versus the wet film thickness of polystyrene in toluene and in 1,4-dioxane, respectively. We found that the FWHM showed an increases with the wet film thickness. The minimum of the full width of half maximum is about 200 μm which is about 5 times of the diameter of laser spot (40 μm). This indicated that the FWHM is always higher than the diameter of laser spot by factor of 2-5.

3.4.4 Effect of dye contents

Experiments were conducted in order to evaluate the effect of dye content on the peak height of the dried polymer film. And another objective of this experiment is to compare the peak formation between two polymers as well. Dextran (200 kg/mole) and polystyrene (228 kg/mole) were used. The solvent for dextran is water while the solvent for polystyrene is toluene. The concentration of polymers solution is 0.1 g/g. Dye for dextran is congo red while dye for polystyrene is oil red EGN. The concentration of dye solution is 0.01 g/g. The ratio between polymer solution and dye solution was 9/1, 8/2, 7/3, 6/4 and 5/5 g/g. The wet film thickness was varied from 100 to 250 μm. The distance between lens and sample was fixed at 5.0 cm. The graph of the peak height as a function of the wet film thickness is presented in Figure 3.9.

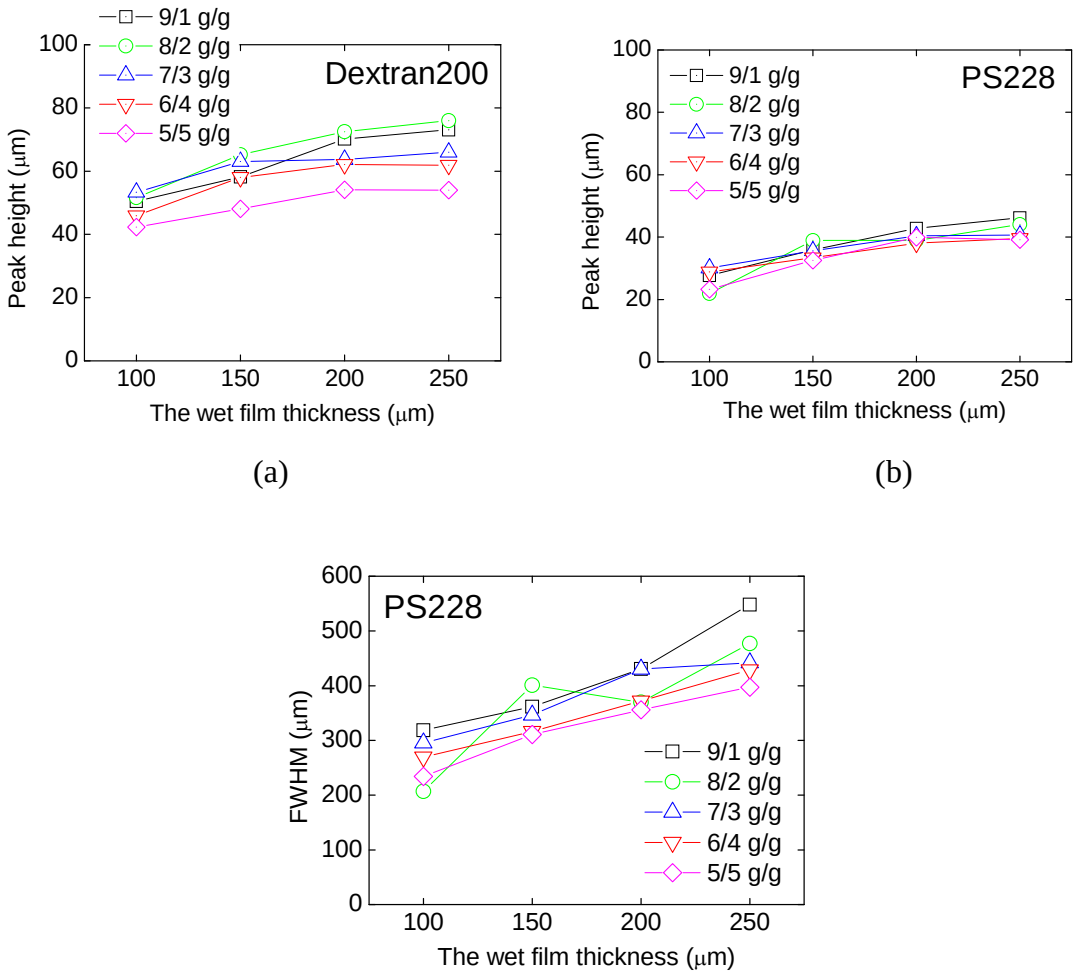

Figure 3.9 The graph of the peak height versus the wet film thickness (a) dextran (200 kg/mole) and (b) polystyrene (228 kg/mole). (c) The graph of FWHM calculated by fitting Gaussian equation versus the wet film thickness of polystyrene (228 kg/mole).

Figure 3.9(a) showed the graph of the peak height versus the wet film thickness at the five different dye contents of dextran200. We found that the peak height did not show an increase with dye content. From our experimental results, the minimum peak height of dextran is about 40 μm while the maximum peak height of polystyrene is about 40 μm, as shown in Fig. 3.9(b). We found that the peak height of dextran is higher than polystyrene for all condition. Considering the peak profile of dextran, we found that peak profile of dextran showed the evidence of bucking instability. The possibly explanation

is that dextran can form hydrogen bonding. The buckling instability plays rule to increase the peak height. Surprisingly, the position occurred buckling instability is about half of peak height of dextran. Figure 3.9(c) shows the graph of FWHM calculated by fitting Gaussian equation versus the wet film thickness of polystyrene (228 kg/mole). We found that the FWHM slightly change with dye contents.

3.4.5 Effect of polymer concentration

Experiments were conducted in order to evaluate the effect of polymer concentration on the peak height of the dried polymer film. Dextran (200 kg/mole) and polystyrene (228 kg/mole) were used. The solvent for dextran is water while the solvent of polystyrene is toluene. Dye for dextran is congo red while dye for polystyrene is oil red EGN. The concentration of dye solution is 0.01 g/g. The concentration of polymer solution was varied 0.05, 0.1 and 0.2 g/g. The ratio between polymer solution and dye solution was 9/1, 8/2 and 7/3 g/g. The wet film thickness was varied from 100 to 250 μm. The graph of the peak height versus the wet film thickness is presented in Figure 3.10.

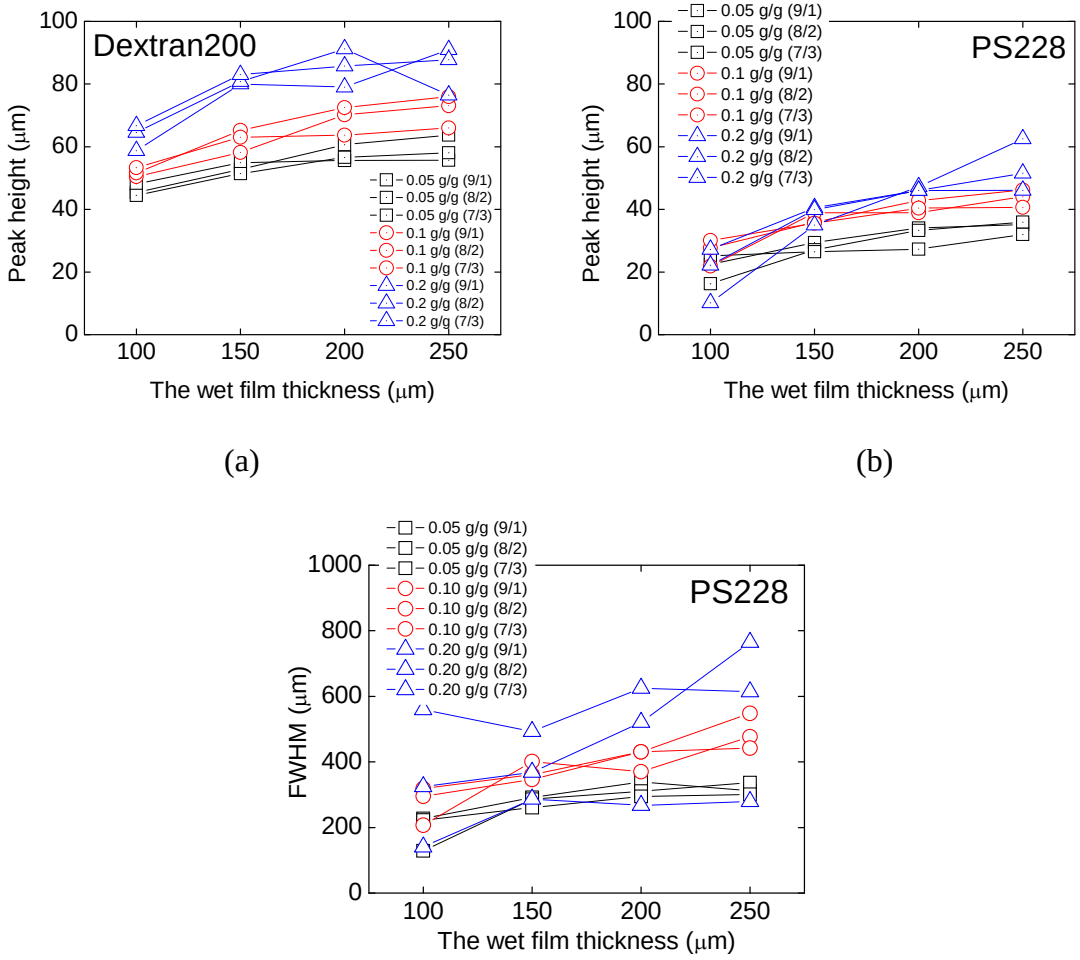

(a) (b)

(c)

Figure 3.10 Comparison of the peak height at different polymer concentration between dextran and polystyrene (a) dextran (200 kg/mole) and (b) polystyrene (228 kg/mole). (c) The graph of FWHM calculated by fitting Gaussian equation versus the wet film thickness of polystyrene (228 kg/mole).

Figure 3.10(a) showed the graph of the peak height versus the wet film thickness for three polymer concentration of dextran with varies dye contents as well. We found that peak height showed an increase with polymer concentration. Figure 3.10(b) showed the graph of the peak height versus the wet film thickness for three polymer concentration of polystyrene with varies dye contents as well. We found that increasing polymer concentration leads to higher peak height. Figure 3.10(c) showed the graph of FWHM

calculated by fitting Gaussian equation versus the wet film thickness of polystyrene (228 kg/mole). We found that the minimum FWHM is about 200 μm (about 5 times of the diameter of laser spot). The FWHM showed an increase with polymer concentration.

3.5 Conclusions

In summary the light-induced structure formation during drying of polymer film was investigated. The maximum diameter of laser spot for inducing structure formation is about 200 μm. There is a characteristic difference of structure formation between dextran and polystyrene polymers. Peak profile of dextran showed the evidence of buckling instability because of hydrogen bonding formation during drying polymer films while polystyrene did not showed this evidence. The peak height of dextran is higher than the polystyrene. The FWHM of polystyrene is larger than the diameter of laser spot about 2-8 times. No difference was found for different molecular weight of dextran and polystyrene. Increasing polymer concentration leads to increasing the peak height. The peak height did not increase when the dye content increases.

3.6 References

1. Deegan, R. D.; Bakajin, O.; Dupont, T. F.; Huber, G.; Nagel, S. R.; Witten, T. A., Capillary flow as the cause of ring stains from dried liquid drops. *Nature* **1997,** 389, (6653), 827-829.

2. Harris, D. J.; Hu, H.; Conrad, J. C.; Lewis, J. A., Patterning Colloidal Films via Evaporative Lithography. *Physical Review Letters* **2007,** 98, (14), 148301.

3. Harris, D. J.; Conrad, J. C.; Lewis, J. A., Evaporative lithographic patterning of binary colloidal films. *Phil. Trans. R. Soc. A* **2009,** 367, (1909), 5157-5165.

4. Pauchard, L.; Allain, C., Buckling instability induced by polymer solution drying. *Europhysics Letters* **2003,** 62, (6), 897-903.

5. Georgiadis, A.; Routh, A. F.; Murray, M. W.; Keddie, J. L., Bespoke periodic topography in hard polymer films by infrared radiation-assisted evaporative lithography. *Soft Matter* **2011,** 7, (23), 11098-11102.

6. Zhuang, S. Y. C. a. L., Lithographically induced self-assembly of periodic polymer micropillar arrays *J. Vac. Sci. Technol. B* **1999,** 17, (6), 3197.

7. Stephen Y. Chou, L. Z., and Linjie Guo Lithographically induced self-construction of polymer microstructures for resistless patterning *Appl. Phys. Lett.* **1999,** 75, (7), 1004.

8. Paru Deshpande, X. S., and Stephen Y. Chou Observation of dynamic behavior of lithographically induced self-assembly of supramolecular periodic pillar arrays in a homopolymer film *Appl. Phys. Lett.* **2001,** 79, (11), 1688.

9. Schäffer, E. T.-A., T; Russell, TP and Steiner, U, Electrically induced structure formation and pattern transfer. *Nature* **2000,** 403, 874.

10. Peng, J.; Han, Y.; Yang, Y.; Li, B., Pattern formation in polymer films under the mask. *Polymer* **2003,** 44, (8), 2379-2384.

11. Peng, J.; Wang, H.; Li, B.; Han, Y., Pattern formation in a confined polymer film induced by a temperature gradient. *Polymer* **2004,** 45, (23), 8013-8017.

12. Keddie, J. L.; Routh, A. F., Fundamentals of Latex Film Formation: Processes and Properties. *Springer* **2010**.

13. Jarusuwannapoom, T.; Hongroijanawiwat, W.; Jitjaicham, S.; Wannatong, L.; Nithitanakul, M.; Pattamaprom, C.; Koombhongse, P.; Rangkupan, R.; Supaphol, P., Effect of solvents on electro-spinnability of polystyrene solutions and morphological appearance of resulting electrospun polystyrene fibers. *European Polymer Journal* **2005,** 41, (3), 409-421.

Chapter 4

Method of Making a Patterned Dried Polymer

Method of Making a Patterned Dried Polymer

*Chakkresit Chindawong and Diethelm Johannsmann**

Institute of Physical Chemistry, Clausthal University of Technology
39678 Clausthal-Zellerfeld, Germany

4.1 Abstract

A method of making a patterned dried polymer from a polymer solution is described. The method comprises a first step of printing black lines onto the back of polyester sheet so that there are printed areas and unprinted areas. When drying a polymer solution deposited onto the back side of this kind of substrate under IR-lamp, the black lines absorbed heat. The films after drying show elevations at the positions above the black lines. We show that the amplitude of the surface features depend on several key parameters such as the initial thickness of the film, the molecular weight of polymers, and the pitch of the pattern.

4.2 Introduction

There are needs for textured coating for many reasons. One might inspire from nature. As we known previously, superhydrophobic surfaces of the lotus leaf,[1] antireflection surfaces of the moth's eye[2] and anti-fouling surfaces of marine organism[3-6] all are the result of the topography or texture of a surface at the micrometre and nanometre length scales. Dome-like surface structures function as microlenses.[7] Straining molded and wrinkled surfaces have been used to tune the adhesion of silicone adhesives.[8] In optical applications, surface features have been employed to tune the surface optical band gap,[9] to increase the light extraction efficiency of diodes,[10] and to act as diffraction gratings.[11]

There are several techniques[12-15] for creating polymer coatings with topographical structure controlled at length scales of nm or mm. A well established method is photolithography, but it is a multistep process requiring specially-designed equipment and photosensitive materials. Topographical features, especially ridges, have also been created by wrinkling processes. Wrinkling has been induced by a mismatch of the elastic moduli of surface layers and substrates achieved by the oxidation of silicone,[16] by differences of the thermal expansivity between polymers and metals,[17] and by the swelling of polymers by solvents.[18] This type of coating necessarily requires a multilayered structure, surface treatments, or a flexible substrate, and hence is not widely applicable.

There are several methods to create topographical patterns in solvent-cast polymer films. For instance, ordered arrays of air bubbles (created when solvent droplets evaporate[19]) have been used to create topographical structures. Elsewhere, less well-ordered topographies have been created from Marangoni instabilities during solvent evaporation from polymer solutions[20] and by surface tension-driven convection.[21] Surface structures can be created in polymers through various types of moulding, such as injection molding,[22] hot embossing[23, 24] and ultraviolet nanoimprinting.[25] These techniques have several disadvantages, such as a lack of process flexibility and a need for expensive equipment.

Routh and Russel[26] introduced a new direction for patterning of polymeric surfaces. They showed that the modulation of evaporation rate across the surface of a

wet colloidal film can drive lateral flow. They placed a mask with holes in it above a latex dispersion. The colloidal polymer particles were carried in the flow towards regions under the holes where water was evaporating fastest. The result was a latex film in which the film was thicker under the pattern of holes in the mask. Building on this work, Harris et al.[27] investigated a novel assembly route for patterning colloidal films, known as evaporative lithography, which uses holes in masks to modulate evaporation, thereby creating patterns of particles. Water evaporation is faster under the open regions in the mask. A lateral water flux is thus set up to replace the water lost to evaporation. This flux carries particles to the open regions. This team reported a fundamental study of the factors affecting pattern formation from hard particles[27] (polystyrene and silica) and from blends of mm-sized and nm-sized particles.[28] Parneix et al. proposed a new type of evaporative lithography used for creating dips and rim patterns in very thin colloidal films.[15] More recently, Keddie et al.[14] announced a new type of evaporative lithography called infrared radiation-assisted evaporative lithography, which used holes in mask and infrared radiation to create periodic topographic patterns hard polymer films[14, 29, 30]

Evaporative lithography presents two limitations. Firstly, Harris et al.[27] reported that two hours were required to make nanoparticle patterns. Secondly, particles of glassy (hard) polymers, which have a glass transition temperature, T_g, greater than room temperature, are not capable of film formation but instead yield brittle and cracked coatings.[31] Keddie et al[32] also demonstrated that infrared radiation-assisted sintering (IRAS) can overcome the limitation of standard lithography and can be an effective means of processing hard latex films. Heating of polymer particles was achieved by the absorption of infrared radiation, which enabled particle coalescence and film formation in a glassy (i.e. ‘‘hard’’) polymer.

Here, we have merged the techniques of evaporative lithography and infrared assisted evaporation to create patterned coatings from a polymer solution. Infrared radiation is shone through a wet polymer film deposited on polyester sheet which was printed black lines onto the back side. When drying a polymer solution deposited onto this kind of substrate under IR-lamp, the black lines absorbed heat. The films after drying showed elevations at the positions of black lines. Because of the resulting elevated temperatures, drying is faster than in standard evaporative lithography. Polymer

flow with the solvent and accumulate above the black lines on the substrate. Importantly, the localised heating above the black line regions of the substrate creates an advantageously strong evaporative flux. Moreover, the infrared heating induces particle sintering and leads to crack-free, films with a bespoke topography. We showed that infrared-assisted evaporation without mask can create a polymer coating with bespoke topography with a pitch, P, able to range from hundreds of mm to a few mm.

4.3 Materials and Experimental

4.3.1 Materials

Four different molecular weights of polystyrene (59, 167, 228 and 319 kg/mol) were used in this experiment. The glass transition temperature of polystyrene is about 106 ^{0}C.[33] Toluene (Aldrich) was used as solvent. Oil red EGN (Aldrich, USA) (λ_{max} = 521 nm, molar extinction coefficient is about 26,000 $(mol/L)^{-1}cm^{-1}$ and melting point is 130 ^{0}C) was used as dye. These materials were used as received with out further purification.

Substrate used in this experiment is polyester sheet (3M CG3700Transparency film for Hewlett-Packard Colour Laser Jet Printer, thickness 0.127 mm).

For sintering of the polymer film a 100 W IR lamp (model type IR10: Philips Infrared R95E, Petra electric) has been used. The lamp's peak emission is in the NIR range between 780-1400 nm.

4.3.2 Profilometer

The profilometer (TENCOR P-1 long scan profiler) was used to measure the profile structure.

4.3.3 Data analysis

The OriginPro Version8.5 was used to analysis the profile surface. The profile surfaces were fitted by using a Fast Fourier Transform (FFT) to get the amplitude of wave-like surface.

4.3.4 Experimental set up

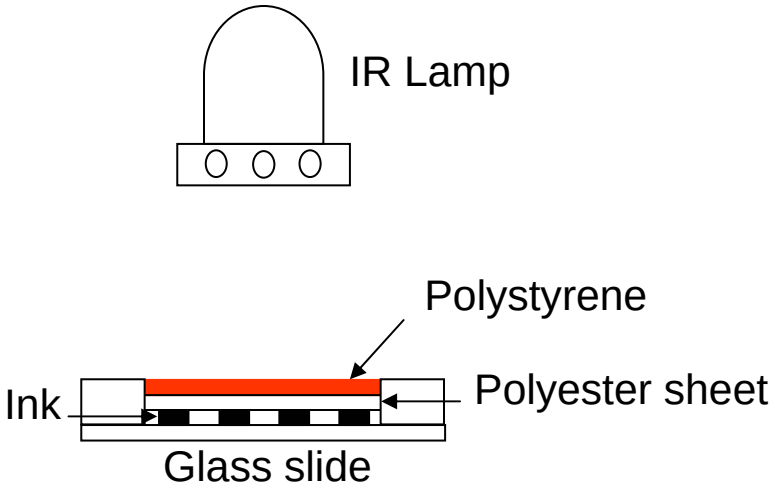

Figure 4.1 Experimental setting for large scale patterning of polymer films

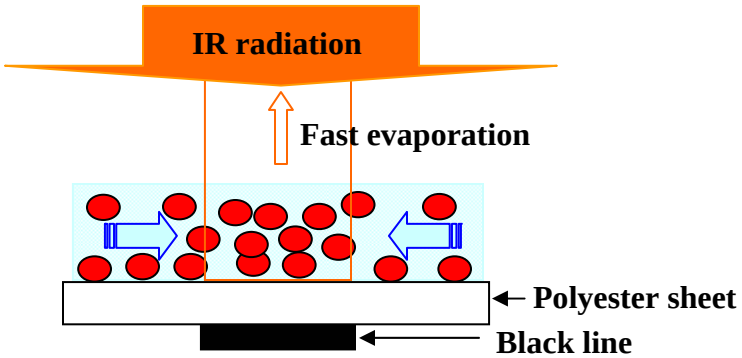

(a)

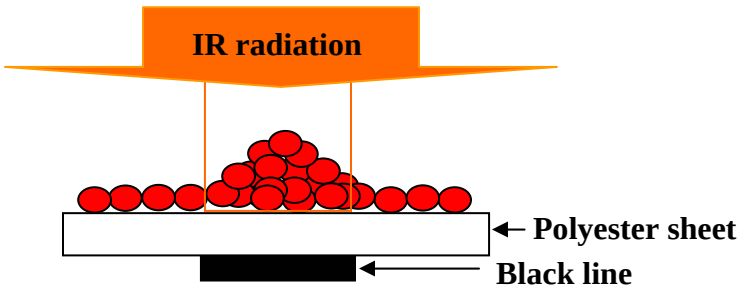

(b)

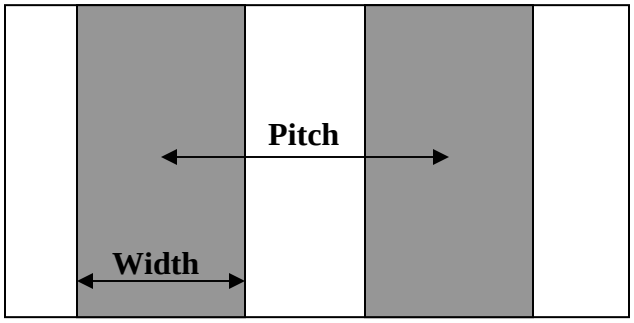

(c)

Figure 4.2 Schematic view of a raised feature on the patterned film during drying of polymer films (a) showed the mechanism of fluid flow to the area of black line during drying and (b) showed the elevations at the position of the black lines after drying. (c) schematic view of the master.

4.3.5 Sample preparation

The wet film samples were cast on polyester sheet (2.0 cm x 2.0 cm) which was printed black lines on the back side. The parameters, initial wet thickness, molecular weights of polymer and dye contents were varied. The wet film was exposed directly to the NIR radiation from the lamp. The IR lamp is placed in most of the experiments at a distance of 16.5 cm above the sample. The radiation time under the IR lamp is in the range from 15 min to 50 min. depending on the initial thickness of the film (a longer radiation is required for thicker films). Later, when the polymer film is dried, the sample is removed from the apparatus and is studied by using a profilometer.

4.4 Results and Discussion

4.4.1 Effect of dye

To evaluate effect of dye, 0.1 g/g of the polystyrene in toluene was prepared. The 0.08 wt% of Oil red EGN was also prepared. The polystyrene (pure and with Oil Red EN, 0.1 g/g of the polystyrene: 0.08 wt% of Oil red EGN is 1 g: 1g) were cast on polyester sheet (2.0 cm x 2.0 cm) which was printed back lines on the back side with varied initial wet thickness and then the samples were placed 16.5 cm beneath the IR

lamp until dry. Finally, the samples have been studied with profilomer and ImageJ. In this experiment, the width of back line is 0.353 mm and the pitch is 1 mm.

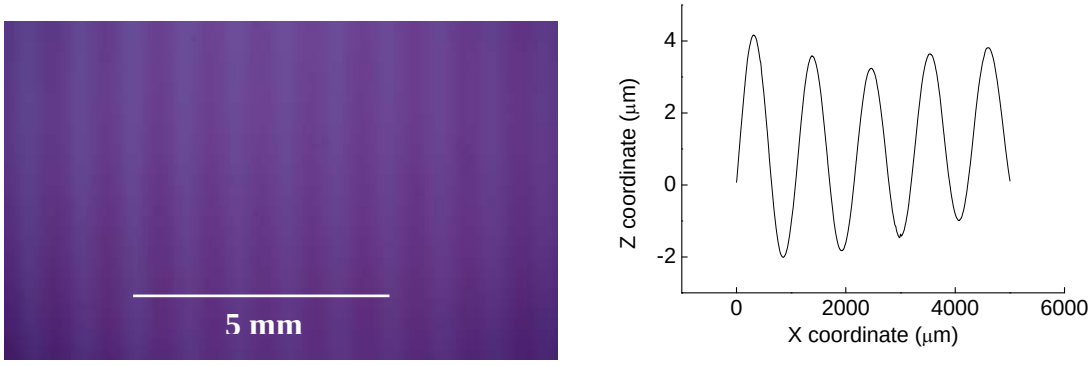

(a) (b)

Figure 4.3 (a) Photograph of the patterned polymer film and (b) Profilometer profile of a patterned film.

After the casting of the polymer onto the polyester sheet, which was printed black lines onto the back side, the film is irradiated by the IR lamp, as shown in Fig. 4.1. The use of the black line ink results in the selective exposure of the wet film to infrared radiation. The wet film above the lined areas reach higher temperatures, due to the black lines absorbed heat, than the unlined areas. Consequently, the evaporative flux is higher in the lined areas. In addition, in these areas the evaporation is also enhanced by the black lines. The solvent flows inward to regions of higher evaporation to replace the fluid loss, as the film surface remains flat, due to the surface tension. Furthermore, this flow also carries particles and hence this results in the accumulation of particles above the line regions, and hence the pattern formation, as shown in Fig. 4.2(b).

An example of a patterned polymer film is shown in Fig. 4.3(a). A master with line width, B = 0.353 nm and pitch, P = 1 mm was used. From profilometer profile, we found that the full width at half maximum (FWHM) of the raised features for this film is approximately 530 μm which are larger than the width of master about factor of 2 and the peak-to-valley height is approximately 3 μm.

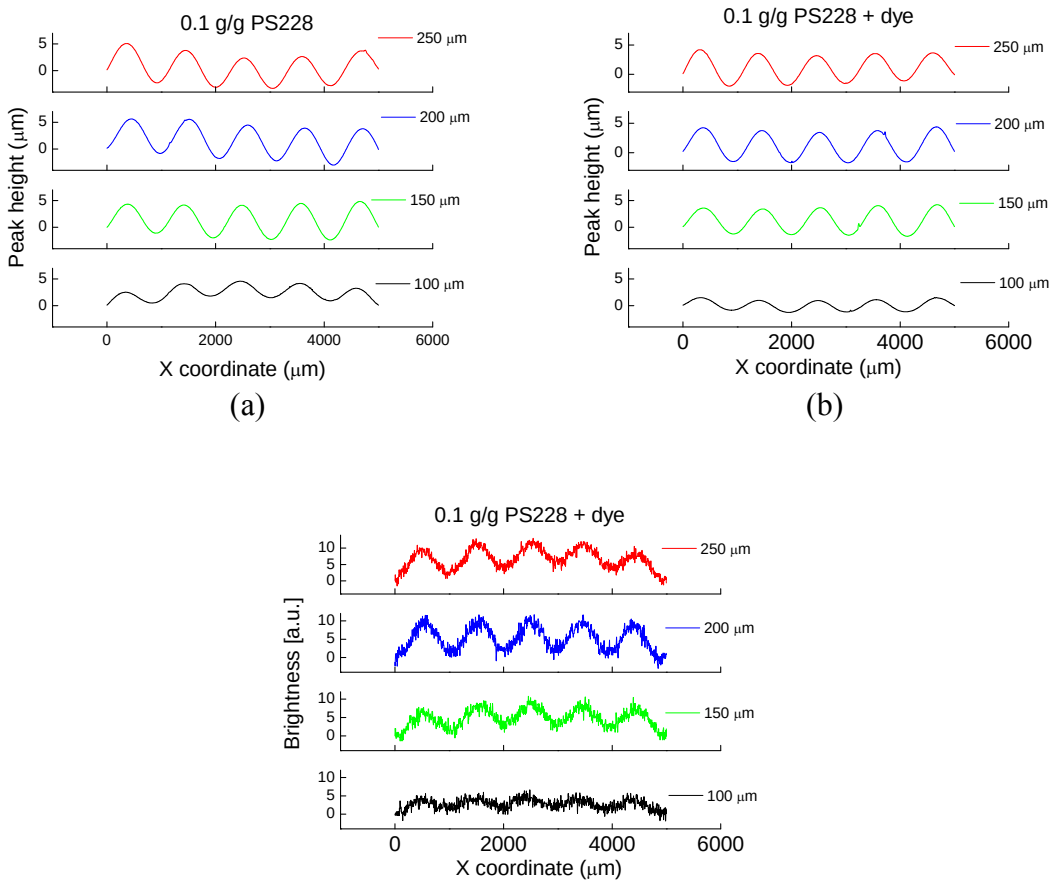

Figure 4.4 (a) The profilometer profile of the patterned polymer film without dye. (b) The profilometer profile of the patterned polymer film with dye. (c) The profile of the color contrast of the patterned polymer film with dye created by using ImageJ program.

The mechanism relies on the fact that the evaporation rate of solvent will be different at position above the black line areas and without the black line areas of polymer solution. The evaporation rate will be higher at position above the black line areas, and so the polymer concentration in these areas will become higher than at the position without black line areas. There will be a flux of fluid from the unlined areas to the lined areas to replace the lost solvent. This flux will carry polymer particles/molecules with it, and so the polymers above the lined areas will become raised relative to the polymers above the unlined areas. These raised portions will form a pattern on the surface of the resulting dried polymer. In this experiment, we also added

dye to see the contrast of the topography surface. We found that the dye accumulated in the areas above the black line areas of dried polymer films. The ImageJ program can be used to create the contrast profile of patterned polymer films, as shown in Fig. 4.4(c). We found that adding the dye to polymer solution did not effect on the aspect ratio of the raised feature of patterned polymer films, as shown in Fig. 4.5 and 4.6. Fig. 4.3(a) demonstrated that at position above the black line areas the dye concentration higher than at position above without black line areas.

From Fig. 4.5, we found that the aspect ratio of patterned surface without dye content did not change with the wet thickness and molecular weight of polystyrene. The value of aspect ratio of patterned surface is about 0.004. Considering in Fig. 4.6, the value of aspect ratio of patterned surface with dye content increases when the wet film thickness increases. As shown a good trend in PS59, the maximum value of the aspect ratio is 0.009.

We also calculated the amplitude of surface profile of patterned polymer surface by using FFT method. Fig. 4.7 and 4.8 showed the plot of the amplitude versus the wet film thickness of four different molecular weights of polystyrene without dye and with dye, respectively. We found that the amplitude increases when the wet film thickness increases.

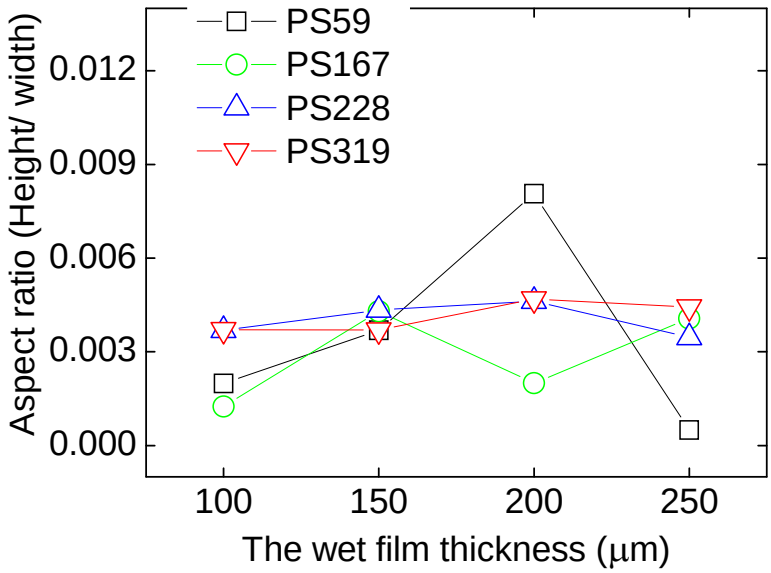

Figure 4.5 The plot of the aspect ratio versus the wet film thickness of four different molecular weights of polystyrene without dye contents.

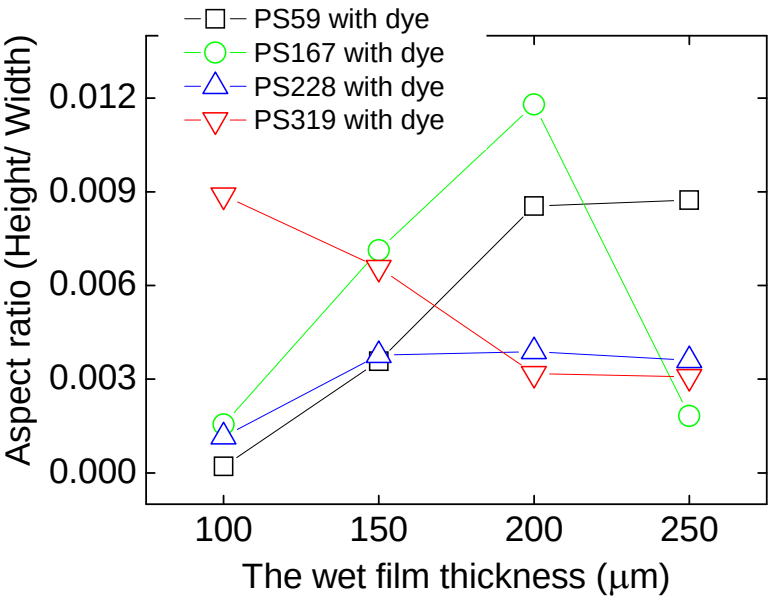

Figure 4.6 The plot of the aspect ratio versus the wet film thickness of four different molecular weights of polystyrene with dye contents.

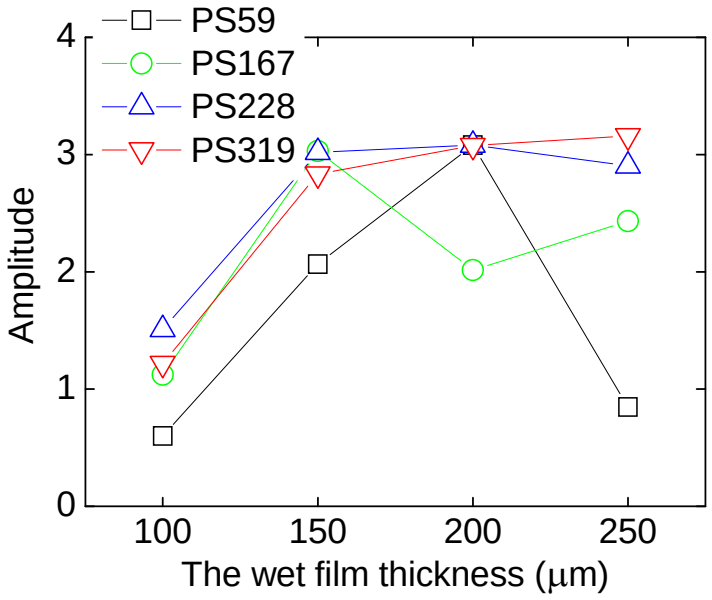

Figure 4.7 The plot of the amplitude of surface profile versus the wet film thickness of four different molecular weights of polystyrene without dye contents.

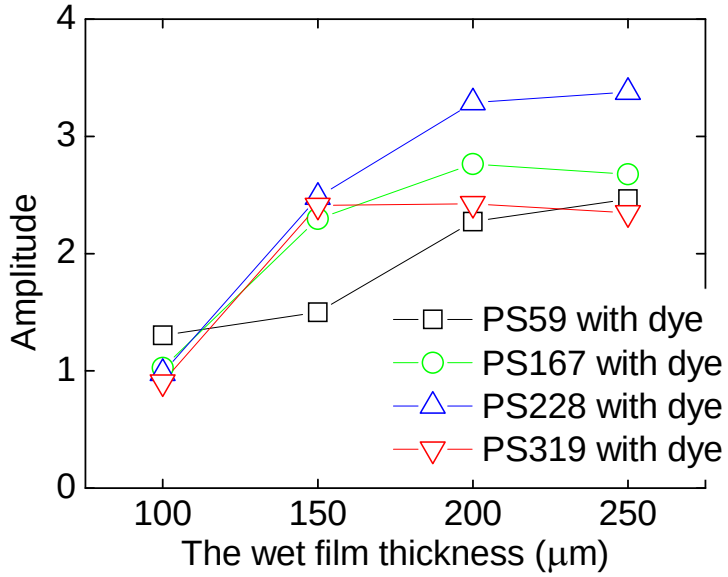

Figure 4.8 The plot of the amplitude of surface profile versus the wet film thickness of four different molecular weights of polystyrene with dye contents.

4.4.2 Effect of the line width and the pitch size

In order to determine the effect of line width and the pitch size on the amplitude of the raised features of the dried film, a series of polyester masters sheets have been used. The pitch size, P, were 0.30 mm, 0.50 mm, 0.70 mm and 0.90 mm. In this series, the line width was fixed at $P/2$. The initial wet thickness was kept constant at 100 μm. The concentration of polymer also kept constant at 0.1 g/g. All the films were cast on a polyester master sheet (2.0 cm x 2.0 cm). The example profiles of the dried patterned polymer films from different pitch size were shown in Fig. 4.9. The plot of the amplitude as a function of P is presented in Fig. 4.10.

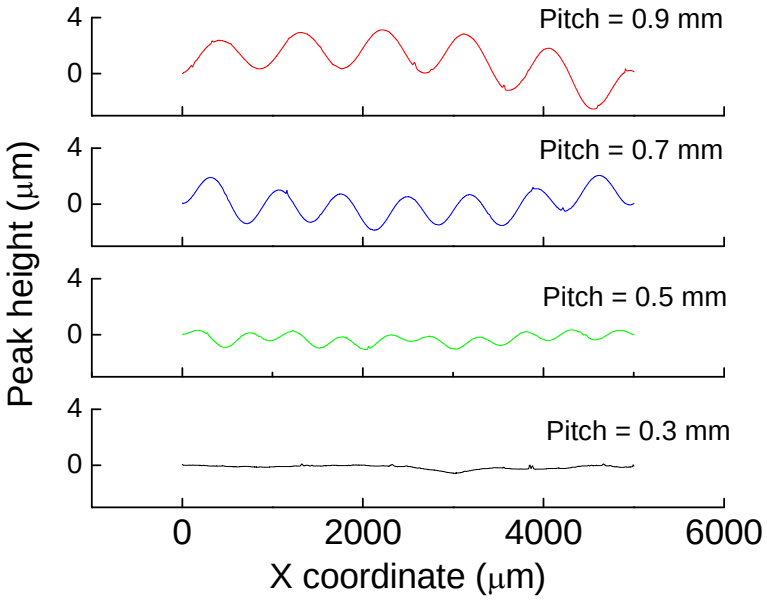

Figure 4.9 The profilometer profile of the patterned polymer film without dye at four different pitch sizes.

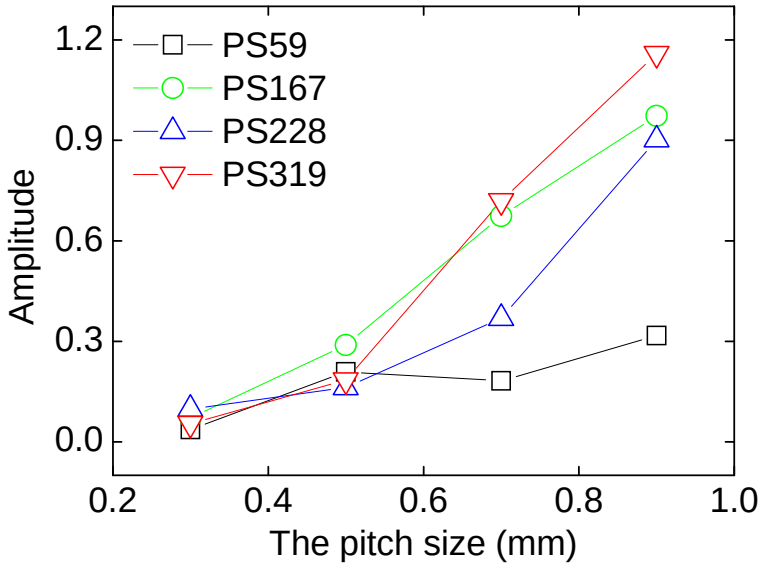

Figure 4.10 The plot of the amplitude as a function of the pitch size, P .

As shown in Fig. 4.9, no raised feature appears on polymer surface when the pitch size is narrow. This means that this method can not used to make the patterned surfaces which have the pitch size narrower than 0.3 mm. The possible explanation is that the difference of the evaporation rate between the black line area and without black line area are not enough for texture formation before drying is complete. The pitch size has a good correlation with amplitude, as shown in Fig. 4.10. This indicates that increasing the pitch size leads to increasing of the amplitude of surface profile.

4.4.3 Effect of the wet film thickness

Experiments were conducted in order to show the effect of the wet film thickness on the amplitude of the raised features of the dried film. The polyester sheet which was printed the black line width = 0.353 mm, pitch = 1 mm on the back side was used in these experiments. The polymer concentration was kept constant at 0.1 g/g. Finally, the wet film thickness varied in the rang from 100 µm to 250 µm. All the films were cast on a polyester sheet master substrate (2 cm x 2 cm). The amplitude as a function of the wet film thickness is presented in Fig. 4.11.

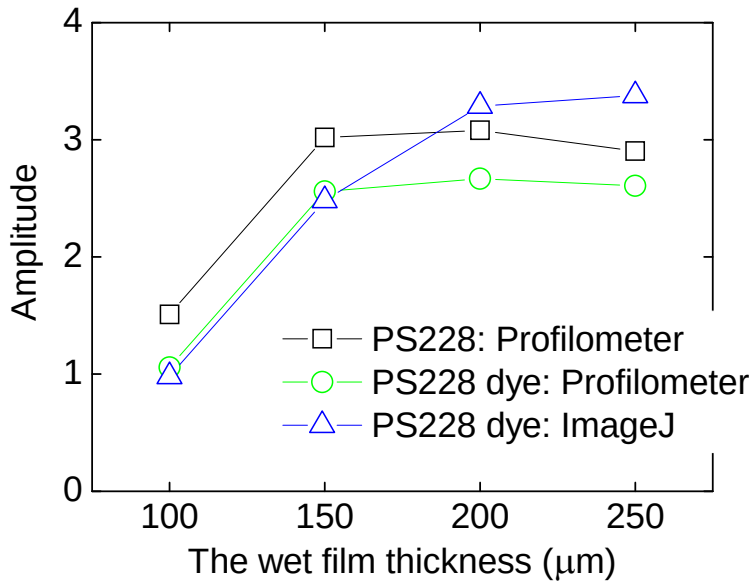

Figure 4.11 The plot of the amplitude of profile surface versus the wet film thickness

As shown in Fig. 4.11, a thicker film leads to the amplitude heights. No different of the amplitude of surface profile was found between pure polymer solution and polymer solution with dye. The value of amplitude of surface profiles characterized by profilmeter and imageJ showed the same value.

4.4.4 Effect of molecular weight

In order to evaluate the effect of molecular weight of polymer on the amplitude of profile surface, the four different molecular weight of polystyrene were prepared in the same concentration (0.1 g/g). The concentration of dye solution is 0.08 wt%. The pure polymer solution and polymer solution mixed with dye solution in volume ration 1/1 were used in this experiment. As shown in Fig. 4.7 and 4.8, four different molecular weight polymers showed the same amplitude. This means that molecular weight of polymers did not effect on the amplitude of surface profile.

4.5 Conclusion

In summary, we showed how the black ink can be used to pattern thin polymer films. This method is versatile since the black ink can be printed easily, and even possibly removed, thus allowing creation of the raised features are quite the same diameter. It constitutes a simple way to structure the surface of a film of micrometric thickness, to provide desired optical, electrical, or wetting properties. Adding the dye in polymer solution did not effect on the aspect ratio and the amplitude of patterned surface. The pitch size and the wet film thickness strongly influence on the amplitude of the texture formation. The molecular weight of polymers did not effect on the amplitude of the texture formation.

4.6 References

1. Ming, W.; Wu, D.; van Benthem, R.; de With, G., Superhydrophobic Films from Raspberry-like Particles. *Nano Letters* **2005,** 5, (11), 2298-2301.

2. Clapham, P. B.; Hutley, M. C., Reduction of Lens Reflexion by the "Moth Eye" Principle. *Nature* **1973,** 244, (5414), 281-282.

3. Verneuil, E.; Ladoux, B. t.; Buguin, A.; Silberzan, P., Adhesion on Microstructured Surfaces. *The Journal of Adhesion* **2007,** 83, (5), 449-472.

4. Efimenko, K.; Finlay, J.; Callow, M. E.; Callow, J. A.; Genzer, J., Development and Testing of Hierarchically Wrinkled Coatings for Marine Antifouling. *ACS Applied Materials & Interfaces* **2009,** 1, (5), 1031-1040.

5. Fuller, K. N. G.; Tabor, D., The Effect of Surface Roughness on the Adhesion of Elastic Solids. *Proc. R. Soc. Lond. A* **1975,** 345, (1642), 327-342.

6. Scardino, A. J.; de Nys, R., Mini review: Biomimetic models and bioinspired surfaces for fouling control. *Biofouling* **2011,** 27, (1), 73-86.

7. Chandra, D.; Yang, S.; Lin, P.-C., Strain responsive concave and convex microlens arrays. In 2007; Vol. 91, pp -.

8. Jeong, H. E.; Kwak, M. K.; Suh, K. Y., Stretchable, Adhesion-Tunable Dry Adhesive by Surface Wrinkling. *Langmuir* **2010,** 26, (4), 2223-2226.

9. Ahmed, S. F.; Rho, G.-H.; Lee, K.-R.; Vaziri, A.; Moon, M.-W., High aspect ratio wrinkles on a soft polymer. *Soft Matter* **2010,** 6, (22), 5709-5714.

10. Rao, J.; Winfield, R.; Keeney, L., Moth-eye-structured light-emitting diodes. *Optics Communications* **2010,** 283, (11), 2446-2450.

11. Bowden, N.; Huck, W. T. S.; Paul, K. E.; Whitesides, G. M., The controlled formation of ordered, sinusoidal structures by plasma oxidation of an elastomeric polymer. In 1999; Vol. 75, pp 2557-2559.

12. Menard, E.; Meitl, M. A.; Sun, Y.; Park, J.-U.; Shir, D. J.-L.; Nam, Y.-S.; Jeon, S.; Rogers, J. A., Micro- and Nanopatterning Techniques for Organic Electronic and Optoelectronic Systems. *Chemical Reviews* **2007,** 107, (4), 1117-1160.

13. Nie, Z.; Kumacheva, E., Patterning surfaces with functional polymers. *Nat Mater* **2008,** 7, (4), 277-290.

14. Georgiadis, A.; Routh, A. F.; Murray, M. W.; Keddie, J. L., Bespoke periodic topography in hard polymer films by infrared radiation-assisted evaporative lithography. *Soft Matter* **2011,** 7, (23), 11098-11102.

15. Parneix, C.; Vandoolaeghe, P.; Nikolayev, V. S.; D., Q.; Li, J.; Cabane, B., Dips and Rims in Dried Colloidal Films. *Physical Review Letters* **2010,** 105, (26), 266103.

16. Chiche, A.; Stafford, C. M.; Cabral, J. T., Complex micropatterning of periodic structures on elastomeric surfaces. *Soft Matter* **2008,** 4, (12), 2360-2364.

17. Bowden, N.; Brittain, S.; Evans, A. G.; Hutchinson, J. W.; Whitesides, G. M., Spontaneous formation of ordered structures in thin films of metals supported on an elastomeric polymer. *Nature* **1998,** 393, (6681), 146-149.

18. Yang, S.; Khare, K.; Lin, P.-C., Harnessing Surface Wrinkle Patterns in Soft Matter. *Advanced Functional Materials* **2010,** 20, (16), 2550-2564.

19. Srinivasarao, M.; Collings, D.; Philips, A.; Patel, S., Three-Dimensionally Ordered Array of Air Bubbles in a Polymer Film. In 2001; Vol. 292, pp 79-83.

20. Bassou, N.; Rharbi, Y., Role of Bénard−Marangoni Instabilities during Solvent Evaporation in Polymer Surface Corrugations. *Langmuir* **2008,** 25, (1), 624-632.

21. Xu, S.; Li, M.; Mitov, Z.; Kumacheva, E., Surface textures induced by convection in thin films of polymeric and polymerizable fluids. *Progress in Organic Coatings* **2003,** 48, (2-4), 227-235.

22. Schift, H.; David, C.; Gabriel, M.; Gobrecht, J.; Heyderman, L. J.; Kaiser, W.; Köppel, S.; Scandella, L., Nanoreplication in polymers using hot embossing and injection molding. *Microelectronic Engineering* **2000,** 53, (1-4), 171-174.

23. Schift, H.; Jaszewski, R. W.; David, C.; Gobrecht, J., Nanostructuring of polymers and fabrication of interdigitated electrodes by hot embossing lithography. *Microelectronic Engineering* **1999,** 46, (1-4), 121-124.

24. Leech, P. W., Lee, Robert A., Davis, Tim J., Printing via hot embossing of optically variable images in thermoplastic acrylic lacquer. *Microelectronic Engineering* **2006,** 83, (10), 1961-1965.

25. Jeon, S.; Kang, J.-W.; Park, H.-D.; Kim, J.-J.; Youn, J. R.; Shim, J.; Jeong, J.-h.; Choi, D.-G.; Kim, K.-D.; Altun, A. O.; Kim, S.-H.; Lee, Y.-H., Ultraviolet nanoimprinted polymer nanostructure for organic light emitting diode application. *Appl. Phys. Lett.* **2008,** 92, (22), -.

26. Routh, A. F.; Russel, W. B., Horizontal drying fronts during solvent evaporation from latex films. *AIChE Journal* **1998,** 44, (9), 2088-2098.

27. Harris, D. J.; Hu, H.; Conrad, J. C.; Lewis, J. A., Patterning Colloidal Films via Evaporative Lithography. *Physical Review Letters* **2007,** 98, (14), 148301.

28. Harris, D. J.; Conrad, J. C.; Lewis, J. A., Evaporative lithographic patterning of binary colloidal films. *Phil. Trans. R. Soc. A* **2009,** 367, (1909), 5157-5165.

29. Georgiadis, A.; Muhamad, F. N.; Utgenannt, A.; Keddie, J. L., Aesthetically textured, hard latex coatings by fast IR-assisted evaporative lithography. *Progress in Organic Coatings* **2013,** 76, (12), 1786-1791.

30. Utgenannt, A.; Keddie, J. L.; Muskens, O. L.; Kanaras, A. G., Directed organization of gold nanoparticles in polymer coatings through infrared-assisted evaporative lithography. *Chemical Communications* **2013,** 49, (39), 4253-4255.

31. J. L. Keddie; Routh, A. F., *Fundamentals of Latex Film Formation: Processes and Properties*. Springer: Dordecht, 2010; Vol. Chapter 1.

32. Georgiadis, A.; Bryant, P. A.; Murray, M.; Beharrell, P.; Keddie, J. L., Resolving the Film-Formation Dilemma with Infrared Radiation-Assisted Sintering. *Langmuir* **2011,** 27, (6), 2176-2180.

33. Jarusuwannapoom, T.; Hongrojjanawiwat, W.; Jitjaicham, S.; Wannatong, L.; Nithitanakul, M.; Pattamaprom, C.; Koombhongse, P.; Rangkupan, R.; Supaphol, P., Effect of solvents on electro-spinnability of polystyrene solutions and morphological appearance of resulting electrospun polystyrene fibers. *European Polymer Journal* **2005,** 41, (3), 409-421.

Chapter 5

Crystalline Nanocellulose with Sol-Gel Impregnation and with a Matrix of Latex Particles

Crystalline Nanocellulose with Sol-Gel Impregnation and with a Matrix of Latex Particles

*Chakkresit Chindawong and Diethelm Johannsmann**

Institute of Physical Chemistry, Clausthal University of Technology
39678 Clausthal-Zellerfeld, Germany

5.1 Abstract

Films of crystalline nanocellulose impregnated with a sol-gel solution were prepared by spin-coating CNC film. Spin-coating assembly methods gave smooth, stable and thin films. The films display birefringence as a result of the intrinsic shape and optical anisotropy of rod-like cellulose nanocrystals which were oriented by the spin-coating process. Films prepared by spin-coating displayed radial orientation of the rod-shaped cellulose nanocrystals. The crystalline nanocellulose impregnated with sol-gel was stable in water.

Keywords: *cellulose nanocrystals, sol-gel*

5.2 Introduction

Cellulose nanocrystals (CNC) are renewable and low cost nanomaterials with important optical and mechanical properties. They have outstanding mechanical properties such as a high aspect ratio, low density (1.566 g/cm^3), high elastic modulus 110-200 GPa and a reactive surface that facilitates grafting chemical species to achieve different surface properties (surface functionalization) and improved dispersion within a matrix polymer.[1-5] These features are favorable for the use of CNCs in composites. Favier et al.[6] completed the first study on CNC composites and observed that the addition of CNCs caused retention in the composite shear modulus at temperatures higher than the glass-transition temperature (T_g) of the matrix material. It has been reported previously that an aqueous suspension of cellulose nanocrystals prepared by sulfuric acid treatment of cellulose microfibrils separates into two phases above a critical concentration.[7] Sulfuric acid-hydrolyzed cellulose is often referred to as microcrystals, whiskers[8], nanocrystals, microcrystallites, or microfibrils. Here after, sulfuric acid-treated cellulose is called "cellulose nanocrystals".[9, 10] The upper layer is isotropic, and the lower layer forms a chiral nematic liquid crystalline phase. The phase separation phenomenon and chiral nematic texture of cellulose nanocrystal suspensions for cotton and wood cellulose have been extensively studied.[9, 11-14] The suspension viscosities and shape parameter of cellulose nanocrystals (CNC) were investigated by Yaman Boluk et al.[15] The properties and applications of cellulose nanocrystal suspensions were reviewed recently.[16-27] Cellulose and many cellulose derivatives display positive uniaxial birefringence and preparing ordered solid samples can maximize this anisotropy.[28] The applications of birefringent materials are extensive and include polarizers, waveguides, recording media, electro-optic modulators, and optical and biological sensors.

Birefringence can also be used to determine the macroscopic liquid crystal order parameter which is essential to the characterization of liquid crystals. Birefringence (also called optical anisotropy or double refraction) is defined as $\Delta n = n_e - n_o$ where n_e is the refractive index of light polarized parallel (extraordinary) to the optical axis and n_o is for polarizations perpendicular (ordinary) to the optical axis. The refractive index is a function of the molecular composition, orientation and packing within a material. The native form of cellulose (cellulose I), occurs as metastable partially crystalline

microfibrils. These microfibrils are composed of mixtures of two different crystalline polymorphs, designated cellulose Iα and Iβ.[28] The Iα crystal structure dominates in cellulose from cotton and it has been found to have a one-chain triclinic unit cell.[29, 30] The birefringence of cellulose ranges from 0.045 to 0.062 (depending on the source) with a refractive index parallel to the crystal axis of 1.576–1.595 and perpendicular to the chain direction of 1.527–1.534 for cotton.[31]

The sol–gel reaction involves the hydrolysis of silica precursors and condensation of the resulting hydroxyl groups to form a nanostructure. The sol–gel process has been widely used in the fields of mesoporous materials, membrane materials and intelligent hybrid hydrogel.[32, 33, 34-37] One simple method is mixing organic compounds with a metal alkoxide ((-$M(OR)_n$, where M is Si, Ti, Al, etc., and R is CH_3, C_2H_5, C_3H_7, etc.) such as tetraethoxysilane (TEOS). During the sol–gel process the inorganic mineral is deposited in the organic compound matrix forming hydrogen bonding between organic phase and inorganic phase. Another method is to introduce triethoxysilyl groups into the organic compounds prior to the sol–gel reactions with TEOS. Some organic/inorganic hybrid on the basis of different inorganic precursors and organic compounds, such as chitosan, silica, PVA have been reported.[33, 38-42] Several applications have been already developed for this kind of hybrid materials particularly in the biomedical field.[43] The dispersed inorganic particles impart the properties of hardness, brittleness, and transparency, whereas density, free volume and thermal stability depend on the organic host polymer.[33] Conventionally, the sol-gel coating film has employed solution-dipping (or dip-coating) in beakers of various sizes containing dilute aqueous polymer solutions. This inexpensive method works for most substrates independent of shape but has not always resulted in adequately homogeneous films. Alternatively, spin-coating is the most widely used technique for obtaining uniform films in lithography and other micromachining applications. The spin-coating process involves the acceleration of a liquid solution on a rotating substrate and is characterized by a balance of centrifugal forces (spin speed) and viscous forces (solution viscosity). Films created this way have been found to be consistent and reproducible in thickness,[44] showing enhanced local planarity when compared to solution-dipped films.[45, 46] This procedure eliminates edge defects often seen in solution-dipped films, whereby surface tension draws the solvent over the lip of

the substrate and removes excess fluid. Spin-coating has the advantage of requiring only small amounts of liquid to coat large areas. Spin-coating is mechanically controlled rather than thermodynamically controlled, giving novel film configurations that have recently gained attention.[28, 44, 47] The primary advantage of spin-coating, over solution-dipping, in the sol-gel assembly is the ability to vary parameters such as concentration, viscosity, solvent type, and spin speed, leading to films with variable thickness, density, and roughness.[32, 48, 49]

The aim of this study is to prevent re-dispersion of pure crystalline nanocellulose film in water. There are two ways to solve this problem. One is by blending CNC solution with latex solution. Another one is the impregnation of the CNC films in sol-gel solution. The latex dispersion was synthesized to blend with CNC solution. And the sol-gel solution also was synthesized to impregnate on CNC film by spin-coating and dip-coating. The morphology of all thin film was investigated by polarized optical microscope. The pencil hardness tester was used to determine the hardness of the film. The thickness of CNC/sol-gel impregnation was measured by using QCM.

5.3 Materials and Experimental

5.3.1 Materials

Cellulose nanocrystals (CNC, 1.05 wt% sulfur on dry CNC sodium form), produced by using 64% sulfuric acid to hydrolyze the amorphous regions of the cellulose polymer, leaving the acid resistant crystals as a product, were obtained in dry powder form from the Forest Products Laboratory (FPL), Process Development Center, University of Maine. Cellulose nanocrystals are rod-like particles approximately 5 nm in diameter and 150-200 nm long.[1] Dimensions are quite reproducible as long as the raw material is wood pulp from trees. Larger crystals can be produced using cotton (10 nm by 500 nm) or algae (20 nm by 1000 nm). The Forest Products Laboratory material is all produced from wood pulp and has the smaller dimension. Deionized water (18.2 MΩcm, Millipore Milli-Q Purification System) was used without pH adjustments to prepare aqueous solution with different concentration of CNC. Tetraethoxysilane (TEOS) was a commercial product supplied by Sigma-Aldrich Chem. Comp., Germany (purity, ≥ 99.9

% (GC)). Ethanol was a commercial product supplied by Merck, Germany (purity, ≥ 99.9 % (GC)). Hydrochloric acid (1 M) was used as catalysts.

5.3.2 Preparation of cellulose nanocrystal suspension in water

The cellulose nanocrystals suspension were prepared by dispersing the cellulose nanocrystals powder in deionized water. The concentration of suspension was varying from 2.5 – 15 wt%. Fig 5.1 show phase diagram.

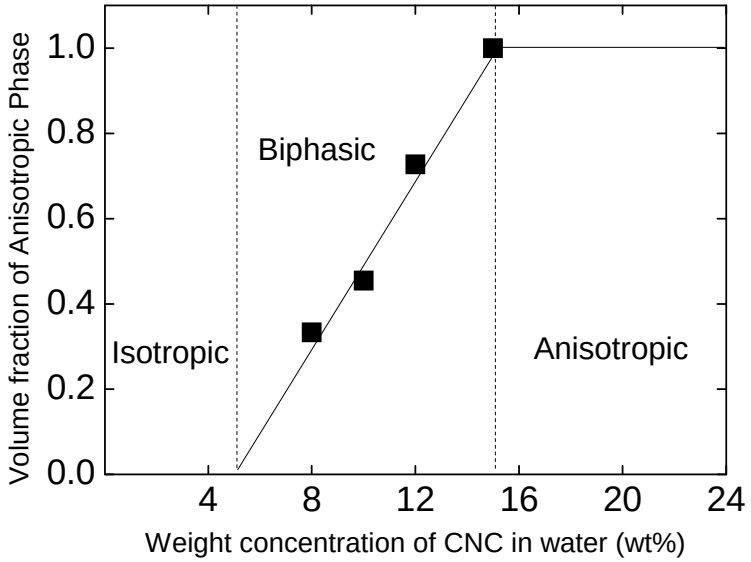

Figure 5.1. Phase transition diagram for a cellulose crystallite suspension in pure water.

It has been reported previously that an aqueous suspension of cellulose nonocrystals prepared by sulfuric acid treatment of cellulose microfilbrils separates into two phases above a critical concentration[7]. The critical concentration for the formation of the liquid crystalline phase is about 4.5–5.3 wt% for cellulose nanocrystals prepared by sulfuric acid treatment from cotton and wood.[9] Suspensions at concentrations above critical concentration separated into the isotropic phase (the upper layer) and chiral nematic phases (the lower layer) with a clear phase boundary.[9] At concentration above 15 wt%, the suspensions did not separate into two phases and become entirely liquid crystalline (anisotropic phase).[9, 50]

To compare the size of cellulose nanocrystals in the upper and lower layers, the spin-coating technique and the crossed polarizers with camera (Canon EOS1000D) or the polarizing optical microscope (ZEISS Axioplan) with camera (Canon PowerShot A590IS) were used. Parts a and b of Figure 5.2 show the polarizing optical images of the cellulose nanocrystals alignment prepared by spin-coating of the upper and lower layers, respectively. It was observed that the cellulose nanocrystals in the upper layer are shorter than those in the lower layer, suggesting an effective fractionation. This results agree with Hirai et al.[9]

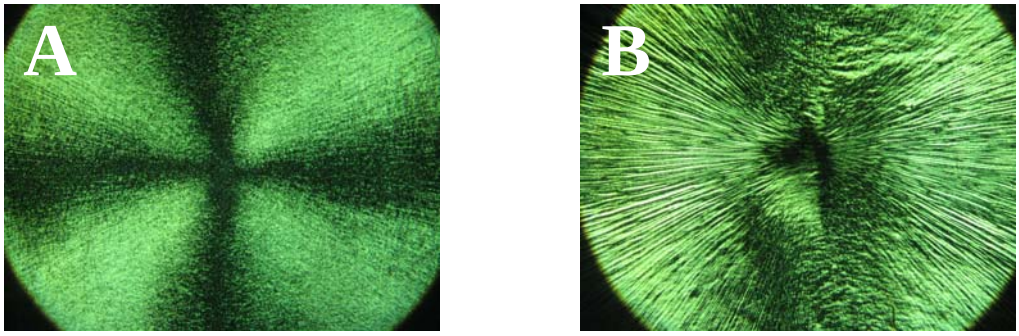

Figure 5.2 Orientation of cellulose nanocrystals. A and B showed polarized-light microscopic image of cellulose nanocrystals suspension in the isotropic phase (the upper layer) and the anisotropic phase (the lower layer), prepared by spin-coating on a glass substrate, respectively. The radial orientation and anisotropy of the crystals results in a Maltese cross pattern, visible between crossed polarizers. It is observed that the nanocrystals in the isotropic phase (the upper layer) are shorter than those in the anisotropic phase (the lower layer), suggesting an effective fractionation.

5.3.3 Preparation of sol-gel solution

TEOS 5.2 g, ethanol 25 g, deionized water 1 g, HCl (1 M) 1 g were mixed. Then the mixture was stirred for 30 min at 40 ^{0}C until a homogeneous solution was obtained.

5.3.4 Preparation of Latex dispersions

Latex dispersions were prepared by miniemulsion polymerization. The monomers were methylmethacrylate (MMA, Carl Roth, 99%, 49.5 wt%), *n*-butylacrylate (BA, Aldrich, 99%, 49.5 wt%), and acrylic acid (AA, Fluka, 99%, 1.4 wt%). The composition of the copolymer was 49.5/49.5/1 wt% MMA/BA/AA. Sodium dodecyl sulfate (SDS, Carl Roth, 99%, 2 wt%) was used as surfactant, hexadecane (HD, Aldrich, 99%, 3.7 wt%) was used as the co-stabilizer, and azo-*bis*-isobutyronitile (AIBN, 1.4 wt%) was used as the initiator. The samples were sonicated for 4 minutes and polymerized for 20 hours at 70 °C. The solids content of the latex dispersions was 20 wt%. The T_g according to the literature values for PMMA (105°C) and PBA (–54°C) and the Fox equation is 4°C. Since T_g is below room temperature, the material film-forms easily, both in pure form and when filled with nanocellulose.

5.3.5 Polarized-light microscopy

Polarized-light microscopy experiments employed a ZEISS Axioplan. Images were recorded with a Canon PowerShot A590IS camera mounted onto the microscope.

5.3.6 Hardness

The pencil hardness was measured with a Wolf-Wilburn Pencil Hardness tester (BYK-Gardner, Germany) following ISO 15184. The pencil hardness scale extends from 9H (hard) to 9B (not hard).

5.3.7 Refractive index

The refractive index was determined with the Abbe-Refractometer (Krüss Hamburg). The light source is Na-D line (wavelength = 589 nm). The working temperature is 20 ^{0}C. The Abbe refractometer measures the critical angle for a light ray passing between two media with different refractive indices.[55] The direction of a ray passing from some medium to the refractometer plate is governed by Snell's law, which relates the angles of incidence i and refraction r in a plane normal to the refractometer plate to the refractive indices of the medium n and the plate n_g by $n \sin i = n_g \sin r$. For n

$\leq n_g$, there is a critical angle r_c given by $n_g \sin r_c = n$, below which no light emerges from the medium. The critical angle occurs for light impinging on the surface at grazing angle ($i \rightarrow 90^0$). In the Abbe refractometer, the critical angle corresponds to a boundary between light and dark fields in the viewing optics, which are calibrated directly in refractive index units. Abbe refractometers often contain compensating prisms which correct for the dispersion when illuminated with white light, and give values for n corrected to the sodium *D* line (589 nm). All refractive indices reported here correspond to light of this wavelength. The refractive index of pure CNC solution and CNC/latex blend solution were measured with Abbe refractometer as a function of CNC concentration.

5.3.8 Dip-Coating Films

CNC/sol-gel films were assembled on glass substrate. The glass substrate was cleaned by UV/Ozone (UV/Ozone Bioforcenanoscience, INC, model: UV.TC.220, made in USA).[51-53] Spin-coated films were made with a commercial spin-coater (Spin Processor, Laurell Technologies Corporation, Model WS-650MZ-23NPP). UV/Ozone dry cleaning is effective in removing organic compounds, but is not effective in removing dust and inorganic salts. The films were prepared immediately after substrate cleaning. For instance, CNC suspension was poured on a stationary glass which was then accelerated at 1260 rpm/s and spun at 3000 rpm for 1 min. The film was then dipped in sol-gel solution with different immersion time. The prepared films were dried at ambient temperature and then put in oven at 120 ^{0}C for 2 hours to cure the sample from wet gel to dry gel.

5.3.9 Spin-Coating films

CNC/sol-gel films were assembled on disk of crystalline quartz. The disk of crystalline quartz was cleaned by UV/Ozone (UV/Ozone Bioforcenanoscience, INC, model: UV.TC.220, made in USA).[51-53] Spin-coated films were made with a commercial spin-coater (Spin Processor, Laurell Technologies Corporation, Model WS-650MZ-23NPP). UV/Ozone dry cleaning is effective in removing organic compounds, but is not effective in removing dust and inorganic salts. The QCM were measured for blank

quartz to make the reference. Sol-gel solution (300 μL) was poured on a disk of crystalline quartz which was then accelerated at 1260 rpm/s and spun at 3000 rpm for 1 min. Then the CNC suspension (300 μL) was poured directly onto the wet sol-gel layer and accelerated at 1260 rpm/s and spun at 3000 rpm for 1 min. The thickness of CNC film was varied by varying the spun speed at 3000, 6000 and 9000 rpm. The sample was measured by QCM. Then, the film was curing in oven at 120 ^{0}C for 2 hours and the sample was measured by QCM again. Sol-gel solution (300 μL) was poured directly onto sample again and then accelerated at 1260 rpm/s and spun at 3000 rpm for 1 min and the sample was measured by QCM again. Then, the film was curing in oven at 120 ^{0}C for 2 hours and the sample was measured by QCM again.

5.3.10 The Quartz Crystal Microbalance (QCM)

The QCM was used to measure the resonance frequencies and resonance bandwidths change, when the resonator is brought into contact with a sample. Typical resonance frequencies are 5, 15, 25, 35, 45, and 55 MHz. These shifts in frequency and bandwidth are the basis of QCM-based sensing. The sample might be a thin film, in which case the frequency shift is proportional to the mass permit area of the film according to the Sauerbrey relation. This proportionality motivates the name “quartz crystal microbalance”. The sample might also be a more complicated object. The “non-gravimetric QCM” requires modeling beyond the Sauerbrey equation. Such models exist and are put to use at many places. For QCM experiment, we can calculate the Sauerbrey thickness of CNC/sol-gel impregnated film.

5.4 Results and Discussion

5.4.1 Effect of concentration on the maltese cross orientation

In order to evaluate the effect of concentration on the maltese cross orientation. The spin-coating films with different concentration of pure CNC and CNC/latex blend were prepared. Table 5.1 demonstrates the digital photograph of single-layer film of pure CNC prepared by spin-coating on glass substrate at different concentration. We found that at 2.5 wt% and 4.0 wt% CNC concentrations did not showed the maltese cross orientation. At initial concentration 8.0 wt% and 10 wt% of pure CNC suspension, CNC

suspension separated into two phases (the isotropic phase (the upper layer) and chiral nematic phase (the lower layer)) with a clear phase boundary.[56-58] We found that the maltese cross orientation of anisotropic phase display rougher surface than the isotropic phase as shown in Fig. 5.2. The possible explanation is that the anisotropic phase has more viscosity, higher concentration, higher density and longer rod.[59] At concentration 15 wt% sample shows malteses cross orientation with rougher surface than those samples. Mixture of rod-like crystalline nanocellulose particles and spherical-like latex particles were prepared by weighting in approximate amounts of the stock dispersion. In this experiment, the weight ratio of stock solution is 1/1. Table 5.2 demonstrates the digital photograph displayed the maltese cross orientation of single-layer film of CNC-latex blend prepared by spin-coating on glass substrate at different CNC concentration. We found that at 2.5 wt% and 4.0 wt% CNC concentration blended with latex dispersion ratio 1/1 by weight of solution, samples did not show the maltese cross orientation. The 8 wt% and 10 wt% of isotropic CNC suspension blended with latex dispersion ration 1/1 by weight of solution did not show the maltese cross orientation while the 8 wt% and 10 wt% of anisotropic CNC suspension blended did shows maltese cross orientation. For wood-based CNCs, the dimension of rod-like CNC particles is 3-10 nm in diameter and 100-300 nm long.[1] At biphasic region (8 wt% and 10 wt% in this cause), the longer rod-like particles is in the lower layer (anisotropic phase form chiral nematic phase or chlolesteric phase) while shorter rod-like particle is in the upper layer (isotropic phase).[58, 59] The particle diameters of spherical-like particles of latex dispersion as determined by dynamic light scattering was 120 nm.[60] The longer rod-like particles and liquid crystalline properties in anisotropic phase of CNC dispersion can be used to induce the maltese cross orientation when it was blended with the latex dispersion. While the shorter rod-like like particle can not use to induce the maltese cross orientation when it was blended with the latex dispersion. Both isotropic suspensions mixed with latex dispersion and anisotropic suspensions mixed with latex dispersion have no phase separation after a period of several days. While latex dispersion was mixed with biphasic suspension, mixed by repeatedly inverting the vial, and allowed to stand. Phase separation was evident after a period of several days. After phase separation it was readily visible that the latex was enriched in the isotropic phase as shown in Fig. 5.3. The

spin-coating films of anisotropic CNC suspension blended with latex dispersion display the ordered micro-phase separation when observed under high magnification crossed-polarized light optical microscope, as shown in Fig. 5.4.

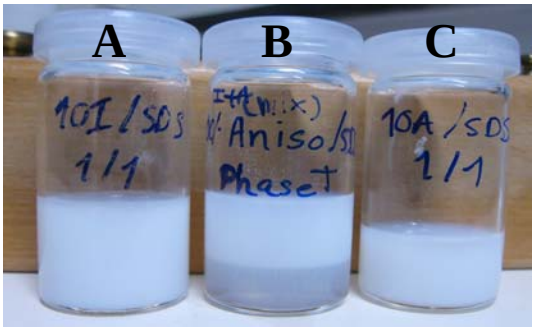

Figure 5.3 Digital photograph of samples (a) the isotropic CNC suspension mixed with latex, (b) the biphasic CNC suspension mixed with latex, showing the preferential partitioning of latex into the upper isotropic phase, and (c) the anisotropic suspension mixed with latex suspension.

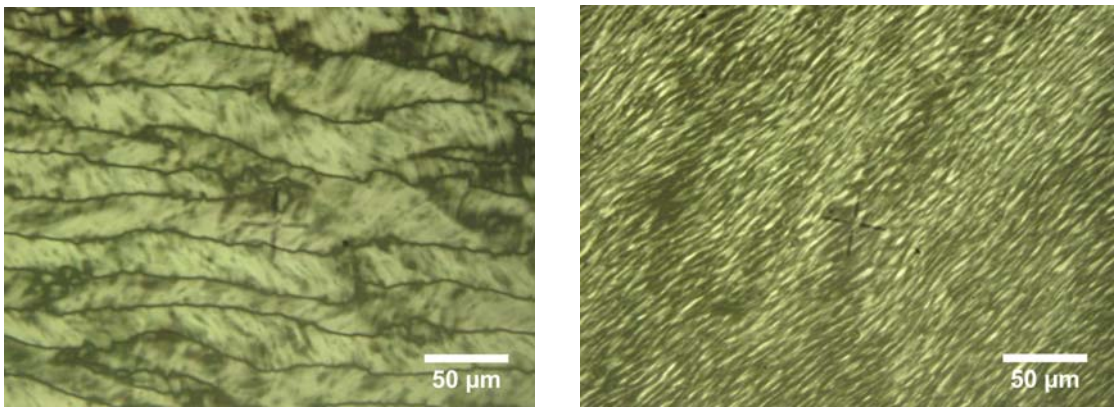

Figure 5.4 The crossed-polarized light optical micrograph of samples (a) the pure anisotropic CNC suspension prepared by spin-coating on glass substrate, showing a fan-shape texture of chiral nematic phase. (b) the anisotropic CNC suspension mixed with latex prepared by spin-coating on glass substrate, showing ordered micro-phase separation.

Table 5.1 The digital photograph of single-layer film of pure CNC prepared by spin-coating on glass (500 μL, accelerated at 1260 rpm/s, spun at 3000 rpm for 1 min).

Sample	Initial concentration (wt%)	pH	Crossed-Polarized light optical microscope image (2.5X)
CNC	2.5	6	 **No maltese cross**
	4.0	6	 **No maltese cross**
	8.0 (Anisotropic)	6	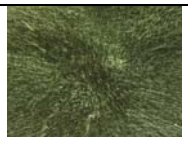 **maltese cross**
	8.0 (Isotropic)	6	 **maltese cross**
	10.0 (Anisotropic)	6	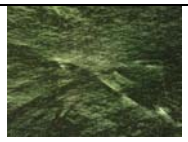 **maltese cross**
	10.0 (Anisotropic)	6	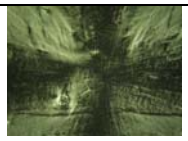 **maltese cross**
	15.0	6	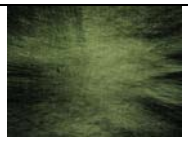 **maltese cross**

Table 5.2 The morphology of single-layer film of CNC latex blend prepared by spin-coating on glass (500 μL, accelerated at 1260 rpm/s, spun at 3000 rpm for 1 min).

Sample	Initial concentration (wt%)	pH	Polarized optical microscope image (2.5X)
CNC/ MMA/BA(50/50) (1/1)	2.5	3	 **No maltese cross**
	4.0	3	 **No maltese cross**
	8.0 (Anisotropic)	3	 **maltese cross**
	8.0 (Isotropic)	3	 **No maltese cross**
	10.0 (Anisotropic)	3	 **maltese cross**
	10.0 (Isotropic)	3	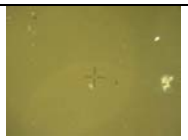 **No maltese cross**
	15.0	3	 **maltese cross**

5.4.2 Effect of concentration on refractive index

In order to evaluate the effect of concentration on refractive index of pure CNC suspension and CNC/latex blend. The CNC suspensions with concentration in the range 2.5 – 15 wt% were prepared. Fig. 5.3 demonstrates the plot of the refractive index versus the CNC concentration.

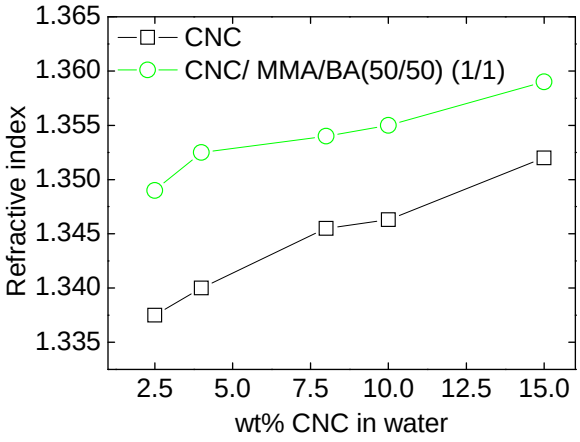

(a)

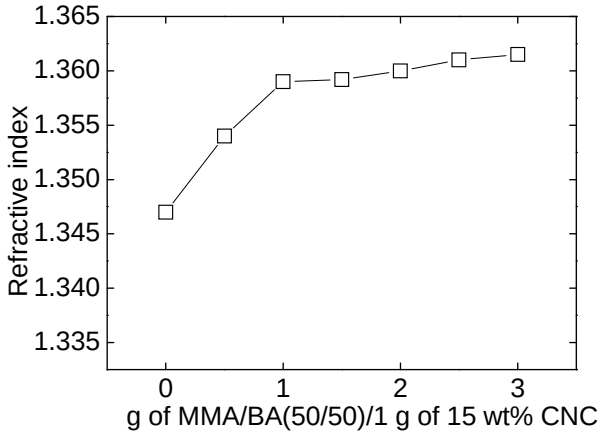

(b)

Figure 5.3 The plot of the refractive index versus the CNC concentration. (a) the plot of refractive index versus pure CNC and the plot of refractive index versus CNC/latex blend at different CNC concentration. (b) the plot of refractive index versus latex content.

We found that the refractive index of solution trend to increase when the concentration of pure CNC and CNC/latex blend increase. The refractive index of CNC/latex solution increase when the latex content increases. This means that blending the latex dispersion with CNC dispersion led to increasing of the refractive index of solution.

5.4.3 Effect of multilayer coating on the maltese cross orientations

In order to evaluate the effect of multi-layer coating on the maltese cross orientation. The 8 wt% anisotropic phase and 10 wt% anisotropic phase of CNC suspension were blended with latex dispersion (MMA/BA(50/50)) in weight ratio 1/1. The samples solution were spin-coated on glass substrate by vary the layer from 1 to 4. Table 5.3 demonstrates the digital photograph of single layer and multilayer of CNC/latex blend films prepared by spin-coating on glass substrate.

Radial orientation of cellulose nanocrystals implies that the centers of the films are more isotropic over the 1 mm^2 area probed by the ellipsometry laser.[28] The digital photograph reveals that the roughness of surface increases when number of layer increase. There are many methods to determine the films thickness such as AFM (scratch-height analysis), ellipsometry, wavelength-dependent optical reflectometry and angle-dependent optical reflectometry). The measurement of the film thickness is not the point of our study here.

Table 5.3 The digital photograp of multi-layer film of CNC latex blend prepared by spin-coating on glass (single-layer: 500 μL, accelerated at 1260 rpm/s, spun at 3000 rpm for 1 min).

Sample	**Initial concentration (wt%)**	**layer**	**Crossed-Polarized light optical microscope image (2.5X)**
CNC/ MMA/BA(50/50) (1/1)	8 Anisotropic	1	
		2	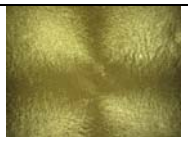
		3	
		4	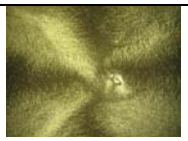
	10 Anisotropic	1	
		2	
		3	
		4	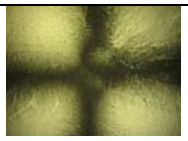

5.4.4 Effect of spin speed on the maltese cross orientation

In order to evaluate the effect of spin speed on the maltese cross orientation. The fixed volume (500 μL) of 8 wt% CNC isotropic suspension was spin-coated on glass substrate at different spin speed. The digital photograph showing "Maltese cross" orientation of cellulose nanocrystals between crossed polarizers at different spin speed was shown in Table 5.4.

Table 5.4 The digital photograph of single layer film of pure CNC suspension (8 wt% isotropic phase) prepared by spin-coating on glass substrate at different spin speed.

sample	Volume (μL)	Acceleration (rpm/s)	Spin speed (rpm)	Crossed-polarized light optical microscope image	
				2.5x	40.0x
8 wt% isotropic	500	1260	500	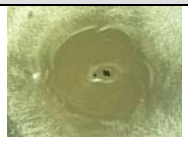	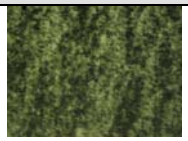
			1000		
			3000		
			6000		
			9000		

We found that at high spin speed gave a maltese crosss orientation better than low spin speed. At spin speed 500 rpm, the digital photograph of the sample did not show a good maltese cross orientation. The maltese cross orientation means the cellulose nanocrystal radial-aligned in plane of surface. This means that higher spin speed gave a good cellulose nanocrystal alignment better than lower spin speed.

5.4.5 Effect of latex content on the maltese cross orientation

In order to evaluate the effect of latex content on maltese cross orientation. The 15 wt% CNC suspension was mixed with latex dispersion at different latex ratio. The weight ratio of 15 wt% CNC suspension/latex dispersion was vary from 1/0, 1/0.5, 1/1, 1/1.5, 1/2, 1/2.5, 1/3 and 0/1. The solution mixtures were spin-coated on glass substrate. The digital photograph of polymeric film is shown in Table 5.6.

We found that the maltese cross orientation slightly disappear when the latex content increase as shown in Table 5.6. The CNC suspension consist of negative charge rod-like nanoparticles, because of sulfuric acid hydrolysis of cellulose, dispersed in water while the latex dispersion consist of negative charge spherical-like nanoparticles, because of a polar group of SDS surfactant, dispersed in water. The CNC suspension, rod-like nanoparticles, spin-coated on glass substrate led to radial alignment of rod-like nanoparticle while latex dispersion, spherical-like nanoparticles, spin-coated on glass did not display radial alignment when look under crossed-polarized light microscope. A good explanation relies on the latex film formation process. When the water evaporates, the spherical-like naonparticles in latex dispersion can deform, until the voids between particles have completely closed. The contacted particles then coalesce, which ultimately results in a continuous thin film without radial alignment. For the CNC suspension, when the water evaporates, the rod-like naoparticles can align by rational shearing and pack together without particles deformation and particle coalescence which led to radial orientation as can see the maltese cross orientation under crossed-polarized light microscope.

Table 5.6 The digital photograph of CNC suspension mixed with latex dispersion at different weight of solution ratio prepared by spin-coating.

Ratio of 15 wt% CNC/ MMA/BA(50/50) (g/g)	**pH**	**Crossed-polarized light optical microscope image**		**waterproof**	**Delamination on glass substrate when soaked in water**
		2.5x	**40x**		
1/0	6		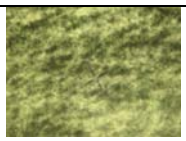	No	-
1/0.5	4	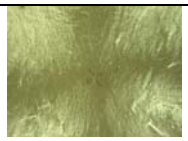		Yes	Yes
1/1	3			Yes	Yes
1/1.5	3			Yes	Yes
1/2	3			Yes	Yes
1/2.5	3			Yes	Yes
1/3	3			Yes	Yes
0/1	3			Yes	Yes

5.4.6 Hardness

In order to measure the hardness of polymeric films, the samples prepared by spin-coating CNC film on glass substrate and follow by dip in sol-gel solution at different immersion time were investigated by pencil hardness tester. Interestingly, the pencil hardness did not change when immersion time increase. Table 5.7 shows, the dipping time and pencil hardness. The pencil hardness of all films prepared by dip-coating with sol-gel solution is 8B.

Table 5.7 The spin-coating CNC film with sol-gel dip-coating

Procedure	1	2	3	4	5
1. spin-coating CNC	yes	yes	yes	yes	yes
2. dips in sol-gel solution	5 min	10 min	15 min	20 min	30 min
3. oven 120 ^{0}C	2 hour	2 hour	2 hour	2 hour	2 hour
4. dips in congo red solution (red color absorb on the film)	yes	yes	yes	yes	yes
5. the red color can wash off by water	yes	yes	yes	yes	yes
6. the film stable in water	yes	yes	yes	yes	yes
7. Pencil hardness test	8B	8B	8B	8B	8B
8. waterproof	yes	yes	yes	yes	yes
9. Delamination occured	No	No	No	No	No

We found that the pencil hardness of sample did not change when immersion time increase. For the formation of sol-gel coatings there must be chemical bonding between the film and the substrate, as is the case for glaze of metal, porcelain and glass substrates. The adhesion of the oxide coating film to the oxide substrates (glass substrate) is achieved by formation of chemical bonds -Si-O-Si' where Si and Si' are a tetravalent metalloid in the film and substrate, respectively, on heating to a certain high temperature. For metal substrates, the bond is formed through a thin oxide layer. It has been shown that the formation of-Si-O-Si' bonds at high tempratures may be easier when many –Si'OH and -SiOH groups are present at the contacting surfaces of the film and the

substrate.[62] The spin-coated CNC films impregnated with sol-gel solution by dip-coating method. When soak the films in water, the pure CNC films can re-disperse in water while the CNC/latex blend did not re-disperse in water but it can delaminate from glass substrate. The spin-coated CNC film impregnated with sol-gel solution by dip-coating method did not re-disperse in water and did not delaminate from glass substrate.

5.4.7 QCM Measurement

In order to measure the Sauerbrey thickness. The disk of crystalline quartz was used to be substrate. Sol-gel solution (300 μL) was poured on a disk of crystalline quartz which was then accelerated at 1260 rpm/s and spun at 3000 rpm for 1 min. Then the CNC suspension (300 μL) was poured directly onto the wet sol-gel layer and accelerated at 1260 rpm/s and spun at 3000 rpm for 1 min. The thickness of CNC film was varied by varying the spun speed at 3000, 6000 and 9000 rpm. The sample was measured by QCM. Then, the film was curing in oven at 120 ^{0}C for 2 hours and the sample was measured by QCM again. Sol-gel solution (300 μL) was poured directly onto sample again and then accelerated at 1260 rpm/s and spun at 3000 rpm for 1 min and the sample was measured by QCM again. Then, the film was curing in oven at 120 ^{0}C for 2 hours and the sample was measured by QCM again. The QCM were measured for blank quartz to make the reference. The result of Sauerbrey thickness was list in table 5.8.

Table 5.8 The result of Sauerbrey thickness at different spin speed of CNC.

	Sauerbrey thickness (nm)		
	3000 rpm	6000 rpm	9000 rpm
Sol-gel-CNC	650-655	395-405	384-400
Sol-gel-CNC Curing	640	383-392	375-393
Sol-gel-CNC Curing Sol-gel	950	702-710	700-713
Sol-gel-CNC Curing Sol-gel Curing	912	670-675	670-681
Sol-gel-CNC Curing Sol-gel Curing under salt (%RH= 85.11 ± 0.29)	905-915	660-670	660-675

We found that the Sauerbrey thickness tend to decrease when the spin speed increase. Cured film led to decreasing of the Sauerbrey thickness. This result means that the sol-gel solution can impregnate with CNC. And we also found that the sol-gel/CNC film did not re-dispersed in water while pure CNC film did re-dispersed in water.

5.5 Conclusion

The pure CNC spin-coating film on glass substrate displays maltese cross orientation under crossed-polarized light but the film can re-dispersed in water.

The isotropic CNC/latex blend spin-coating film on glass substrate did not display maltese crosss orientation under crossed-polarized light while anisotropic CNC/latex blend display maltese crosss orientation under crossed-polarized light. The CNC/latex blend film on glass substrate did not re-dispersed in water but can delaminate from glass substrate when soak in water.

The spin-coated CNC film impregnated with sol-gel solution did not re-disperse in water and did not delaminate from glass substrate when soak in water. The pencil hardness of films is 8B.

5.6 References

1. Roya R. Lahiji; Xin Xu; Ronald Reifenberger; Arvind Raman; Alan Rudie; Moon, R. J., Atomic Force Microscopy Characterization of Cellulose Nanocrystals. *langmuir* **2010,** 26, (6), 4480-4488.

2. Azizi Samir, M. A. S., Alloin, Fannie, Dufresne, Alain, Review of Recent Research into Cellulosic Whiskers, Their Properties and Their Application in Nanocomposite Field. *Biomacromolecules* **2005,** 6, (2), 612-626.

3. Olivier, C.; Moreau, C.; Bertoncini, P.; Bizot, H.; Chauvet, O.; Cathala, B., Cellulose Nanocrystal-Assisted Dispersion of Luminescent Single-Walled Carbon Nanotubes for Layer-by-Layer Assembled Hybrid Thin Films. *Langmuir* **2012,** 28, (34), 12463-12471.

4. Kim, J.; Montero, G.; Habibi, Y.; Hinestroza, J. P.; Genzer, J.; Argyropoulos, D. S.; Rojas, O. J., Dispersion of Cellulose Crystallites by Nonionic Surfactants in a

Hydrophobic Polymer Matrix. *Polymer Engineering and Science* **2009,** 49, (10), 2054-2061.

5. ALEXANDER B. REISING, R. J. M., JEFFREY P. YOUNGBLOOD; Alexander B. R., R. J. M., Jeffrey P. Y.,, Effect of Particle Alignment on Mechanical Properties of Neat Cellulose Nanocrystal Films. *Journal of Science & Technology for Forest Products and Processes* **2012,** 2, (6).

6. Favier, V.; Chanzy, H.; Cavaille, J. Y., Polymer Nanocomposites Reinforced by Cellulose Whiskers. *Macromolecules* **1995,** 28, (18), 6365-6367.

7. Revol, J. F.; Bradford, H.; Giasson, J.; Marchessault, R. H.; Gray, D. G., Helicoidal self-ordering of cellulose microfibrils in aqueous suspension. *International Journal of Biological Macromolecules* **1992,** 14, (3), 170-172.

8. Ni, H.; Zeng, S.; Wu, J.; Cheng, X.; Luo, T.; Wang, W.; Zeng, W.; Chen, Y., Cellulose nanowhiskers: Preparation, characterization and cytotoxicity evaluation. *Bio-Medical Materials and Engineering* 22, (1-3), 121-127.

9. Asako Hirai, O. I., Fumitaka Horii, and Masaki Tsuji, Phase Separation Behavior in Aqueous Suspensions of Bacterial Cellulose Nanocrystals Prepared by Sulfuric Acid Treatment. *Langmuir* **2009,** 25, 497-502.

10. Lu, P.; Hsieh, Y. L., Preparation and properties of cellulose nanocrystals: Rods, spheres, and network. *Carbohydrate Polymers* **2010,** 82, (2), 329-336.

11. Roman, M.; Gray, D. G., Parabolic focal conics in self-assembled solid films of cellulose nanocrystals. *Langmuir* **2005,** 21, (12), 5555-5561.

12. Revol, J.-F., L. Godbout, X. M. Dong, D. G. Gray, H. Chanzy and G. Maret, , Chiral Nematic Suspensions of Cellulose Crystallites; Phase-Separation and Magnetic-Field Orientation. *Liquid Crystals* **1994,** 16, 127–134.

13. J.-F. Revol, H. B., J. Giasson, R.H. Marchessault, D.G. Gray, Helicoidal self-ordering of cellulose microfibrils in aqueous suspension. *International Journal of Biological Macromolecules* **1992,** 14, 170-172.

14. Majoinen, J., Kontturi, E., Ikkala, O., Gray, D. G., SEM imaging of chiral nematic films cast from cellulose nanocrystal suspensions. *Cellulose* **2012,** 19, (5), 1599-1605.

15. Boluk, Y.; Lahiji, R.; Zhao, L.; McDermott, M. T., Suspension viscosities and shape parameter of cellulose nanocrystals (CNC). *Colloids and Surfaces A: Physicochemical and Engineering Aspects* **2011,** 377, (1-3), 297-303.

16. Beck, S.; J. Bouchard; Berry, R., Controlling the Reflection Wavelength of Iridescent Solid Films of Nanocrystalline Cellulose. *Biomacromolecules* **2011,** 12, 167–172.

17. Csoka, L.; Hoeger, I. C.; Peralta, P.; Peszlen, I.; Rojas, O. J., Dielectrophoresis of cellulose nanocrystals and alignment in ultrathin films by electric field-assisted shear assembly. *Journal of Colloid and Interface Science* 363, (1), 206-212.

18. Picard, G., Simon, D., Kadiri, Y., LeBreux, J. D., Ghozayel, F., Cellulose Nanocrystal Iridescence: A New Model. *Langmuir* **2012,** 28, (41), 14799-14807.

19. Peng, B. L.; Dhar, N.; Liu, H. L.; Tam, K. C., Chemistry and Applications of Nanocrystalline Cellulose and Its Derivatives: A Nanotechnology Perspective. *Canadian Journal of Chemical Engineering* **2011,** 89, (5), 1191-1206.

20. Habibi, Y.; Lucia, L. A.; Rojas, O. J., Cellulose Nanocrystals: Chemistry, Self-Assembly, and Applications. *Chemical Reviews* **2010,** 110, (6), 3479-3500.

21. Huang, J. L.; Li, C. J.; Gray, D. G., Cellulose Nanocrystals Incorporating Fluorescent Methylcoumarin Groups. *Acs Sustainable Chemistry & Engineering* **2013,** 1, (9), 1160-1164.

22. Charreau, H.; Foresti, M. L.; Vazquez, A., Nanocellulose Patents Trends: A Comprehensive Review on Patents on Cellulose Nanocrystals, Microfibrillated and Bacterial Cellulose. *Recent Patents on Nanotechnology* **2013,** 7, (1), 56-80.

23. Beck, S., Bouchard, J., Chauve, G., Berry, R., Controlled production of patterns in iridescent solid films of cellulose nanocrystals. *Cellulose* **2013,** 20, (3), 1401-1411.

24. Durán N, L. A., Seabra AB. , Review of cellulose nanocrystals patents: preparation, composites and general applications. . *Recent Pat Nanotechnol* **2012,** 6, 16-28.

25. Klemm, D., Kramer, Friederike, Moritz, Sebastian, Lindstrom, Tom, Ankerfors, Mikael, Gray, Derek, Dorris, Annie, Nanocelluloses: A New Family of Nature-Based Materials. *Angewandte Chemie-International Edition* **2011,** 50, (24), 5438-5466.

26. Heath, L.; Thielemans, W., Cellulose nanowhisker aerogels. *Green Chemistry* **2010,** 12, (8), 1448-1453.

27. Dufresne, A., Nano-cellulose from nature to high performance tailored materials. *Berlin de Gruyter* **2012**.

28. Cranston, E. D., Gray, Derek G., Birefringence in spin-coated films containing cellulose nanocrystals. *Colloids and Surfaces A: Physicochemical and Engineering Aspects* **2008,** 325, (1-2), 44-51.

29. A.A. Baker, W. H., J. Sugiyama, M.J. Miles, New Insight in cellulose structure by atomic force microscopy shows the Iα crystal phase at near-atomic resolution. *Biophys. J.* **2000,** 79, 1139–1145.

30. Y. Nishiyama, J. S., H. Chanzy, P. Langan, Crystal structure and hydrogen bonding system in cellulose I(alpha) from synchrotron X-ray and neutron fiber diffraction. *J. Am. Chem. Soc.* **2003,** 125 14300–14306.

31. D. Klemm, B. P., T. Heinze, U. Heinze, W. Wagenknecht, Comprehensive Cellulose Chemistry: Fundamental and Analytical Methods. *Wiley–VCH, Weinheim* **1998,** 1.

32. Belleville, P., Functional coatings: The sol-gel approach. *C. R. Chimie* **2010,** 13, 97–105.

33. Xie, K. L.; Yu, Y. H.; Shi, Y. Q., Synthesis and characterization of cellulose/silica hybrid materials with chemical crosslinking. *Carbohydrate Polymers* **2009,** 78, (4), 799-805.

34. Dujardin, E.; Blaseby, M.; Mann, S., Synthesis of mesoporous silica by sol-gel mineralisation of cellulose nanorod nematic suspensions. *Journal of Materials Chemistry* **2003,** 13, (4), 696-699.

35. Wojciechowska, P.; Foltynowicz, Z.; Nowicki, M., Synthesis and Characterization of Modified Cellulose Acetate Propionate Nanocomposites via Sol-Gel Process. *Journal of Spectroscopy*.

36. Samuneva, B.; Djambaski, P.; Kashchieva, E.; Chernev, G.; Kabaivanova, L.; Emanuilova, E.; Salvado, I. M. M.; Fernandes, M. H. V.; Wu, A., Sol-gel synthesis and structure of silica hybrid biomaterials. *Journal of Non-Crystalline Solids* **2008,** 354, 733-740.

37. Hou, A.; Shi, Y.; Yu, Y., Preparation of the cellulose/silica hybrid containing cationic group by sol-gel crosslinking process and its dyeing properties. *Carbohydrate Polymers* **2009,** 77, (2), 201-205.

38. George, J.; Sajeevkumar, V. A.; Ramana, K. V.; Sabapathy, S. N.; Siddaramaiah, Augmented properties of PVA hybrid nanocomposites containing cellulose nanocrystals and silver nanoparticles. *Journal of Materials Chemistry* 22, (42), 22433-22439.

39. Zhou, Y. M.; Fu, S. Y.; Zheng, L. M.; Zhan, H. Y., Effect of nanocellulose isolation techniques on the formation of reinforced poly(vinyl alcohol) nanocomposite films. *Express Polymer Letters* 6, (10), 794-804.

40. I. Kvien.; K.Oksman, Orientation of cellulose nanowhiskers in polyvinyl alcohol. *Appl. Phys. A* **2007,** 87, 641–643.

41. de Mesquita, J. P.; Donnici, C. L.; Teixeira, I. F.; Pereira, F. V., Bio-based nanocomposites obtained through covalent linkage between chitosan and cellulose nanocrystals. *Carbohydrate Polymers* **2012,** 90, (1), 210-217.

42. Liu, H. Z.; Laborie, M. P. G., Bio-based nanocomposites by in situ cure of phenolic prepolymers with cellulose whiskers. *Cellulose* 18, (3), 619-630.

43. Wicklein, B.; Salazar-Alvarez, G., Functional hybrids based on biogenic nanofibrils and inorganic nanomaterials. *Journal of Materials Chemistry A* **2012,** 1, (18), 5469-5478.

44. Malkiat S. Johal , J. L. C., Peter A. Chiarelli , Ding-Guo Liu , Jennifer A. Shaw , Jeanne M. Robinson , and Hsing-Lin Wang Polyelectrolyte Trilayer Combinations Using Spin-Assembly and Ionic Self-Assembly. *Langmuir* **2003,** 19 (21), 8876–8881.

45. Cranston, E. D., Gray, D. G., Morphological and optical characterization of polyelectrolyte multilayers incorporating nanocrystalline cellulose. *Biomacromolecules* **2006,** 7, (9), 2522-2530.

46. Lee, S.-S.; Hong, J.-D.; Kim, C. H.; Kim, K.; Koo, J. P.; Lee, K.-B., Layer-by-Layer Deposited Multilayer Assemblies of Ionene-Type Polyelectrolytes Based on the Spin-Coating Method. *Macromolecules* **2001,** 34, (16), 5358-5360.

47. Schreckenbach*, A., Macroscopic structures in liquid crystal systems prepared with spin coating *Polymer* **1997** 38, (12), 3069-3083.

48. Lee, S.-S.; Lee, K.-B.; Hong, J.-D., Evidence for Spin Coating Electrostatic Self-Assembly of Polyelectrolytes. *Langmuir* **2003,** 19, (18), 7592-7596.

49. SAKKA, S., Preparation and Properties of Sol-Gel Coating Films. *Journal of Sol-Gel Science and Technology* **1994,** 2, 451-455.

50. Xue Min Dong; Tsunehisa Kimura; Jean-Francüois Revol; Gray, D. G., Effects of Ionic Strength on the Isotropic-Chiral Nematic Phase Transition of Suspensions of Cellulose Crystallites. *Langmuir* **1996,** 12, 2076-2082.

51. Vig, J. R., UV/ozone cleaning of surfaces. *J. Vac. Sci. Technol. A* **1985,** 3, (3), 1027-1034.

52. Oak Manufacturing Co., L., Ultraviolet-Ozone Surface Treatment. *Three Bond Technical News* 1987

53. Essential Points of UV/Ozone Dry cleaning. http://www.senlights.com/gijyuu/drycleaning/drycleaning.html

54. ASTM Committee D-1 on Paint and Related Coatings, M., and Applications Standard Test Method for Film Hardness by Pencil Test. *Physical Properties of Applied Paint Films.*

55. Laivins, G. V., Gray, D. G., Birefringence of a polymeric cholesteric liquid crystal measured by refractometry. *Journal of Applied Polymer Science* **1987,** 33, (1), 137-150.

56. Beck, S. C. PHASE SEPARATION PHENOMENA IN CELLULOSE NANOCRYSTAL SUSPENSIONS CONTAINING DEXTRAN-DYE DERIVATIVES. Ph.D. Thesis, McGill University, Canada, 2007.

57. Beck-Candanedo, S., Roman, Maren, Gray, Derek G., Effect of Reaction Conditions on the Properties and Behavior of Wood Cellulose Nanocrystal Suspensions. *Biomacromolecules* **2005,** 6, (2), 1048-1054.

58. Edgar, C. D.; Gray, D. G., Influence of Dextran on the Phase Behavior of Suspensions of Cellulose Nanocrystals. *Macromolecules* **2002,** 35, (19), 7400-7406.

59. Hirai, A. I., O. Horii, F. Tsuji, M., Phase Separation Behavior in Aqueous Suspensions of Bacterial Cellulose Nanocrystals Prepared by Sulfuric Acid Treatment. *Langmuir* **2009,** 25, (1), 497-502.

60. Irina Nikiforow; Jorg Adams; Alexander M. Konig; Arne Langhoff; Katja Pohl; Andrey Turshatov; Johannsmann, D., Self-Stratification During Film Formation from Latex Blends Driven by Differences in Collective Diffusivity. *Langmuir* **2010,** 26, (16), 13162-13167.

61. Koenderink, G. H.; Vliegenthart, G. A.; Kluijtmans, S. G. J. M.; van Blaaderen, A.; Philipse, A. P.; Lekkerkerker, H. N. W., Depletion-Induced Crystallization in Colloidal Rod-Sphere Mixtures. *Langmuir* **1999,** 15, (14), 4693-4696.

62. Sakka, S., Preparation and properties of sol-gel coating films. *Journal of Sol-Gel Science and Technology* **1994,** 2, (1-3), 451-455.

Chapter 6

An Anisotropic Ink Based on Crystalline Nanocellulose: Potential Application in Security Printing

An Anisotropic Ink Based on Crystalline Nanocellulose: Potential Applications in Security Printing

*Chakkresit Chindawong, Diethelm Johannsmann**

Institute of Physical Chemistry, Clausthal University of Technology,
38678 Clausthal-Zellerfeld, Germany

6.1 Abstract

Polymer dispersions containing crystalline nanocellulose (CNC) have been used as birefringent inks. When printed onto dark paper, the letters are darker than the background if viewed without polarizers, while they are brighter than the background if viewed with crossed polarizers. This type of contrast inversion can have applications in security printing and optical authentication.

* author for correspondence, electronic mail: johannsmann@pc.tu-clausthal.de

6.2 Introduction

Security printing relies on patterns, which are easily recognized, on the one hand, but are not easily forged, on the other.[1] Since recognition occurs by visual inspection, security printing often exploits features with a peculiar optical appearance. Examples are holograms, colored fibers, and watermarks. Intricate schemes of printing play a role, but particular types of inks (often combined with certain printing procedures) are used, as well. Such inks can make use of fluorescence,[2] up-conversion from the infrared, or opalescence (also called "iridescence").[3] The latter effect relies on interference. The resulting colors are impressive and, also, change with the angle of observation. A second class of optically variable inks (OVI's) relies on reflective pigment particles with platelet-shape.[1] If the platelets have a preferred orientation, their appearance depends on the angle of observation.

Birefringence is known to produce a variety of interesting optical effects (including angle-dependent colors), when the object of interest is placed between crossed polarizers and viewed in transmission. However, a peculiar appearance must be obtained in *reflection* (diffuse or specular), if it shall be of use in security printing. This entails a difficulty in so far, as the diffuse and depolarized reflection from a white background can easily mask all effects of polarization. White paper reflects light randomly, which implies that the polarization of the reflected photons is largely uncorrelated to the incident polarization. The depolarization is a consequence of multiple scattering. Many inks are similar to paper in this regard. They differ from the background in their color, but conventional inks are designed to be strong scatterers just like the paper itself, which entails multiple scattering. This behavior contrasts to the behavior of translucent, birefringent ink, for instance composed of crystalline nanocellulose (CNC). CNC layers scatter light only weakly. Because single scattering dominates, the polarization is preserved to a certain extent[4] and polarization effects can be observed even in diffuse reflection. However, the scattered intensity from the ink cannot be seen against an unpolarized background, if the latter is white paper. A white background spoils all polarization effects.

These problems can be overcome by applying the CNC-based ink to *dark* paper. With a dark background, multiple scattering is reduced to the extent that the diffuse reflectance is attenuated by a factor of 2 – 3 under crossed polarizers (see, for instance, Fig. 6.4). The preservation of polarization is the consequence of single scattering.[4]

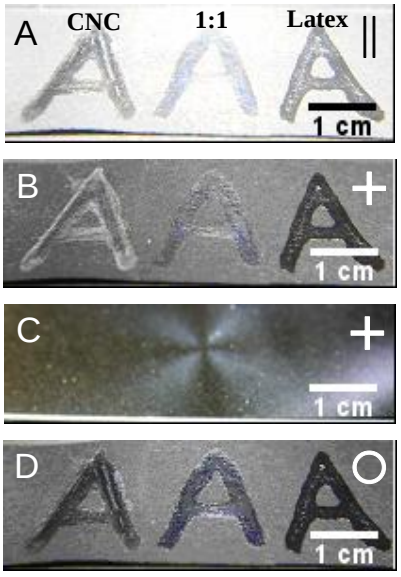

Figure 6.1 The letter "A" was written onto black paper with pure nanocellulose (left), a 1/1 mixture of nanocellulose with a latex dispersion (center), and a pure latex dispersion (right). The images in panels A, B, and D were acquired with parallel polarizers, with crossed polarizers, and without polarizers, respectively. Panel C shows a spin-cast film of nanocellulose imaged under same conditions as in panel B. Spin-casting leads to highly oriented films. One observes a Maltese cross in Panel C, where the center of the cross is the rotation axis during spin casting. When the principal axis of the birefringence makes an angle with the polarizers, the respective area appears bright. For the inks containing nanocellulose, there is contrast inversion between panels A and B. For the arrangement of the sample, the light source, the camera, and the polarizers see Fig. 6.3.

Fig. 6.1 demonstrates the effect. The letter "A" was written with pure nanocellulose (left), with a 1/1 mixture of nanocellulose and a polymer latex (center), and with a latex dispersion containing no nanocellulose (right). The different images were taken with parallel polarizers (A), crossed polarizers (B), and without polarizers (D). There is contrast inversion between panels A and B. Panel C shows a spin-cast latex films imaged with crossed polarizers as in panel B. Spin-casting orients the films, where the rods line up along the radial direction. Areas, inside which the rods makes an angle with the polarizers, appear bright (for similar reasons as in transmission). Panels B and D also differ in appearance, but the effects are less impressive. Fig. 6.1 was acquired in the laboratory with polarizers mounted in front

of the light source and the camera. However, devices visualizing polarization effects be simpler than that. Fig. 6.2 shows a sketch of a flash lamp with a polarizer glued to the front of the LED and a second polarizer attached to its side. The device can be cheap; its application is trivial.

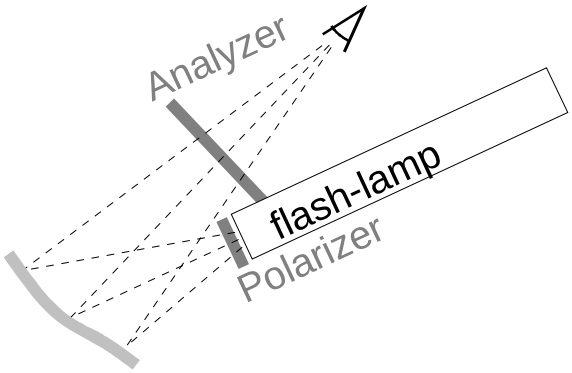

Figure 6.2 A simple testing device for polarizing inks.

Crystalline nanocellulose (CNC) has been known since the early 1950s.[5] Its availability has improved recently, which has led to a surge in interest. Overviews can be found in Refs. 6, 7, and 8. The focus in this work is on the optical properties of dried nanocellulose and on potential applications in optics. The material used (supplied by the Forest Products Laboratory, Madison, WI), is composed of nanorods with a diameter of 5 nm and a length in the range between 100 and 200 nm.[9] Dispersions in water are isotropic at concentrations below 5 % and form a chiral-nematic phase at concentrations larger than 15 %. There is phase coexistence between 5 and 15 %. The dried material forms a glassy phase with a smooth surface.[10,11]

Because the rods giving rise to liquid crystalline behavior are of colloidal dimensions, it is easy to produce alignment. Put differently, some kind of alignment actually cannot be avoided during application of the ink because the spreading process is accompanied by shear flow. Droplets applied by inkjet printing are birefringent. The pattern of orientation reflects the flow during deposition.[12] If good alignment is required, one can shear the material after deposition with a doctor blade as demonstrated in Refs. 13 and 14.

While birefringence and even intricate patterns of birefringence are easily obtained, it is difficult to achieve clear films for a number of reasons. Because cellulose is chiral, CNC dispersions (and also the dried films) have a tendency to develop twist. When blending nanocellulose with a polymer dispersion and shearing the material, one can overcome the twist and achieve uniaxial anisotropy, but these films still show a texture under the microscope. The texture may be caused by orientation fluctuations, concentration fluctuations, or packing defects. Packing imperfections can give rise to interesting super-structures as proposed in Ref. 15. Still, they amount to a problem in optical applications, where clarity would be desirable. Security printing in this regard is special. The application of nanocellulose as an ink does not require optical clarity. On the contrary, a small amount of turbidity helps to recognize the material as being special.

Security printing applications of nanocellulose have been proposed before.[16,17] Gray and co-workers have shown that nanocellulose dispersions can be dried in such a way that the material's chirality is preserved and that the pitch is in the range of the wavelength of light. The material then produces iridescent colors.[18] The effects discussed below are *not* based on chirality but rather on nematic order. We did observe a slight bluish coloration, occasionally, but we do not exploit it. Most of the time, the pitch was too long to generate interference colors. Chirality can still be useful for inks because chirality induces a specific texture.

Dispersions of nanocellulose are not practical inks because the dried material can be redispersed in water. However, a waterproof material with similar properties is obtained by blending the nanocellulose with a latex dispersion. Such blends have been studied before in the context of mechanical reinforcement.[19,20,21] A 1/1 (v/v) mixture of an acrylic latex blend with a glass temperature, T_g, of 4°C and a CNC dispersion was employed here. We will report on the film formation properties of CNC/latex blend separately. The focus here on the application as an ink.

6.3 Materials and Experimental

6.3.1 Crystalline Nanocelluloses

The crystalline nanocellulose employed was produced by the Forest Products Laboratory (FPL, Madison, WI) and purchased through the University of Maine.[22] Details on the production process and on material properties are provided on the homepage of the

University of Maine.[9] The nanocellulose was delivered in powder form and dispersed in water by sonication.

6.3.2 Latex dispersions

Latex dispersions were prepared by miniemulsion polymerization. The monomers were methylmethacrylate (MMA, Carl Roth, 99%, 49.5 wt%), *n*-butylacrylate (BA, Aldrich, 99%, 49.5 wt%), and acrylic acid (AA, Fluka, 99%, 1.4 wt%). The composition of the copolymer was 49.5/49.5/1 wt% MMA/BA/AA. Sodium dodecyl sulfate (SDS, Carl Roth, 99%, 2 wt%) was used as surfactant, hexadecane (HD, Aldrich, 99%, 3.7 wt%) was used as the co-stabilizer, and azo-*bis*-isobutyronitile (AIBN, 1.4 wt%) was used as the initiator. The samples were sonicated for 4 minutes and polymerized for 20 hours at 70 °C. The solids content of the latex dispersions was 20 wt%. The T_g according to the literature values for PMMA (105°C) and PBA (–54°C) and the Fox equation is 4°C. Since T_g is below room temperature, the material film-forms easily, both in pure form and when filled with nanocellulose.

CNC dispersions with weight concentrations between 5 and 15% phase-separate into an isotropic and a chiral-nematic phase. The CNC used for printing was always obtained from the anisotropic fraction of such phase-separated dispersions. From the phase diagram, the concentration is known to be 15wt%. The solids content of the mixture was 17 wt%. Spreading of the latex dispersion onto paper occurred from a pipette. On glass substrates, the material occasionally delaminates. The adhesion on paper is very good.

6.3.3 Spin-coating

For comparison, samples were also prepared by spin-casting (Laurell Technologies Corporation, Model WS-650MZ-23NPP, 3000 rpm).

Characterization mostly occurred as sketched in Fig. 6.3. The sample was illuminated with a white LED (Heitronic IP44) from the top. Conventional sheet polarizers were mounted in front of the lamp and in front of the camera. The observation angle of the camera was 45 degrees. The microscopic texture was studied by optical microscopy (Zeiss Axioplan) and by confocal laser scanning microscopy (DM IRBE Leica Microsystems).

The contrast inversion observed upon rotating the polarizer (cf. Fig. 6.1) was quantified on samples, which were applied straight lines (rather than letters). In order to obtain a well-defined average thickness, the area of application was limited with Scotch tape.

For the comparison of the brightness between the different orientations of the polarizers, the auto-gain function of the camera was switched off. Brightness is reported in arbitrary units. The brightness was averaged over a square millimeter in the center of the sample.

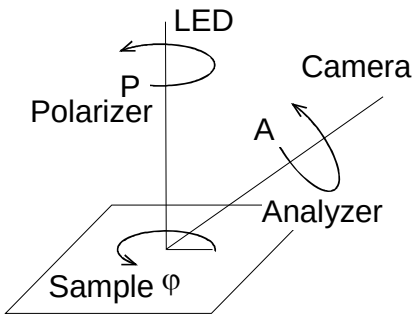

Figure 6.3 Geometry of the experiments underlying Figs. 6.1 and 6.4–6.

6.4 Results and Discussion

6.4.1 Polarization effects in diffuse reflection

Fig. 6.4 shows the brightness versus the angle of the polarizer for samples with an average thickness of 60 µm. Squares correspond to the pure nanocellulose, upper triangles correspond to the 1/1 mixture with the latex blend. The analyzer (in front of the camera) was in s-position, that is, the electric field vector was perpendicular to the plane of incidence. Polarizer angles of 0 and 180 degree denote an E-vector, which is perpendicular to the plane of incidence as defined by the position of the camera. The (dark) background clearly shows the effects of crossing polarizers. The brightness is reduced compared to parallel polarizers by about a factor of 2 – 3. This contrasts to the variation of brightness inside the areas coated with the ink. In these areas, the angle dependence is much reduced. Note that a weak dependence of the brightness on the angle of the polarizer can also be achieved with conventional white ink. However, white ink at the same time is much brighter than the background. One cannot achieve contrast inversion. The anisotropic ink by itself scatters light only weakly. Its effect is based on the scrambling of polarization. For that reason, areas coated with pure nanocellulose appear *darker* than the background when viewed with parallel polarizers. The ink redistributes the light between the two polarizations. Unfortunately, the effect is slightly weaker with the CNC/latex blend than with pure CNC. Pure CNC is not a

practical ink because it is not waterproof. There is no contrast inversion with the CNC/latex blend, but the ink's peculiar behavior still is easily recognized.

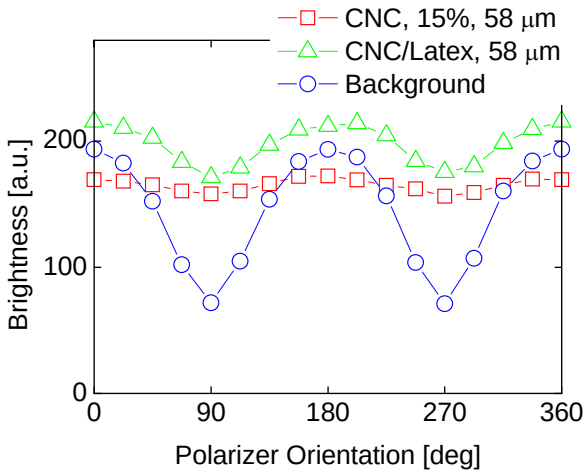

Figure 6.4 Average brightness versus angle of the polarizer (*P* in Fig. 6.3). The brightness of the background is significantly reduced under crossed polarizers, while the brightness of the ink stays about the same.

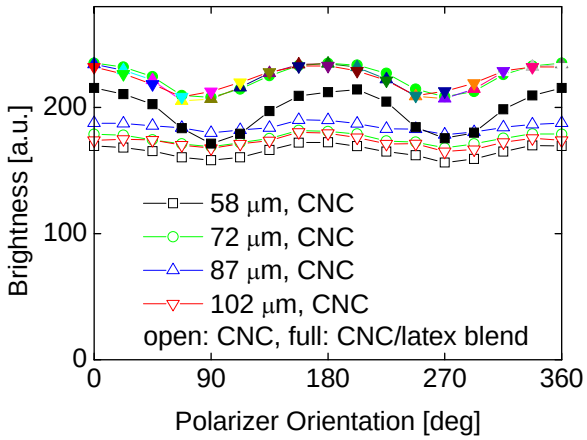

Figure 6.5 Same as Fig. 6.4, where the average thickness of printed layer was varied between 58 and 102 μm.

Fig. 6.5 addresses the thickness dependence. Clearly, thickness is of little influence in the thickness range from 60 µm to 100 µm. The overall brightness is somewhat larger when the average thickness is increased, but this effect has to be weighed against other properties like durability or cost.

6.4.2 In-plane orientation

So far, the discussion focused on the orientation of the polarizers. One might hope that the orientation of the sample (the angle φ in Fig. 6.3) might lead to equally impressive results. However this is not the case as demonstrated in Fig. 6.6. Optical observation does show a slight variability of the sample's appearance upon rotation in the plane of the substrate, but this variability does not translate to a significant variability after averaging over area. Clearly, the material is not well aligned.

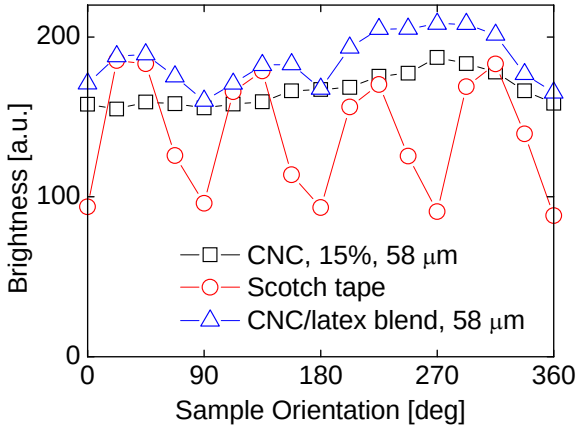

Figure 6.6 Average brightness versus orientation of the sample (φ in Fig. 6.3). The brightness of the areas covered with ink only weakly depends on the orientation of the sample. This contrasts to the areas covered with Scotch tape. These vary strongly in brightness because scotch tape is birefringent with a uniform orientation of the principal axes.

There are two sources of poor alignment. The first is the "coffee-stain" effect, which aligns the material *after* deposition, that is, while it dries.[23] Immediately after deposition, one does observe alignment along the direction of drawing. However this alignment is largely destroyed by the flow of water towards the edge of the drop. The matter has been extensively discussed in the context of latex films.[24] Importantly, a flow of liquid relative to a soft

network of CNC rods orients the rods. The images suggest that the rods are lined up parallel to the edge. This can be explained with the compression of a loose network of rods under a viscous stress as sketched in Fig. 6.7. A second source of misalignment can be a rough substrate (such as paper). Fig. 6.8 demonstrates the effect. The letters were written onto a slightly translucent paper (sandwich paper, purchased at a supermarket); the images were acquired in transmission with crossed polarizers. Panel A shows the sample immediately after application of the ink. There is some birefringence; the letters are clearly distinguished from the background. The birefringence is larger for a letter written with pure nanocellulose than for the letter written with the CNC/latex blend (to the right and to the left, respectively). However, the orientation is lost after drying (panel B). If paper is the substrate, it will always be difficult to maintain a well-defined orientation after drying.

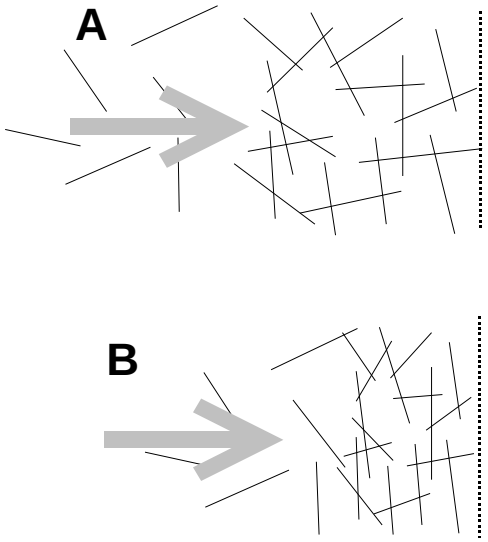

Figure 6.7 Sketch of how the coffee stain effect orients a loose network of rods at the edge of a drying droplet. The orientation is the consequence of a uniaxial compression. The dotted line is the edge of the sample. The grey arrows denotes a flow of liquid towards the edge, caused by the coffee-stain effect. The flow compresses the network of nanorods.

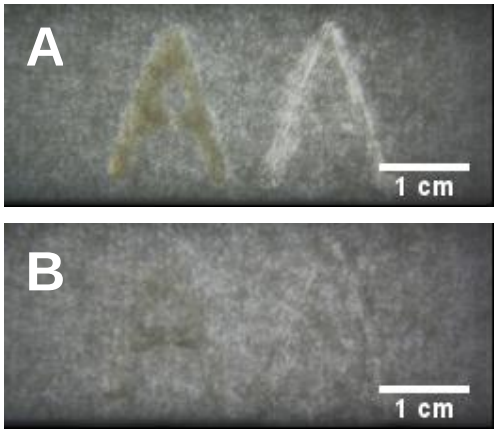

Figure 6.8 The letter "A" was written onto slightly translucent paper and imaged in transmission with crossed polarizers. Left: CNC/latex blend, Right: pure CNC. In the wet state (A) there is birefringence, which, however, is lost during drying (B). The ink applied to rough surface is not easily aligned on the macroscopic scale.

6.4.3 Microscopic texture

CNC ink displays a texture on the level of a few microns. The texture is characteristic, it can serve for authentication purposes. Of course a microscope (or at least a magnifying glass) is needed. The texture of the ink produced from pure nanocellulose (Fig. 6.9A) reflects the material's chiral-nematic behavior. An experienced observer easily recognizes the texture, although quantification and automated recognition is difficult.

The microscopic texture of the CNC/latex blend is different. It does show streaks along the preferred direction, but these are not caused by chirality. They are not related to a pitch of a twisted structure, but rather go back to demixing between polymer and cellulose on the microscale during drying. Demixing was proven with confocal microscopy. The ink was stained with a water soluble dye, namely sulforhodamine G. A variability in brightness reflects variability in concentration of the dye, rather than orientation. Since sulforhodamine G is hydrophilic, it is enriched in hydrophilic domains upon microphase-separation. The pattern seen in Fig. 6.9B presumable is caused by a micro-scale demixing between polymer an nanocellulose.

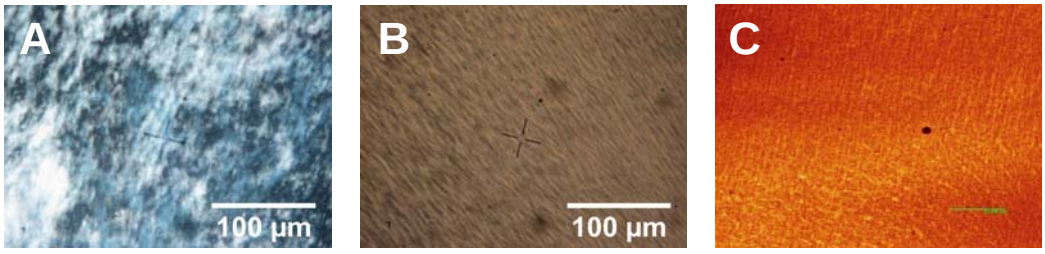

Figure 6.9 Micrographs taken of a layer of pure nanocellulose (A), a layer of a nanocellulose/latex blend (B). Panel C shows confocal microscope image of a nanocellulose/latex blend. For the image in C, the CNC had been stained with sulforhodamine G. The patterns correspond to concentration fluctuations of the dye. The dry material shows demixing between the polymer phase and the nanocellulose.

6.5 Conclusions

We propose the use of a CNC latex blend as an ink for security printing. The inks is recognized as being special in diffuse reflection, if polarizers are inserted between the light source and the paper and, also, between the paper and the observer. Such devices are easily realized; their application is trivial.

Ink made of CNC appears peculiar because it scrambles the polarization from the background without being a strong scatterer, itself. Application requires a dark background. Applied to black paper, the contrast strongly depends on whether the printed area is viewed with polarizers being parallel or with crossed polarizers.

6.6 Acknowledgements

We thank Arne Langhoff for technical help with the confocal laser scanning microscopy. Chakkresit Chindawong received a graduate fellowship from the Thai Ministry of Science and Technology.

6.7 References

1 http://prado.consilium.europa.eu/en/glossarypopup.html, downloaded on 21.12.2013

2 Barbera-Guillem, E., Fluorescent ink compositions comprising functionalized fluorescent nanocrystals. *US 8241765 B2* **2012**.

3 Lee, H. S.; Shim, T. S.; Hwang, H.; Yang, S. M.; Kim, S. H., Colloidal Photonic Crystals toward Structural Color Palettes for Security Materials. *Chemistry of Materials* **2013,** 25, (13), 2684-2690.

4 Berne, B. J.; Pecora, R., Dynamic Light Scattering: With Applications to Chemistry, Biology, and Physics. Dover Pubn Inc: 2003.

5 Ranby, B. G., Fibrous macromolecular systems. Cellulose and muscle. The colloidal properties of cellulose micelles. *Discussions of the Faraday Society* **1951,** 11, 158-164.

6 Samir, M.; Alloin, F.; Dufresne, A., Review of recent research into cellulosic whiskers, their properties and their application in nanocomposite field. *Biomacromolecules* **2005,** 6, (2), 612-626.

7 Dufresne, A., Nanocellulose: From Nature to High Performance Tailored Materials. De Gruyter: 2012.

8 Klemm, D.; Schumann, D.; Kramer, F.; Hessler, N.; Hornung, M.; Schmauder, H. P.; Marsch, S., Nanocelluloses as innovative polymers in research and application. In *Polysaccharides II*, 2006; Vol. 205, pp 49-96.

9 http://umaine.edu/pdc/cellulose-nano-crystals/, downloaded on 21.12.2013

10 Araki, J.; Wada, M.; Kuga, S.; Okano, T., Birefringent glassy phase of a cellulose microcrystal suspension. *Langmuir* **2000,** 16, (6), 2413-2415.

11 Edgar, C. D.; Gray, D. G., Smooth model cellulose I surfaces from nanocrystal suspensions. *Cellulose* **2003,** 10, (4), 299-306.

12 Roman, M.; Navarro, F., Deposition of Cellulose Nanocrystals by Inkjet Printing. In *ACS Symposium Series*, American Chemical Society: 2009; Vol. 1019.

13 Reising, A. B.; Moon, R. J.; Youngblood, J. P., Effect of Particle Alignment on Mechanical Properties of Neat Cellulose Nanocrystal Films. *J-for-Journal of Science & Technology for Forest Products and Processes* **2012,** 2, (6), 32-41.

14 Diaz, J. A.; Wu, X. W.; Martini, A.; Youngblood, J. P.; Moon, R. J., Thermal Expansion of Self-Organized and Shear-Oriented Cellulose Nanocrystal Films. *Biomacromolecules* **2013,** 14, (8), 2900-2908.

15 Picard, G.; Simon, D.; Kadiri, Y.; LeBreux, J. D.; Ghozayel, F., Cellulose Nanocrystal Iridescence: A New Model. *Langmuir* **2012,** 28, (41), 14799-14807.

16 Revol, J. F.; Godbout, J. D. L.; Gray, D. G., Solidified liquid crystals of cellulose with optically variable properties. *Patent* **1995,** WO9521901.

17 Zhang, Y. P., Anti-counterfeiting method using synthesized Nanocrystalline Cellulose Taggants. *Ph.D. Thesis, Department of Electrical and Computer Engineering, McGill University, Montreal* **2012**.

18 Beck, S.; Bouchard, J.; Berry, R., Controlling the Reflection Wavelength of Iridescent Solid Films of Nanocrystalline Cellulose. *Biomacromolecules* **2011,** 12, (1), 167-172.

19 Favier, V.; Canova, G. R.; Cavaille, J. Y.; Chanzy, H.; Dufresne, A.; Gauthier, C., Nanocomposite Materials from Latex and Cellulose Whiskers. *Polymers for Advanced Technologies* **1995,** 6, (5), 351-355.

20 Ben Mabrouk, A.; Vilar, M. R.; Magnin, A.; Belgacem, M. N.; Boufi, S., Synthesis and characterization of cellulose whiskers/polymer nanocomposite dispersion by mini-emulsion polymerization. *Journal of Colloid and Interface Science* **2011,** 363, (1), 129-136.

21 Hajji, P.; Cavaille, J. Y.; Favier, V.; Gauthier, C.; Vigier, G., Tensile behavior of nanocomposites from latex and cellulose whiskers. *Polymer Composites* **1996,** 17, (4), 612-619.

22 http://umaine.edu/pdc/nanofiber-r-d/, downloaded on 21.12.2013

23 Deegan, R. D.; Bakajin, O.; Dupont, T. F.; Huber, G.; Nagel, S. R.; Witten, T. A., Capillary flow as the cause of ring stains from dried liquid drops. *Nature* **1997,** 389, (6653), 827-829.

24 Routh, A. F., Drying of thin colloidal films. *Reports on Progress in Physics* **2013,** 76, (4), 046603.

Chapter 7

Conclusions

Conclusions

In light of the research results described in Chapter 3 through 6 and with respect to the objectives of this project given in Chapter 2, the following conclusions can be drawn.

The local heating of focus laser beam can used to guide the structure formation during drying of polymer films. We found the characteristic difference between polystyrene films drying from toluene solution and dextran films from aqueous solution. The height profile of polystyrene is well described by a Gaussian. Dextran films dried under similar condition develop a small cusp in the center. The cusp develops because of buckling.

We showed how the black ink can be used to pattern thin polymer films. This method is versatile since the black ink can be printed easily, and even possibly removed, thus allowing creation of the raised features are quite the same diameter. It constitutes a simple way to structure the surface of a film of micrometric thickness, to provide desired optical, electrical, or wetting properties. Adding of a dye into polymer solution did not have an effect on the aspect ratio and the amplitude of patterned surface. The pitch size and the wet film thickness strongly influence on the amplitude of the texture formation. The molecular weight of polymers did not effect on the amplitude of the texture formation.

We showed how to prepare a smooth, stable and thin films of pure CNC, CNC/latex blend and CNC with sol-gel prepared by spin-coating method. The films display birefringence as a result of the intrinsic shape and optical anisotropy of rod-like CNC which were oriented by the spin-coating process. Films prepared by spin-coating displayed radial orientation of the rod-shaped cellulose nanocrystals. The crystalline nanocelluloses with sol-gel dip-coating films were stable in water. The pencil hardness of all films prepared by dip-coating with sol-gel solution is 8B.

We showed how to use a CNC latex blend as an ink for security printing. The inks is recognized as being special in diffuse reflection, if polarizers are inserted between the light source and the paper and, also, between the paper and the observer. Such devices are easily realized; their application is trivial. Ink made of CNC appears peculiar

because it scrambles the polarization from the background without being a strong scatterer, itself. Application requires a dark background. Applied to black paper, the contrast strongly depends on whether the printed area is viewed with polarizers being parallel or with crossed polarizers.